

# Solid Oxide Fuel Cell Cathodes

Dynamics of Interfaces

**Nielsen, Jimmi**

*Publication date:*
2008

# *Solid-Oxide-Fuel-Cell cathodes*
## *Dynamics of interfaces*

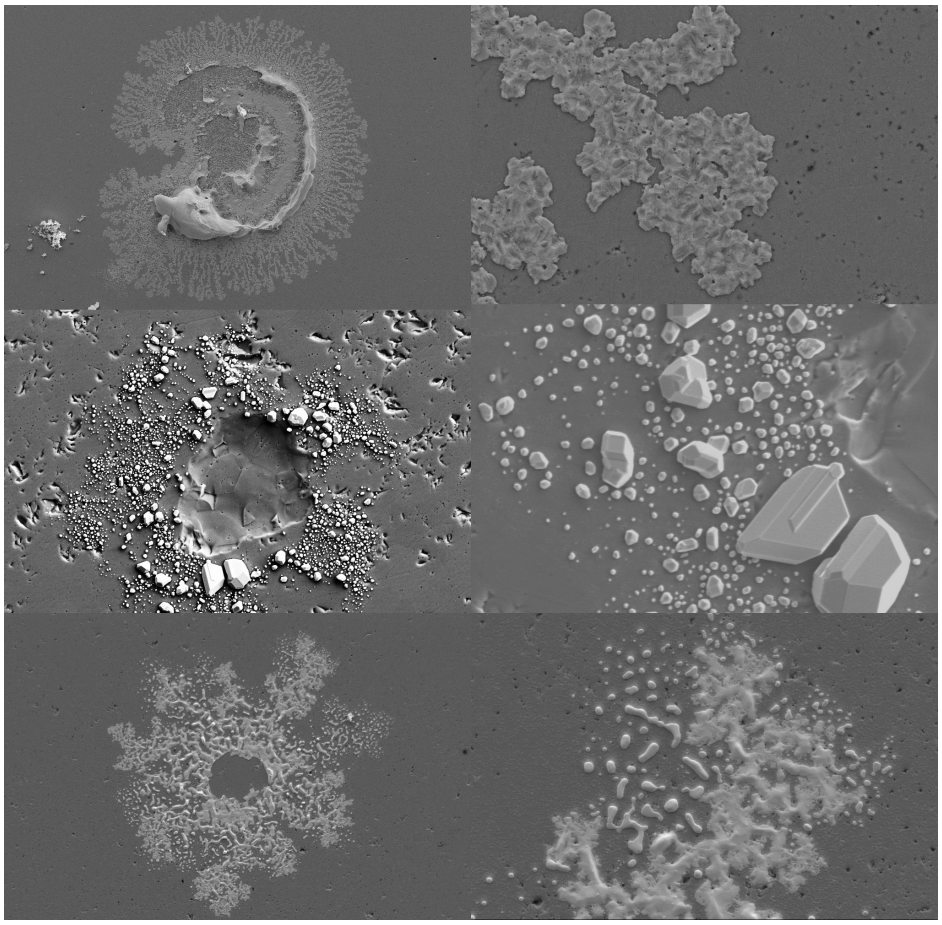

*Jimmi Nielsen*

*Ph.d. Thesis*

*Department of Chemistry*
*Technical University of Denmark*

*October 2007*

## List of Abbrevations

| | |
|---|---|
| SOFC | Solid Oxide Fuel Cell |
| OCV | Open Circuit Voltage |
| PEEM | Photo Emission Electron Microscopy |
| PLD | Pulsed Laser Deposition |
| SEM | Scanning Electron Microscopy |
| EDS | Energy Dispersive Spectroscopy |
| Pt | Platinum |
| Pd | Palladium |
| Au | Gold |
| Ag | Silver |
| Ir | Irridium |
| LSM | Strontium doped Lanthanum Manganite $(La_{0.85}Sr_{0.15})_{0.95}MnO_{3\pm\delta}$ |
| Freq. | Frequency |

# Solid-Oxide-Fuel-Cell cathodes
## Dynamics of interfaces


## Summary

It is well known in the literature that Platinum/yttria-stabilized-zirconia (Pt/YSZ) model electrodes for the cathode in Solid Oxide Fuel Cell (SOFC) show activation at moderate to high cathodic polarization. Further, it is well known that passage of current on a long timescale result in morphological changes at the interface between the Pt electrode and the YSZ electrolyte. It is also well known that similar, but less pronounced, activation take place for SOFC relevant LSM model electrodes and that one chamber SOFC with LSM as cathode show activation and deactivation as function of time during operation.

The purpose of the Ph.d. project is to contribute to the knowledge and to gain further understanding about the processes taking place at the cathode in solid oxide fuel cells. Particularly of interest, are the processes which are a consequence of the electrode reactions and are of great importance for the long term stability. In the studies, simple model systems has been used in the form of point-, mikro- and geometrically well defined pattern electrodes upon a polished YSZ electrolyte. The basis has been Pt electrodes, but other noble metals and SOFC relevant Lathanum-Strotium-Manganite (LSM) electrodes has also been studied. The used electrochemical techniques were chronoamperometry, linear voltammetry and impedance spectroscopy.

Introductory investigations were carried out regarding the influence of a frequency dependent potential distribution on the traditional determination of various impedance spectrum determined parameters, as well as the influence on the shape of an impedance spectrum. The studies show that the frequency dependent potential distribution can affect the shape of an impedance spectrum. Further, it is illustrated that the error, as a result of a frequency dependent potential distribution when determining the polarization resistance for normally applied point- and microelectrodes, in most cases is neglectable.

The performed electrochemical experiments with Pt microelectrodes and subsequently scanning electron microscopy (SEM) investigations show that the primary reason for Pt electrodes showing activating upon cathodic polarization is an increase of the electrode by migration of Pt electrode material. The studies also show that the phenomena is not unique for Pt, but also

take place for noble metal electrodes such as silver (Ag) and Palladium (Pd) electrodes. Gold (Au), on the contrary, shows no sign of electrode material migration. Different designed experiments suggest that formed $PtO_2(g)$ and AgO(g) is reduced at the cathodic polarized Three-Phase-Boundary (TPB). Pd electrode material migration happens considerably faster than in the case of Pt and Ag electrodes. Since the partial pressure of PdO(g) is so low that it does not result in any significant evaporation of Pd, gas phase transport can not explain the electrode material migration of Pd. An unknown surface transport mechanism seems to be present.

Systematic impedance spectroscopy studies of an array of Pt microelectrodes with varying size in a self build hotstage setup indicate that oxygen diffusion is possible through the bulk of Pt. In the literature this is assumed to be neglectable. The systematic impedance studies further show the presence of two processes with different characteristic time constants.

High cathodic polarization of Au point-electrodes show that activation of Au electrodes is also possible. Post mortem examination with SEM show that considerable morphological changes of the interface have taken place, particularly at TPB. These changes are causing the observed activation. The investigations suggest that the morphological changes are current induced or accelerated by current. Similar investigations of LSM point-electrodes and LSM films as electrodes reveal that the observed morphological changes for Au electrodes also take place for LSM electrodes. Further, the LSM investigations show extensive formation of the poor electronic conducting and catalytic $La_2Zr_2O_7$ phase. This is unexpected since LSM with 5 percent excess manganese has been used, which is reported to considerably reduce the formation of $La_2Zr_2O_7$.

# Faststof-Oxid-Brændselscelle katoder
## Dynamik af grænseflader


*Resumé*

Det er velkendt i litteraturen, at platin/yttria-stabiliseret-zirkonia modelelektroder (Pt/YSZ), for katoden i faststof-oxid-brændselsceller (SOFC), udviser aktivering ved moderat til kraftig katodisk polarisation, samt at længere tids strømpassage skaber ændringer af morfologien af grænsefladen mellem Pt elektrode og YSZ elektrolyt. Det er også kendt, at tilsvarende, men knap så udpræget, aktivering af SOFC relevante LSM modelelektroder finder sted og, at et kammer brændselsceller med LSM som katode udviser både aktivering og passivering som funktion af tiden under drift.

Formålet med Ph.d. projektet er at bidrage til kendskabet og øge forståelsen af de processer, der finder sted ved katoden i faststof-oxide-brændselsceller. Det er især processerne, som er en konsekvens af elektrodereaktionerne, og som har stor betydning for den langsigtede stabilitet, der er af interesse. I studierne er der anvendt simple modelsystemer i form af punkt-, mikro-, og geometrisk veldefinerede mønster elektroder oven på en polykrystallinsk poleret YSZ elektrolyt. Udgangspunktet har været platin elektroder, men også andre ædelmetal og SOFC relevante Lathan-Strontium-Manganit (LSM) elektroder har været studeret. De anvendte elektrokemiske teknikker har i undersøgelserne været chronoamperometri, lineær voltammetri og impedans spektroskopi.

Indledningsvis er det blevet undersøgt, hvor stor betydning en frekvens afhængig potentialfordeling har for traditionel bestemmelse af diverse parametre fra et impedans spektrum, og hvilken indflydelse det har på udseendet af et impedans spektrum. Det er vist, at en frekvensafhængig potentialfordeling i princippet kan påvirke udseendet af et impedansspektrum. Desuden er det vist, at fejlen som resultat af en frekvensafhængig potentialfordeling ved bestemmelse af polarisationmodstanden er, i langt de fleste tilfælde for normal anvendte punkt- og mikroelektroder, negligerbar.

De udførte elektrokemiske forsøg med Pt mikroelektroder med efterfølgende Skanning Elektron mikroskopi (SEM) undersøgelser, viser, at den primære grund til Pt elektroders aktivering ved katodisk polarisation skyldes en forøgelse af selve elektroden ved migration af Pt elektrodemateriale. Forsøgene viser også, at det ikke er et unikt fænomen for Pt men, at det også finder sted for

andre ædelmetalelektroder, såsom sølv (Ag) og palladium (Pd) elektroder. Guld (Au) viser derimod ingen tegn på elektrodematerialemigration. Forskellige designede eksperimeter antyder, at elektrodematerialemigrationen for Pt og Ag hovedsagelig skyldes, at dannet $PtO_2(g)$ og AgO(g) reduceres ved den katodisk polariserede tre-fase-grænse (TPB). Pd elektrodematerialemigration foregår betydeligt hurtigere end for Pt og Ag. Da partialtrykket af PdO(g) er så lille, at det ikke forårsager nogen signifikant fordampning af Pd, kan gasfasetransport af Pd ikke forklare migrationen af Pd. Dette tyder på, at en ukendt overflademigrationsmekanisme er til stede.

Systematiske impedansspektroskopistudier af et array af Pt mikroelektroder i en selvbygget hotstageopstilling antyder, at oxygen kan diffundere gennem Pt, hvilket i litteraturen er antaget til ikke at finde sted. De systematiske impedansstudier viser yderligere en tydelig tilstedeværelse af to processer med forskellige karakteristiske tidskonstanter.

Kraftig katodisk polarisation af Au punktelektroder viser, at der også kan ske en aktivering af Au elektroder. Efterfølgende undersøgelser af kontaktområdet med SEM viser, at betydelige morfologiske ændringer af kontaktområdet har fundet sted, især ved TPB. Disse ændringer er årsagen til den observerede aktivering. Undersøgelserne tyder på, at de morfologiske ændringer er strømforårsaget eller fremskyndet ved strømpassage. Tilsvarende undersøgelser af LSM punktelektroder og LSM film som elektroder afslører, at de morfologiske ændringer for Au elektroder også finder sted for LSM elektroder. Desuden viser LSM undersøgelserne dannelsen af den dårlige elektrisk ledende og katalytiske $La_2Zr_2O_7$ fase. Dette er uventet, da der er anvendt LSM med 5 procent overskud af mangan, som er rapporteret kraftigt reducerende for dannelsen af $La_2Zr_2O_7$.

## Preface

The present thesis has been submitted to the Technical University of Denmark (DTU) as a partial fulfilment of the requirement for obtaining the Ph.d. degree at DTU. The Ph.d. scholarship is part of the project "Efficient conversion of renewable energy by solid oxide fuel cells" financed by The Danish Ministry of Science Technology and Innovation. The experimental work has been carried out at:

- Department of Chemistry - DTU.
- Materials Research Department - Risø National Laboratory - DTU.

I thank my supervisors, associate professor Torben Jacobsen (DTU) and research professor Mogens Mogensen (Risø), for guidance during the project. A special thanks to Torben Jacobsen for a relaxed, open door policy in everyday guidance and the many inspiring and fruitful discussions. Also a special thanks to Mogens Mogensen and Karin Vels Hansen for providing access and introduction to the many experimental facilities at Risø. A number of people have been very helpful during the experimental work at Risø and deserve an explicit thanks:

- Senior scientist Jørgen Bilde-Sørensen for explanation and assistance with scanning electron microscopy.
- Senior scientist Nini Pryds and research assistant Katarzyna Rodrigo for the PLD deposition.
- Post. Doc. Ming Chen for help regarding Factsage and Thermo-Calc.
- Head of programme Rafael Taboryski and technician Ina Blom at the polymer department at Risø for help with lithography.
- Ph.d. student Michael Steenbæk for always being willing to help.

Besides this, I would like to acknowledge www.Hattrick.org for making everyday life more exciting the past 3 years.

30. October 2007

Jimmi Nielsen
Department of chemistry
Technical University of Denmark

# Contents

# Chapter 1

# Introduction

Even though fuel cells were discovered in 1839 by Sir William Grove it was not until the apollo space missions (1961-1972) that the development and application of fuel cells occurred. The large interest in fuel cells evolved during the nineteen seventies oil crises which initiated large research and development efforts. The increasing environmental awareness during the last 30-40 years has further contributed of making fuel cells an attractive technology. The main advantage of fuel cells as compared to conventional fossil fuel power generation is that the achievable efficiency is not subjected to any thermodynamic limit (Carnot cycle). The thermodynamic limitation of conventional power generation is a result of generating electrical energy from heat. In fuel cells the stored chemical energy is directly converted into electrical energy. In practice however, chemical reactions and mass transport energy and steric barriers, and hence energy losses, will always be present. The challenge from an engineering point of view is to understand and reduce these energy losses as much as possible.
Fuel cells are traditionally classified according to the electrolyte. This thesis deals with fuel cells based on a pure oxygen ion conducting solid oxide electrolyte, hence Solid Oxide Fuels Cells (SOFC's), with a operating temperature range from $600^0C$ to $1000^0C$. The benefits of SOFC as compared to other types of fuel cell are a generally higher efficiency and a larger tolerance towards different fuels, but with the disadvantage of a high operating temperature.

## 1.1 SOFC principle and characteristics

The operation principle of a SOFC can be seen in figure 1.1 page 11. The cell consists of two electrodes cathode and anode with a solid electrolyte in

between. At the cathode oxygen is reduced according to the reaction scheme:

$$\frac{1}{2}O_2 + 2e^- \rightarrow O^{2-} \tag{1.1}$$

The pure oxygen ion conducting electrolyte enables transport of oxygen ions to the anode, where they react and participate in a oxidation of the fuel, in this case hydrogen, resulting in the generation of water $H_2O$ and two electrons:

$$O^{2-} + H_2 \rightarrow \frac{1}{2}H_2O + 2e^- \tag{1.2}$$

A typical single cell has, depending on operation conditions, an open circuit

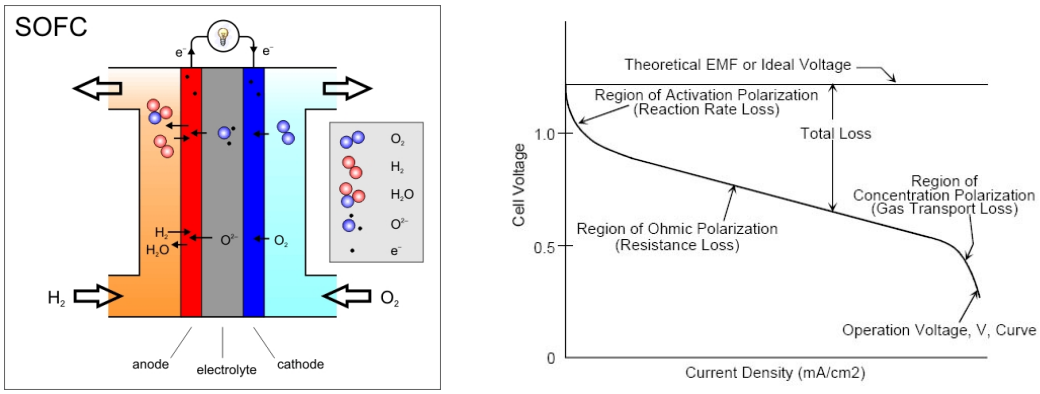


Figure 1.1: **Left:** Principle of a SOFC. **Right:** Characteristics of a typical fuel cell.

voltage of approximately 1V. To achieve the desired voltage cells are, with a interconnect material, serial connected into a stack.
A typical voltage-current fuel cell characteristic is shown to the right in figure 1.1 page 11. The operating cell voltage E can be expressed as:

$$E = E_{OCV} - IR_r - \eta_c - \eta_a \tag{1.3}$$

$E_{OCV}$ is the open circuit voltage and is dependent on operation conditions such as gas composition, temperature and electrolyte pinholes. $IR_r$ is ohmic loss, $\eta_c$ and $\eta_a$ are cathode and anode polarization losses. The right side of figure 1.1 page 11 shows three characteristic regimes:

- At low current densities the main energy loss is due to reaction kinetics of the electrodes. Improving the catalytic activity of the electrodes,

hence lowering of the energy barrier or barriers to overcome, will reduce electrode polarization losses. Of the two electrodes, the cathode contributes with the largest electrode overvoltage in modern SOFC´s.

- The ohmic resistance $R_r$ of the cell is the sum of contact resistance between the various cell components and the ionic/electronic conduction resistance from electrolyte and interconnect. The ohmic loss is dominating at moderate current densities (the linear regime).

- When the current density is high the kinetics can become mass transport controlled. The kinetics can either be limited by diffusion of reactants to the electrode or by the removal of reaction products from the electrode.

# Chapter 2

# Literature findings

## 2.1 Introduction

In spite of the last 20-30 years of extensive research effort to elucidate the cathode reaction kinetics, the details of the reaction 1.1 page 11 remains to a large extent a mystery. A recent review by Stuart B. Adler with 369 references summarizes the advances made in understanding the oxygen reduction and the factors governing SOFC cathode performance for electronic and mixed conduction cathode materials [1]. The studied cathode systems can generally be divided into the following three categories: model cathodes (noble metals), pure electronic ceramic cathodes of the type $La_xSr_{1-x}MnO_{3+\delta}$(LSM) and mixed electronic and oxygen ion conducting cathodes such as pioneering materials $La_xSr_{1-x}CoO_{3+\delta}$(LSC). The focus of this thesis are issues concerning pure electronic conducting cathodes or more specific noble metals and LSM.

### 2.1.1 Capacitance of SOFC cathodes

Common for cathodes on pure oxygen ion conducting electrolytes are an unusual high spread and value of the impedance estimated apparent double layer capacitance $C_{dl}$. For Pt this is typically greater than $10^{-4}F/cm^2$ [2, 3]. Attempts to measure the true $C_{dl}$ using chronoamperometry have yielded values of $10^{-6}$- and $10^{-5}F/cm^2$ respectively [2, 4], which is argued to be in reasonable accordance with the charge separation at the Pt/YSZ interface [2], hence the expectable $C_{dl}$ value. The origin of the high value of impedance determined apparent $C_{dl}$ remains so far unsolved, but M. Kleitz, who was one of the first to notice and point out the abnormal impedance $C_{dl}$ value, has argued and proposed that a reservoir of electroactive neutral

oxygen at cathode reactions is the cause [5]. The basis for this postulation is mainly measurements on Ag electrodes where oxygen dissolves into the Ag bulk. In this respect, it is worth mentioning that Metcalfe has argued that the NEMCA effect, with spill over of ionic oxygen from the YSZ to the electrode, can change the catalyst surface properties even at OCV [7]. This alternation of the catalyst surface properties might be M. Kleitzs postulated oxygen electrode reservoir of electroactive neutral oxygen.
For metal oxide ceramic cathode materials, an additional contribution to the apparent $C_{dl}$ exists in form of a chemical capacitance (oxidation/reduction of the bulk). It is a result of the ability of oxide ceramic materials to change oxygen stoichiometry at the electrode electrolyte interface upon polarization. The magnitude of the chemical capacitance depends on the bulk oxygen diffusivity and surface oxygen exchange coefficient for the given material. Capacitance values as high as 0.1-1 $F/cm^2$ have been reported [6]. The capacitance can therefore be used as a course measure for the involvement of the cathode bulk in the overall electrode reaction.
In contrast of $C_{dl}$ being a useful tool its existence also gives rise to problems. The problems are mainly associated with impedance kinetic studies on pure electronic cathode materials. The electrode reaction of these materials is restricted to the Three-Phase-Boundary (TPB), that is the line where electrode, electrolyte and air is in contact with each other, hence only a minor part of the electrode is active. The large inactive area has a relatively large capacitance that shunts the electrode reaction. The interference of capacitive current at high frequency in impedance spectroscopy has proven to be rather severe and in most cases the faradaic impedance information is overshadowed and buried in the capacitive response [23, 26]. Acquiring information about the electrode reaction is therefore non-trivial and will be discussed in more detail in section 5.1 page 31.
Another characteristic common feature for different cathode materials is non-stationary behaviour. The cathodes show activation, non-linearity and hysteresis phenomena at moderate to high polarization [8, 9, 10, 11, 12]. All though these are well known phenomena, very little is known about the cause.

## 2.2 Noble metals as model cathodes

### 2.2.1 Kinetics of Pt

Noble metals are generally believed to be a good foundation for acquiring knowledge about the fundamental mechanisms associated with reduction

and incorporation of oxygen into the doped $ZrO_2$ electrolyte. The chemical inertness and highly confinement of the electrode reaction to the TPB is believed to provide a simple and well defined system for studying the processes/reactions that take place near and at the TPB. The main focus of the thesis will be on Pt since it is by far the most studied noble metal in kinetic studies. The main necessary steps in the cathode reaction are transport of oxygen to the TPB reaction zone, charge transfer and incorporation of oxygen ions into the electrolyte. There is generally two pathways for transporting oxygen to the TPB zone. Oxygen can either adsorb directly at the TPB or/and adsorb some distance away and be transported to the TPB by surface diffusion. Examples can be found in the literature of each of the above mentioned steps, as being argued rate limiting for the overall reaction. One reason for the apparent contradictory conclusions in the literature could be and probably is a changing reaction mechanism as function of temperature, oxygen partial pressure, polarization, presence of impurities etc. However some reaction rate limiting factors are reported more frequently and better supported than others.

### 2.2.2 Adsorption

An essential step in the reduction of oxygen is adsorption onto the Pt surface. It has been well accepted for a long time that fast reversible dissociative adsorption on Pt takes place at elevated temperatures [13, 14]. Nonetheless low temperature studies on Pt(111) have shown that dissociative adsorption proceeds through sequential physi- and chemisorbed molecular precursor states [16, 17, 18]. The SOFC relevant strong chemisorbed desorption peak at approximately 720K in TPD measurements is reported to follow first order desorption kinetics. This also applies to polycrystalline Pt with oxygen supplied either by gas phase or electrochemically [15]. These results could indicate that desorption of atomic oxygen goes through the precursor states with desorption of molecular oxygen being rate determining. But it could also indicate associative desorption of atomic oxygen. The significance of precursor states and lateral interaction of adsorbed oxygen on adsorption kinetics has been studied in the modelling work of Mitterdorfer and Gauckler [25, 26, 27]. In this work kinetic parameter values and their dependency on temperature and oxygen partial pressure was estimated from impedance measurements. The conclusion was a significant dependency of the kinetic parameters on surface coverage and hence it were concluded that the ordinary Langmuir isotherm is not an accurate description at least not for the whole coverage range from 0 to 1.

### 2.2.3 Surface diffusion

Evidence for surface diffusion limitation has been observed many times. Several authors have performed conductivity measurements over a large oxygen partial pressure and temperature range showing that the conductivity as function of oxygen partial pressure goes through a maximum [19, 20, 21]. The slope of the regions before and after the conductivity maximum can be accounted for if diffusion controlled conditions is assumed. Another indication of diffusion limitations comes from the transient in chronoamperometry measurements [22]. After charging the double layer capacity the current decay from 150ms-1s could be modelled with a $t^{-1/2}$ (Cottrell) dependency at 873K, which is the classical sign of diffusion control. Impedance evidence of diffusion was first provided by Verkerk and Burggraaf [23]. They assumed that the electrode reaction impedance is in parallel with the double layer capacity (Randles circuit). This enabled them to subtract the double layer capacitance. The result was the characteristic impedance Warburg element with a finite diffusion layer for measurements at 983K. However, they did not account how they determined the double layer capacitance value or whether it was a pure capacitor or a constant phase element. It seems risky business to subtract something that you in principle do not know the nature and value of. More recently Mitterdorfer and Gauckler [25, 26, 27] used the method developed by Berthier et al. [24] for subtracting the effect of double layer capacitance. The result was a smooth and suppressed Warburg finite diffusion layer response at 975K. This was interpreted as and fitted with the gerisher impedance, which describes the situation of co-limited diffusion and reaction. In the case of platinum it corresponds to co-limitation of surface diffusion and adsorption. This is intuitively a more appealing description since adsorption, within the diffusion length, must take place. In order to evaluate whether surface diffusion is likely to be observed in electrochemical measurements it is essential to have knowledge about the surface diffusion constant for oxygen on platinum. Unfortunately data in this area is very sparse. In the references given above regarding diffusion, the measurements on Pt(111) field emitter tips conducted by Lewis and Gomer is typically mentioned [13]. Using this data the diffusion constant at 1000K can be estimated to $1*10^{-11}m^2/s$. However the more recent PEEM work on Pt(110) by Oertzen, Rotermund and Nettersheim has seldom been mentioned. They measured surface diffusion as function of coverage and identified to distinct regions with different diffusion coefficients separated with a relatively sharp change at coverage 0.2 monolayer. This change is in accordance with the impedance estimated diffusion

coefficient coverage dependency reported in the earlier mentioned modelling work by Mitterdorfer and Gauckler [25, 26, 27]. The PEEM results give the following diffusion coefficient values at 1000K $D_{\theta<0.2} = 5 * 10^{-8} m^2/s$ and $D_{0.2<\theta<0.7} = 3 * 10^{-8} m^2/s$. Due to the different crystallographic orientations direct comparison between the diffusion data is not possible, but it apparently shows that surface diffusion is highly dependent on the crystallographic orientation. It is difficult to make any predictions of which situation is predominant for polycrystalline Pt. The characteristic time $\tau$ for a pure diffusion process can be expressed as $\tau = \frac{\delta^2}{D}$, with $\delta$ being the diffusion layer thickness. $\tau$ can be extrapolated from the frequency in the impedance data, at which deviation from the characteristic warburg $\sim 45^o$ straight slope occurs. At short times the gerisher impedance resembles warburg behaviour meaning that it is possible to extract an order of magnitude $\tau$ value. Extracting $\tau$ from the above mentioned data of Robertson, Verkerk and Mitterdorfer and using the PEEM diffusion data gives diffusion lengths that vary from 10 to 10000$\mu$m, all of which are outside reason. Using the diffusion data of Lewis and Gomer gives diffusion lengths from a couple of hundred nm (data of mitterdorfer) to several $\mu$m. Although the data of Mitterdorfer and Gauckler is in the neighbourhood of what's reasonable the remaining data still provides diffusion lengths that are to large. Beside unrealistic diffusions lengths it also shows that the data are inconsistent.

### 2.2.4 Influence of impurities on kinetics

A speculative explanation for this lack of consistency and apparent unrealistic results, could be, that diffusion is not surface diffusion, but diffusion through an nm thick layer of impurities on the YSZ surface. The oxygen diffusion constant for the impurity film is expected to be significantly lower than the diffusion constant for surface diffusion on Pt. In this picture the cathode provides an electrode dependent concentration of atomic oxygen at the diffusion layer thickness and hence a performance variation for electrodes with different catalytic properties. The existence of a thin impurity film on the YSZ surface and impurity rim ridge at the TPB zone is well documented for the SOFC anode Ni electrode [54, 55, 56]. Different compositions and thickness of the impurity film might explain the inconsistent reported evidence for diffusion controlled kinetics.

## 2.3 LSM cathodes

### 2.3.1 Steady state measurements

The most detailed overview of the electrochemical properties of LSM is provided by steady-state d.c. characteristics and associated impedance of LSM measurements conducted by Siebert, Hammouche and Kleitz [28] at $960^oC$ in air. They made measurements on cone shaped dense sintered LSM electrodes on YSZ in order to minimize porosity effects. The result was an exponential increasing current in the anodic region with a single suppressed semicircle impedance response. In the cathodic regime the response from 0 to -150mV was an increasing current towards a limiting current and a single suppressed semicircle impedance response. From -150mV a sudden discontinous jump in current and difficulty in reaching a steady state was observed. The corresponding impedance showed beginning distinct features at high frequency and strong inductive effects at low frequency. From -200mV to -300mV the onset of an exponential like increase in current was observed and above this transition zone the impedance split up into a suppressed semicircle at high frequency and a suppressed Warburg finite diffusion response at low frequency. This was interpreted as the onset of ionic conductivity and is in agreement with the 30 percent strontium substituted Lanthanum Manganite electrode becoming substoichiometric with respect to oxygen around -300mV [29].

### 2.3.2 Surface versus bulk oxygen transport

As in the case of Pt, Mitterdorfer and Gauckler has shown that subtracting the electrolyte resistance and double layer capacitance from the suppressed single semicircle impedance response of porous LSM on YSZ at $850^oC$, using the method of Berthier et al [24], reveals a Gerisher like impedance response [30]. This result suggests that the cathode LSM kinetics is surface controlled as in the case of Pt. Numerous attempts has been made to provide clues about the influence of mixed conductivity, especially near the TPB, on the overall electrochemistry. It is well documented, that in the case of thin dense LSM films with a large area to TPB length ratio, the electrode resistance is controlled by electrode area and thickness, hence ionic conductivity [31, 32, 33, 34]. Further an increasing resistance with increasing oxygen partial pressure has been observed, indicating that the concentration of oxygen vacancies is of key importance [31]. LSM is at OCV in air oxygen superstoichiometric with cat ion vacancies and therefore ionic con-

ductivity is expected to be very poor [35, 29]. The polarisation at which LSM in air becomes oxygen substoichiometric depends on strontium doping and temperature and is located relatively far from the cathode polarization in SOFC´s. Brichzin et al. has recently made measurements on 100nm thick dense well defined circular electrodes with varying diameter (20-200$\mu$m) at $\sim 800^oC$ [36, 37]. These measurements showed a clear correlation between reaction resistance and electrode diameter at cathodic polarization, indicating that bulk ionic conductivity controls the overall reaction. Even though the thickness resembles the particle dimension of real porous LSM cathodes, the smallest electrode diameter 20$\mu$m certainly does not. In order to acquire knowledge about the transition from bulk to surface, controlled reaction kinetics measurements on smaller or thicker electrodes are needed. LSM pattern electrodes and isotope exchange experiments analyzed with SIMS has revealed information about oxygen incorporation [40, 41], but is unable to distinguish between surface and bulk kinetics [42].

### 2.3.3 Solid state chemical reactions

Another issue concerning cathodes are the chemical reactivity of the cathode with the YSZ electrolyte. It is well known that LSM reacts with YSZ and forms insulating secondary phases that inhibit the electrode/electrolyte interfacial processes. Typical secondary phases are $La_2Zr_2O_7$ (LZ) and $Sr_2ZrO_4$ (SZ) [30]. The formation of these secondary phases is greatly accelerated when LSM becomes manganese deficient. The solubility of manganese in YSZ is rather high [38, 39], so in order to avoid or slow down formation of secondary phases excess manganese is put into the LSM structure.

# Chapter 3

# The thesis

## 3.1 Objective of thesis

It is well established that activation, non-linearity and hysteresis phenomena take place for model electrode systems Pt-YSZ as well as electrode systems of SOFC cathode and anode materials LSM-YSZ and nickel-YSZ. The cause of the unexpected phenomena are unknown, but it is known that changes of the morphology and chemical composition take place near and at the interface between electrode and electrolyte. The objective of this thesis is to study the above mentioned changes and in this matter the role of current and thereby gain further insight to SOFC long term stability. Attempts will be made to correlate the changes with electrochemical measurements. The experimental approach is the use of different noble metals with different catalytic and physical properties. This simplifies the system by excluding the possibility of solid state chemical reactions, mixed conduction near the electrode perimeter, and it reduces the effect of ill defined and bad contact between electrode and electrolyte. The electrochemistry and characterized changes near and at the interface between electrode and electrolyte of noble metals will be compared with similar LSM experiments. The main characterization tool is SEM.

## 3.2 Thesis layout

Chapter 1 consist of introduction and the basic principle of SOFC together with the I-V characteristic of SOFC's. Chapter 2 is an overview of reported results in the literature regarding SOFC cathode kinetics and issues important for the performance of the cathode. The chapter is followed by the present chapter 3. Chapter 4 describes the experimental. Chapter 5 deals with some preliminary theoretical considerations with respect of using

impedance spectroscopy in studies on SOFC model point electrodes, micro-electrodes and thin films. Chapter 6-8 describe the obtained experimental results on various electrodes. Chapter 6 are results on Pt electrodes, chapter 7 are results on other noble metal electrodes (Pd, Ag and Au) and chapter 8 are results on and comparison of LSM and Au electrodes. Each of the last mentioned chapters starts either with a published, accepted or submitted article that is followed by additional results obtained on the subject of the chapter. This means that these chapters contain repetition of some of the experimental description and results. References within in articles are giving at the end of the articles, while references in additional result sections are together with references in the remaining part of the thesis given at the end. It is necessary to read the articles before reading the additional results sections of chapter 6-8. Chapter 9 summarizes and discusses the obtained results and state conclusions.

# Chapter 4

# Experimental

## 4.1 Materials used in experiments

Tabel 4.1 page 23 provides an overview of the materials used in the experimental work of the thesis.

### 4.1.1 Preparation of 8% YSZ electrolytes

Polycrystalline 8% YSZ electrolyte pellets were prepared by isostatically pressing at $4Kbar$ followed by sintering for 2 hours at temperatures ranging from $1300 - 1700^0C$. Suitable pieces were cut with a diamond saw. 8% YSZ powder supplied by Viking chemicals was sintered at $1300^0C$ and yielded crystallites of $\sim 200nm$ in diameter and the resulting pellets were polished in several steps ending with $3\mu m$ diamond paste. The Viking 8% YSZ was only used in Pt microelectrode measurements. 8% YSZ from Tosoh Corporation was sintered at temperatures from $1500 - 1700^0C$ resulting in crystallites ranging from several $\mu m$ to $\sim 10\mu m$. The resulting pellets were also polished in several steps ending with $1\mu m$ and in some cases $1/4\mu m$. The Tosoh 8% YSZ was used in Pt, Pd, Ag, Au and LSM electrode measurements. All 8% YSZ electrolyte pellets were cleaned in an ultrasonic bath of water and ethanol before experiments.

### 4.1.2 Preparation of electrodes

An overview of the electrodes can be seen in figure 4.1 page 24.

| **Electrolyte materials** | **Source of acquirement** | **Degree of purity** |
|---|---|---|
| Polycrystalline 8% YSZ | Viking chemicals | Al, Si and Fe < 10ppm<br>Na and Ca < 20ppm<br>Hf natural abundance 2mol% |
| Polycrystalline 8% YSZ | Tosoh Corporation | $Al_2O_3 < 0.005Wt\%$<br>$SiO_2 < 0.003Wt\%$, $SiO_2 < 0.060Wt\%$<br>$Fe_2O_3 < 0.002Wt\%$ |
| **Electrode materials** (Diameter) | | |
| Platinum wire (Pt) (0.3mm) | Johnson Matthey | Thermocouple quality |
| Palladium wire (Pd) (0.5mm) | Johnson Matthey | 99,9% |
| Silver wire (Ag) (0.4mm) | Johnson Matthey | Unknown |
| Gold wire (Au) (0.5mm) | Johnson Matthey | 99,9% |
| Pt80%/Ir20% wire (0.1mm) | Johnson Matthey | Unknown |
| $(La_{0.85}Sr_{0.15})_{0.95}MnO_{3\pm\delta}$ (LSM) | Topsoe Fuel cells | Unknown |

Table 4.1: Materials used in experimental work of the present thesis, source of acquirement and degree of purity.

### Microelectrodes

Pt, Pd and Ag microelectrodes were prepared by electrochemical etching of wires. The tips of the wires were placed in an gently stirred aqueous solution containing 40 volume percent of a saturated calcium chloride solution at room temperature [46]. With a graphite rod as counter electrode, a 50Hz AC voltage with a amplitude of $\sim 35V$ was applied. By small adjustments of the amplitude ($\pm 5V$) for the different metal wires, the desired cone shaped tip was achieved. The microelectrodes were prepared when there no longer was electronic contact between wire and solution.

The microelectrode wires were kept in place by putting the wire through a 6 bores alumina tube and locked by bending the wire out through the hole in the side of the alumina tube as shown on the image to the right of

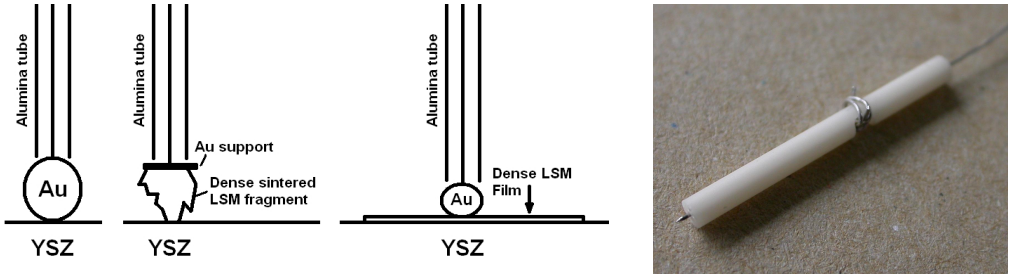


Figure 4.1: An overview of the electrodes used in experiments. The image to the right is a Pt microelectrode in a 6 bore alumina tube holder.

figure 4.1 page 24.

### Ball shaped noble metal point electrodes

Ball shaped point electrodes were prepared by melting a drop at the end of a wire in a gas flame.

### LSM point electrodes

The fragment of a dense sintered LSM tablet was pressed down onto a polished 8% YSZ tablet. Under assembly the LSM fragment was clued onto a gold support with ordinary household glue and pressed down on the 8% YSZ tablet before the whole assembly was heated.

### Pt and LSM Films as dense geometrically well defined electrodes

The films were deposited on 8% YSZ substrates by pulsed laser deposition (PLD) using a 1mm thick cobber mask with holes of 2mm in diameter. Depositions were done by Katarzyna Rodrigo at Risø National Laboratory Denmark.

### Array of Pt microelectrodes

A pattern for Pt microelectrodes were designed by the author of the present thesis. Standard clean room lithography was performed by Ina Blom and subsequent PLD Pt deposition was performed by Katarzyna Rodrigo. Both are employees at Risø National Laboratory - Technical University of Denmark.

## 4.2 Experimental setup

A sketch and an image of the 3 electrode experimental setup are presented in figure 4.2 page 26. The reference electrode consist of a wire around the YSZ tablet with painted Pt paste along the wire. The counter electrode was painted Pt paste on the opposite side of the working electrode. In most cases a two electrode setup was used with the reference electrode functioning both as reference and counter electrode.

The furnace was a tubular furnace with a length of 600mm and an inner diameter of 56mm. The experimental setup was mounted onto the furnace cap, as shown in the right image of figure 4.2 page 26, which was lowered down into the furnace. The shown horizontal alumina discs serves as radiation shields. In order to measure the temperature of the working electrode, a closed alumina tube with a thermocouple (Pt-10%Rh/Pt) inside, was lowered through a hole in the furnace cap down to the same level as the working electrode. The temperature and the heating rate of the furnace was controlled by an Eurotherm 902P temperature controller. The heating rate was if nothing else stated $100^0C/hour$ and cooling was done by switching off the furnace. During experiments, air saturated with water at room temperature was passed into the furnace by an inlet at the bottom of the furnace at a typical rate of 2.5l/h. This was done to keep the humidity and oxygen partial pressure fixed in the experiments making comparisons more reliable. Further indications has been presented that the atmospheric water content has influence on the electrochemistry of the SOFC Ni/YSZ anode [47].

All the wires in the setup are Pt except the different electrodes. Beside the YSZ electrolyte, all the internal parts of the furnace are solely made of alumina.

## 4.3 Hotstage

The construction of the hotstage and the hotstage setup are shown in figure 4.3 page 27. The supporting alumina rods (2) are grounded in order to reduce electrical noise from conducting ceramics at high operating temperatures $700 - 1000^0C$. Thin sheets of sapphire are chosen to separate the counter electrode from the ceramics of the hotstage for the following three reasons: A) Sapphire is an insulator. B) Sapphire has, for ceramics, good thermal conducting properties C) Sapphire is transparent. The transparency allows heat exchange by radiation and thereby minimizes temperature gra-

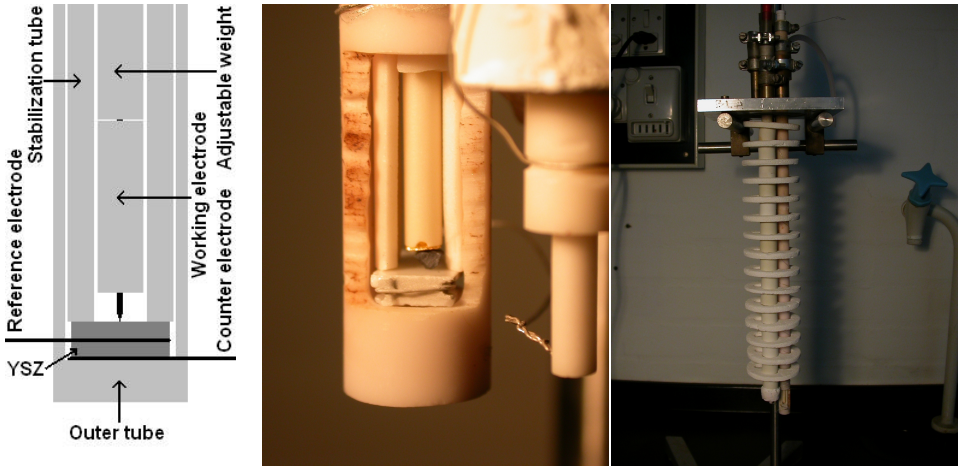


Figure 4.2: From the left a sketch of the 3 electrode setup. In the middle an image of the 3 electrode experimental setup. To the right an image of the furnace cap with the experimental setup which is lowered down into the tubular furnace.

dients within the hotstage. The Pt foil (4) electronically connects the Pt plate (5), which acts as a counter electrode. Since Pt is an excellent thermal conductor, even at $1000^0C$, it is assumed that no significant temperature gradients exist within the relatively thick 1mm Pt plate (5). By melting a thermocouple (6) onto the Pt plate it is possible to measure the temperature of the counter electrode. The 1mm thick YSZ slice (7) with microelectrodes is painted with Pt paste, on the opposite side of the electrodes, and placed on the Pt plate (5). The hole in the top of the hotstage, through which it is possible to electronically connect the microelectrodes, acts as a controlled leak of heat.
The contacting needle consisted of a 2mm in diameter Ag wire onto which a Pt80%/Ir20%, 0.1mm in diameter, wire was melted. The Pt80%/Ir20% wire was electrochemical etched as described in section 4.1.2 page 23. The length of the 20% Ir/Pt wire was 5-10mm.
When electronic contact to the microelectrodes was achieved the noise was reduced by simultaneously looking at an oscilloscope and moving the electrical ground along the heating coils, as described in section 4.4.3 page 29, until a minimum in observed noise was found.

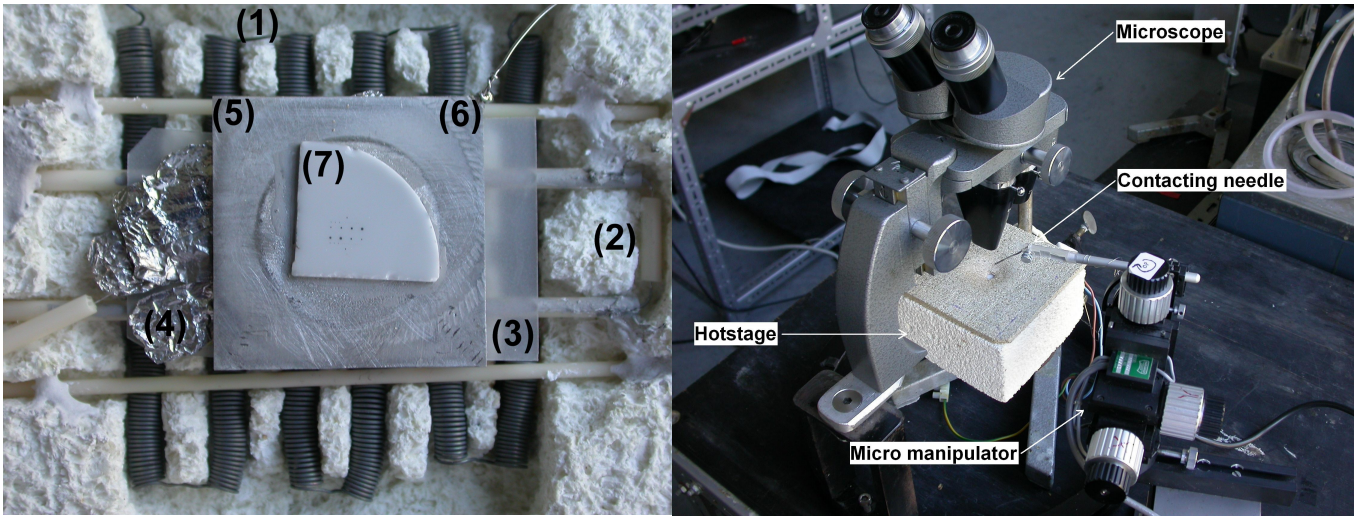


Figure 4.3: **Left:** Construction of the homebuild hotstage. **(1)** Kanthal heating coils. **(2)** 6 bore alumina support rods with a Pt wire through the rods and Pt paste on top. Pt wire and paste is electrically grounded. **(3)** 0.5 mm thick sapphire sheets. **(4)** Pt foil. **(5)** 26x26x1mm Pt plate. **(6)** 10% Rh/Pt thermocouple. **(7)** 1mm thick polycrystalline YSZ electrolyte with deposited Pt microelectrodes. **Right:** Overview of the setup with optical microscope, hotstage with the top and microminipulator.

## 4.4 Electrochemical measurements

The computer programs which are referred to in the following sections are unless otherwise stated written by T. Jacobsen, Department of chemistry, DTU. Polarization was kept on during cooling in all step polarization experiments.

### 4.4.1 Data acquisition

A setup consisting of a laboratory developed potentiostat was controlled by a Hewlett Packard HP 7500 series B controller. The HP applied signal was passed through a low pass filter before reaching the potentiostat. The controller transmitted data to and received instructions from a Pc with laboratory developed software. The setup was used to conduct ultra slow linear potential sweeps (1-100$\mu V/s$) and step polarization experiments.

A Gamry FAS 2 potentiostat was used to conduct impedance spectroscopy and medium to fast linear potential sweeps (100$\mu m/s$-1V/s) as well as step

polarization experiments with a high sampling rate (1 second) compared to the HP setup (360-1000s). Ultra slow sweeps, with periodic impedance spectrum recording, was made possible using a by the author modified gamry script. The script records with an adjustable time interval time, voltage, current, an impedance spectrum and finally writes the results in a file and repeats itself. The desired applied potential was provided to the control signal input channel of the gamry potentiostat by the above mentioned HP controller setup. The typical frequency range and amplitude in the recorded impedance spectra was respectively 100KHz-1Hz and 25 mV RMS. The number of data points per frequency decade ranged from 7 to 13. Systematic errors at high frequencies (above 1KHz), due to inductive behavior of cables etc., were mapped by impedance measurements on resistances with known values, that were close to the experimental values. The erroneous inductive phase shift, as function of resistance, was empirically described by polynomials. This was used in a small program to correct the high frequency part of the recorded impedance spectra. The program was also able automatically to correct systematic numbered impedance output files originating from periodic impedance monitoring during ultra slow linear potential sweeps and step polarization experiments. The corrected impedance spectra were fitted with a given equivalent circuit, using a laboratory developed fitting program, that is also able to automatically fit a series of systematic numbered impedance spectra files and put the resulting fitted parameters into one output file.

### 4.4.2 Estimation of electrolyte resistance from impedance spectra

Microelectrodes have small double layer capacitances, due to a limited reliable frequency window. This makes it difficult experimentally to make precise estimation of the electrolyte resistance, since considerable extrapolation is necessary. Impedance spectra of microelectrodes are discussed in detail in section 5.1 page 31.
The equivalent circuit $R_{electrolyte}(R_{polarization}Q)$ in Boukamp notation [51], is used for the estimation of the electrolyte resistance in periodic impedance monitored experiments. The recorded impedance spectra change shape during the experiments and the chosen frequency window used in fitting is selected in the following way: High frequencies are always included and the lower frequency limit is chosen on the following criterion, that the experimental data is well described by a suppressed semicircle in a nyquist plot. That is, the impedance spectrum in a series of spectra, that deviates mostly from a suppressed semicircle determines the lower frequency limit. To in-

sure reasonable agreement between fit and experimental data, the fits are inspected by eye after fitting. Examples of typical fitted impedance spectra can be seen in figure 4.4 page 29.

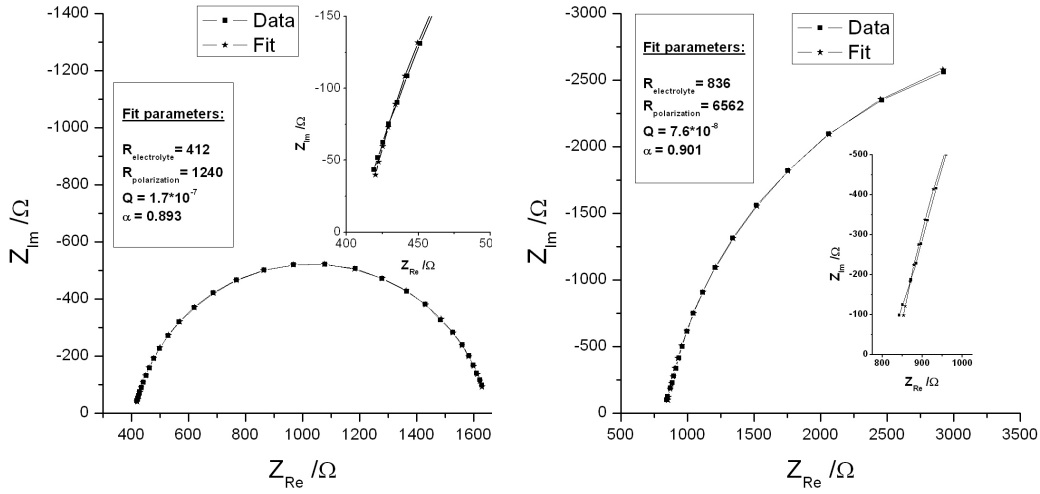


Figure 4.4: Typical fits with experimental impedance data.

### 4.4.3 Reduction of 50Hz noise

At high temperatures the alumina ceramics of the furnace has a small but finite electrical conductivity which introduces 50Hz noise from the heating coils of the furnace. It is quite severe at $1000^0C$ when measuring currents of around $1\mu A$ and lower. This is considerably reduced by moving the electrical ground along the heating coils to the level of the electrochemical cell inside the furnace using the method described in [48].

The Gamry FAS 2 potentiostat has some different build in filters that can be useful in eliminating 50Hz noise.

50Hz noise, in ultra slow linear potential sweeps and step polarization measurements with the HP controller setup, is eliminated by the computer program by creating data points from averaging of measurements during a period ranging from 360 to 1000s.

## 4.5 Characterization tools

### 4.5.1 SEM/EDS

After experiments and removal of electrodes the YSZ surfaces were examined for changes in morphology and chemical composition in a Scanning Electron Microscope (SEM) at Risø National Laboratory. The YSZ samples were coated with carbon in order to prevent charging. A JEOL JSM-840 microscope was accessible during the whole project period and a Field Emission Gun SEM (FEG-SEM) Zeiss SUPRA-65 was accessible during the last year of the project. The recorded images are secondary electron images.
Chemical compositions were analyzed by the microscopes Energy Dispersive X-ray Spectroscopy facility. The interaction volume of EDS is approximately $1\mu m^3$, which set the limit on how small features can be studied by the technique.

# Chapter 5

# Preliminary theoretical considerations

## 5.1 Considerations regarding choice of electrode type and size

Considerations regarding the advantage and disadvantage of different types of electrodes and electrode sizes are discussed in the following two sections for different techniques and purposes.

### 5.1.1 Kinetic studies with impedance spectroscopy

For pure electronically conducting electrodes, two sources of current are present in impedance recording.

- A current from the electrode reaction at the TPB
- A current from the double layer capacity

It is the current from the electrode reaction that is of interest. Interference from the capacitive current is therefore undesirable. Microelectrodes are useful in this respect because of a smaller interference from the capacitive current than in the case of normally applied larger point-electrodes. This is due to the fact that the current from the electrode reaction at the TPB depends on the electrode perimeter, while the capacitive current from the double layer capacity depends on the contact area between the electrode and the electrolyte. The different powers of the radius dependency of the two current sources means that the smaller the electrodes are the less is the relative interference from the capacitive current. There is however, a limit as to

how small the electrodes can be in practical measurements. Two situations are considered in the following:

**(I)** In the following, charge transfer is assumed to be rate limiting for the electrode reaction. It is appropriate to describe the situation with a Randles equivalent circuit. That is, an equivalent circuit consisting of an electrolyte resistance $R_{electrolyte}$ in series with a reaction resistance $R_{reaction}$ in parallel with a capacitor $C_{dl}$. $R_{reaction}$ is in impedance spectroscopy determined as $R_{reaction} = Z(freq. \rightarrow 0) - Z(freq. \rightarrow \infty)$. Thus, a good determination of $R_{reaction}$ requires that the impedance reaches the real axis in a Nyquist plot in the high and low frequency limit of the scanned frequency window. In practice, the frequency window at disposal is approximately 1MHz-1mHz. As the electrode size is decreased the capacitance is also decreased, and at some point it is no longer possible for the high frequency limit to reach the real axis in a Nyquist plot, and hence extrapolation is necessary. Continuing decreasing the electrode size will in the end result in a situation where it is no longer possible to determine the reaction resistance.

**(II)** In this scenario it is assumed that the electrode reaction is limited by mass transport. As a case model, the impedance response is described by a finite-length diffusion Warburg impedance response.

$$Z(j\omega) = \frac{dE}{dc} \cdot \frac{1}{zF} \cdot \frac{tanh(\delta\sqrt{\frac{j\omega}{D}})}{\sqrt{j\omega D}} \tag{5.1}$$

The overall situation can be described by an equivalent circuit consisting of an electrolyte resistance $R_{electrolyte}$ in series with a Warburg element W in parallel with a capacitor $C_{dl}$. The characteristic frequency $\nu_W$ for the Warburg element is approximately $\nu_W \simeq 0.4\frac{D}{\delta^2}$ [28], and hence independent of electrode size. D is the diffusion constant and $\delta$ is the diffusion length. $\nu_W$ is, for the discussed electrode reaction, assumed to be within the accessible frequency window. For large electrodes severe interference from capacitive current will be present and an impedance response very close to a semicircle, as in situation (I), will be observed. But since the characteristic frequency $\nu_W$ for the Warburg element is independent of the electrode size the Warburg response will be more and more clearly observed as the electrode size is decreased. A decrease of the electrode size should therefore in principle reveal an electrode reaction, which is diffusion controlled. This also applies to the situation with the double layer capacitance, shunting a gerisher impedance that is used for describing the situation where surface diffusion is co-limited with adsorption [1].

As mentioned in section 2.2.3 page 16, surface diffusion impedance responses have been reported in the literature. The diffusion responses were identified after using different procedures for subtracting the double layer capacitance from the impedance responses. In doing so, many assumptions were made, which are questionable. However, if the reported results and conclusions are correct it should be possible to verify them with the use of micro- or submicrometer electrodes.
In the above treated situations, the effect of current constriction has not been taken into account. This will be thoroughly dealt with in the sections to come. Nonetheless the smaller the electrodes, the smaller is the current constriction effect. This favors microelectrodes compared to the larger normally applied Point-electrodes.

### 5.1.2 Long term changes

In studies of the long term effects of polarization, it is desirable to have well defined contact areas in order to correlate the electrochemical responses with changes near and at the interface between the electrode and the electrolyte. High sensitivity towards discrete events at the reaction zone is desirable and is achieved with a small TPB length. This is due to the fact that the electrochemical response is a less averaged response, than in the case of a large TPB length. A relatively small TPB length can be obtained with the use of microelectrodes. The use of electrochemical etched noble metal wires as microelectrodes provides a fairly well defined system to study. The contact between the electrode and the electrolyte is good. A fairly well defined contact area for post mortem analysis is obtained along with a relatively good sensitivity towards discrete events at the TPB. Paste electrodes, on the other hand, have uncontrollable contact areas, which are unfit for post mortem analysis. Pattern electrodes are difficult and time consuming to make and they are difficult to contact. Besides this, they have a relatively short lifetime before they break up into islands.

## 5.2 Effects of potential distribution

### 5.2.1 Introduction

Impedance spectra of pure electronic conducting SOFC cathodes consist of two different current distributions with different electrolyte resistance values at the limiting situations of $freq. \rightarrow 0$ and $freq. \rightarrow \infty$. For disk electrodes at low frequency, the electrochemical reaction restricts the current to that of a ring electrode, and at high frequencies the whole disk electrode is active due to the double layer capacity. The change in electrolyte resistance during impedance recording introduces an error in the normal way of determining the polarization resistance as $R_{polarization} = Z(freq. \rightarrow 0) - Z(freq. \rightarrow \infty)$, with Z representing impedance. The questions addressed in the following are:

- How large is this error in determination of polarization resistance.
- How does the change in current distribution affect the shapes of impedance spectra.
- How does lateral resistance of films affect impedance spectra.

### 5.2.2 Theory

Electromagnetic behavior is described by a set of equations known as Maxwell's equations. Formulated as partial differential equations, Maxwell's equations take the form:

$$\nabla \times E + \frac{\partial B}{\partial t} = 0 \qquad (Faradays\ law) \tag{5.2}$$

$$\nabla \times H - \frac{\partial D}{\partial t} - J^c = 0 \qquad (Ampères\ law) \tag{5.3}$$

$$\nabla \cdot D = \rho \qquad (Gauss\ law\ of\ electricity) \tag{5.4}$$

$$\nabla \cdot B = 0 \qquad (Gauss\ law\ of\ magnetism) \tag{5.5}$$

E, B, H, D and $J^c$ are vector fields, while $\rho$ is a scalar. A description of the fields and the associated units can be seen in table 5.1 page 35. The

| **Quantity** | **Description** | **Unit** |
|---|---|---|
| | **Constitutive parameters** | |
| $\sigma$ | Specific conductivity | S/m |
| $\varepsilon$ | Electric flux density | $C/m^2$ |
| $\mu$ | Magnetic permeability | H/m |
| | **Fields** | |
| E | Electric field intensity | V/m |
| D | Electric flux density | $C/m^2$ |
| H | Magnetic field intensity | A/m |
| B | Magnetic flux density | $W/m^2$ |
| $\rho$ | Electric charge density | $C/m^3$ |
| $\varphi$ | Electric potential | V |
| J | Electric current density | $A/m^2$ |

Table 5.1: Constitutive parameters and field quantities

constitutive relations between the various fields are:

$$D = \varepsilon E \quad B = \mu H \quad J^c = \sigma E \tag{5.6}$$

where $\varepsilon$ is the electric permittivity, $\mu$ is the magnetic permeability and $\sigma$ is the specific conductivity. In the following, only isotropic homogeneous linear media are considered allowing free movement of the material properties $\varepsilon$, $\mu$ and $\sigma$ through the different operators of equation 5.2- 5.5. The time dependency normally complicate the solution considerably, but if it is known that a sinusoidal time dependency exists (like for example in impedance

spectroscopy) the so-called time harmonic model can be applied [49]. The model assumes that all scalar fields and components of the vector fields take the form $u(x,t) = Re(u(x,\omega)e^{-i\omega t})$, for some constant real valued $\omega$. The result is:

$$\nabla \times E - i\omega\mu H = 0 \quad (Faradays\ law) \tag{5.7}$$

$$\nabla \times H - \hat{\sigma}E = 0 \quad (Ampères\ law) \tag{5.8}$$

$$\nabla \cdot (\varepsilon E) = \rho \quad (Gauss\ law\ of\ electricity) \tag{5.9}$$

$$\nabla \cdot (\mu H) = 0 \quad (Gauss\ law\ of\ magnetism) \tag{5.10}$$

$\hat{\sigma} = \sigma - i\omega\varepsilon$ is the complex conductivity, and multiplied with E, it describes the total current J as the sum of the conduction current $J^c$ and the displacement current $J^d$. The equations 5.7- 5.10 above are Maxwell's equations in the frequency domain. The great advantage is that, for constant frequency, the equations are stationary and only dependent on the spatial coordinates. Making the reasonable assumption that induction of current from magnetic fields can be neglected, that is $\nabla \times E = 0$, which implies that the electric field can be written as $E = -\nabla\varphi$. Further taking the divergence of equation 5.8 (remember the identity $\nabla \cdot (\nabla \times F) = 0$), we arrive, at what is called the continuity equation expressing conservation of charge:

$$\nabla \cdot J = -\nabla \cdot ((\sigma + i\omega\varepsilon)\nabla\varphi) = 0 \tag{5.11}$$

This is the equation that is numerically solved for a given geometry, frequency, set of boundary conditions and material properties by the Comsol 3.3a program using the Finite Element Method (FEM). From the complex valued potential distribution the resulting complex valued current density can be calculated:

$$J = -\hat{\sigma}\nabla\varphi \tag{5.12}$$

The Comsol 3.3a program was used to do a boundary integration of the current through the ground area A (See figure 5.1 page 37). This makes it possible to calculate the impedance as:

$$Z = \frac{V_0}{\int_A -\hat{\sigma}\nabla\varphi \cdot dA} \tag{5.13}$$

By varying the frequency, doing the potential and current calculations enables a simulation of the entire impedance spectrum. In the case of electrostatics ($\omega$=0) equation 5.11 reduces to Laplace's equation:

$$\nabla^2\varphi = 0 \tag{5.14}$$

### 5.2.3 Geometry and parameters of the model

**DC**

The purpose of the calculations is to reflect situations in real measurements with point electrodes. This means that the potential drop in the electrolyte media should resemble that of an infinitely large electrolyte media. The question therefore is how large the radius and height of the chosen cylindrical electrolyte media should be, as compared to electrode radius, in order to fulfill this criterion. The relationship between electrolyte resistance R, electrolyte conductivity $\sigma$ and electrode radius r in 3D for an infinitely large electrolyte media is given by Newmans formula [50]:

$$R = \frac{1}{4\sigma r} \tag{5.15}$$

When $\sigma$ and r are chosen to be 1S/m and 0.1m it follows that the electrolyte media should have dimensions that result in a resistance of 2.5Ω. Calculations are done on a cylindrical electrolyte with a circular polarized area (1V) on top with radius 0.1m, and with the bottom of the cylindrical electrolyte as ground (0V). This is illustrated in the left figure of figure 5.1 page 37. All other exterior boundaries are set to behave as insulators. A calculation of the resistance is enabled by solving Laplace's equation 5.14 and calculating the total current as a current density boundary integration of the ground, using Comsol 3.3a. The right figure in figure 5.1 page 37 shows the electrolyte resistance as function of increasing cylindrical electrolyte radius and height (radius=height). It is illustrated that the resistance is larger than

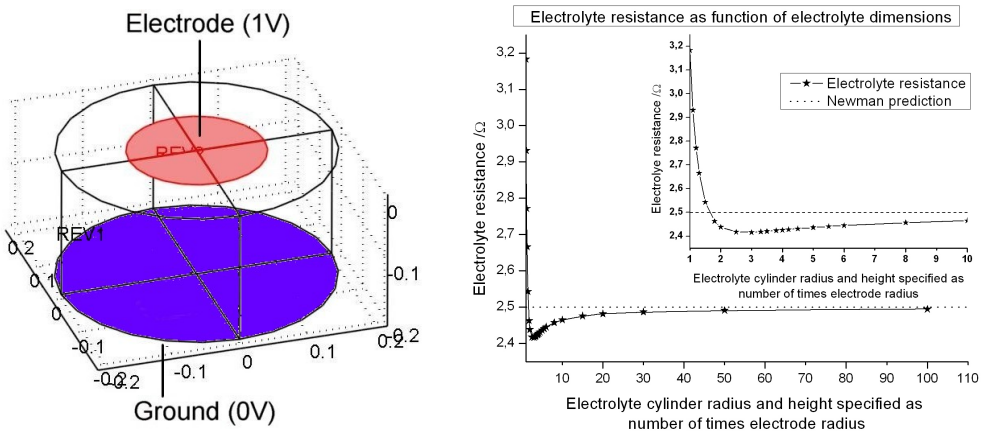


Figure 5.1: Left: Geometry of the model. Right: Electrolyte resistance as function of dimensions (radius=height).

the Newman value, when the electrolyte radius/height is close to that of the electrode radius. This is because the electrolyte dimension prevents the current from spreading out at the edge of the electrode, but as the electrolyte radius/height is increased the resistance drops rather quickly below the Newman value. On continuous increase of the radius/height asymptotic behavior towards the Newman value is observed. This is reassuring since it shows that the calculations, and hence meshing of the geometry, provides trustworthy results.

### AC

At a radius/height of 10 times the electrode radius the resistance is approximately 1-2 percent from Newman value which is accurate enough, and this is the scaling that is used in all the AC calculations. The electrode in the AC case is modelled by revolving the 2D situation with the stated physical parameters presented in figure 5.2 page 38. The outer DC active ring of the electrode (R3) is modelled as a very good conductor, compared to the electrolyte (R1), with a given permittivity $\varepsilon$, that has the same value as the permittivity of the non-conducting inner part of the electrode (R2). In order to make the calculations possible and less time consuming, calculations were done on a 6 percent cake slice of the described cylinder geometry. The final calculated complex valued current was scaled up to that of the whole cylinder geometry by multiplication of 60.

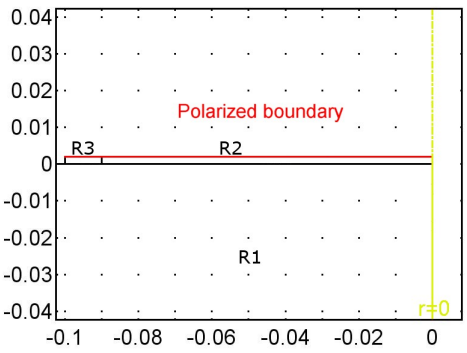


| Region | Physical properties |
|---|---|
| R1 | $\sigma$=1 S/m, $\varepsilon$=0 $C^2/Jm$ |
| R2 | $\sigma$=0 S/m, $\varepsilon$=0.01 $C^2/Jm$ |
| R3 | $\sigma = 1 \cdot 10^6 S/m$, $\varepsilon$=0.01 $C^2/Jm$ |

Figure 5.2: Right: Cross section of the cylindrical model electrode. R2 and R3 are the electrode and R1 is the electrolyte with the dimensions radius=height=1. Left: Physical properties of the different regions R1, R2 and R3.

## 5.3 Current constriction

The absolute potential distribution at the two limiting cases of a simulated impedance spectrum can be seen in figure 5.3 page 39. As shown in the figures, only the conducting ring electrode is active at low frequencies, while the whole disk electrode is active at high frequencies. Simulations of impedance

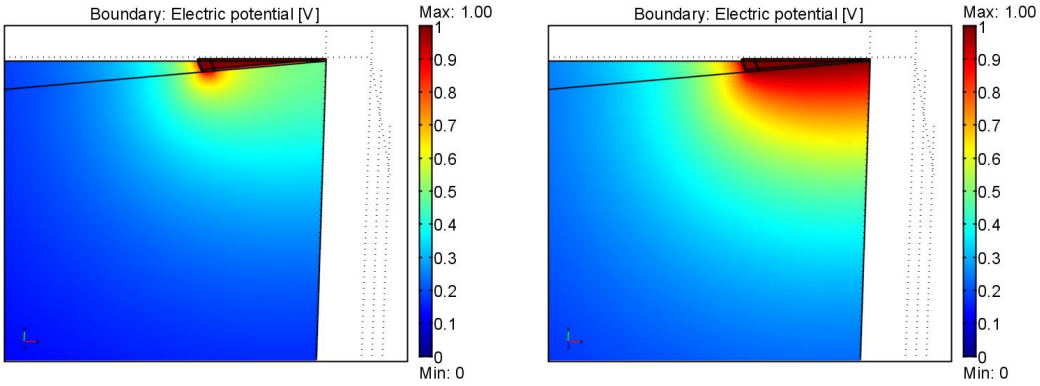


Figure 5.3: Tilted cake slice showing absolute potential $V = \sqrt{(Re(V))^2 + (Im(V))^2}$ distribution plots at different frequencies **Right**: 1mHz **Left**: 100Hz.

spectra for various width of the DC active ring electrode are shown in figure 5.4 page 40. $Z(freq. \rightarrow \infty)$ is the electrolyte resistance when the whole disk is active, and $Z(freq. \rightarrow 0)$ is the electrolyte resistance of the ring electrode at DC conditions. The common high frequency limit, of the simulated spectra, is in accordance with the predicted value in figure 5.1 page 37 for electrolyte dimensions height=radius=1. This corresponds to the Newman value for the given geometry, with the whole electrode/electrolyte interface at constant potential, confirming that the calculations are accurate. Very little is known about the extension of the TPB zone for pure electronic conducting cathodes, but it is generally believed to be of the length scale $1\mu$m, and most probably less. Typical point electrodes in SOFC studies have contact areas with a radius larger than $50\mu$m. This means that the width of the TPB zone is around, and in many cases smaller, than 1 percent of the radius. Figure 5.3 page 39 shows, when this is the case, the error in polarization resistance is of the same order of magnitude as the disk electrolyte resistance determined as $Z(freq. \rightarrow \infty)$. Great care should therefore be taken in the interpretation of impedance spectra of catalytic good electrodes with polarization resistances comparable to the $Z(freq. \rightarrow \infty)$ value. The current constriction effect can be neglected for catalytic poor electrodes with polarization resistances $R_p \gg Z(freq. \rightarrow \infty)$.

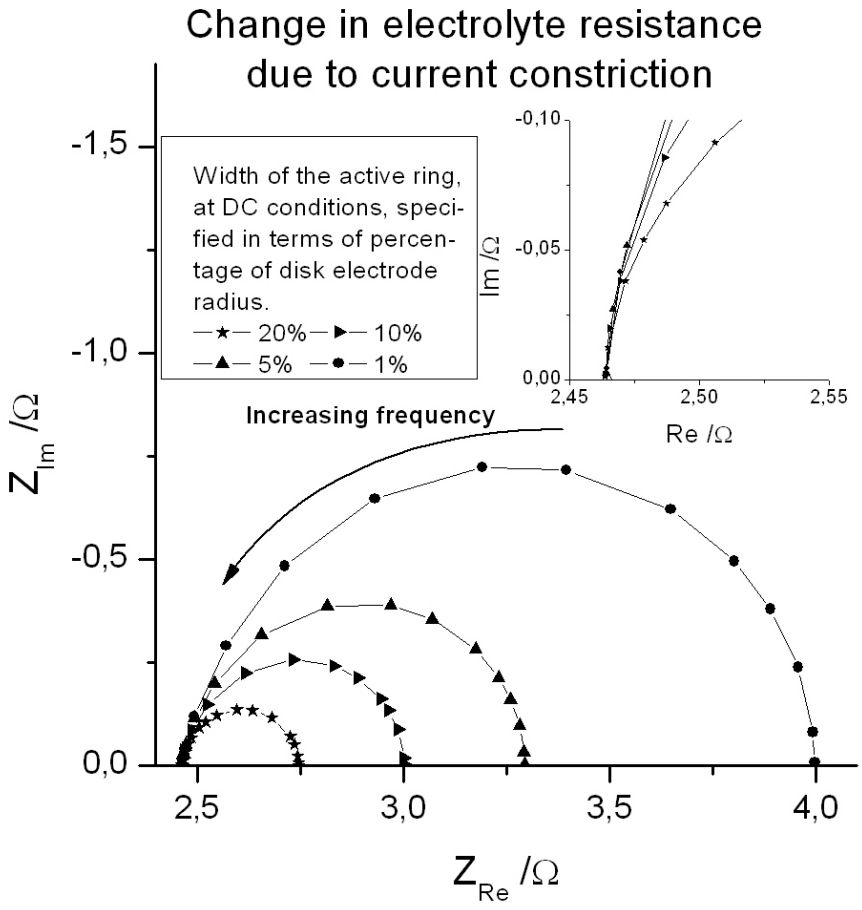


Figure 5.4: Simulated impedance spectra with different widths of the active ring electrode at DC conditions. The frequency range of the spectra is from 100Hz to 10mHz.

## 5.4 Influence of current distribution on the shape of impedance spectra

A closer inspection of the simulated impedance spectra presented in figure 5.4 page 40 reveals that the spectra are not ideal semicircles as the response of a resistor in series with a resistor in parallel with a capacitor, $R_1(R_2C)$ in Boukamp notation [51]. This is illustrated in figure 5.5 page 41 by fitting

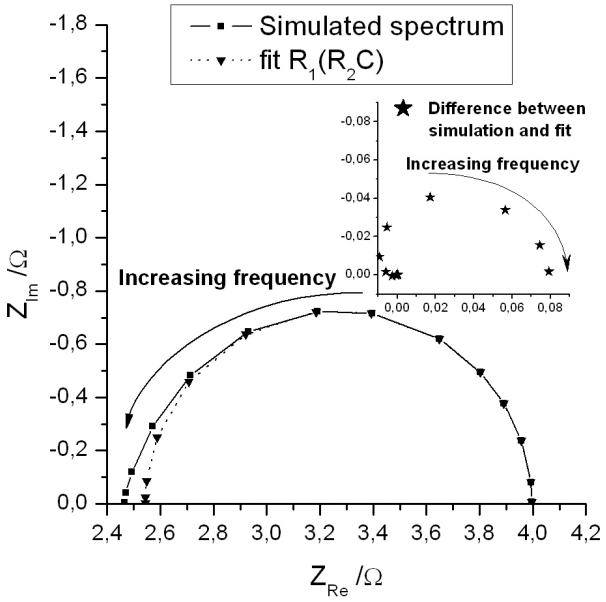


Figure 5.5: Simulated impedance spectrum of figure 5.4 page 40 with the low frequency part fitted with the equivalent circuit $R_1(R_2C)$.

the low frequency part with the equivalent circuit $R_1(R_2C)$, which shows an increasing deviation from moderate to high frequencies with the fit. The inset graph in the upper right corner of the figure shows a Nyquist plot of the difference between simulation and fit. The distortion from an ideal parallel coupling between a resistor and a capacitor is due to a change in the potential distribution of the electrode/electrolyte interface as function of frequency. At low frequencies the conducting part of the electrode determines the potential distribution with a corresponding electrolyte resistance $R_{3TB}$. At high frequencies it is the capacitive part of the electrode that determines the potential distribution, with a different electrolyte resistance $R_{2TB}$ than the low frequency electrolyte resistance. If the two potential distributions

were frequency independent and no interaction occurred, the response would be that of an ideal semicircle. This can be described with the equivalent circuit $R_{2PB}(\Delta RC)$, where $\Delta R = R_{3PB} - R_{2PB}$. However, interaction between the two limiting potential distributions do occur and frequency dependency does exist. This implies that $\Delta R$ and C changes as function of frequency, resulting in the distortion shown in figure 5.6 page 42. To illustrate a changing potential distribution as function of frequency, simulations have been carried out with the whole electrode active at DC conditions, but with the electrode conductivity reduced to 0.1S/m. The changing potential distribution is illustrated in figure 5.6 page 42. At low and moderate frequencies a clear

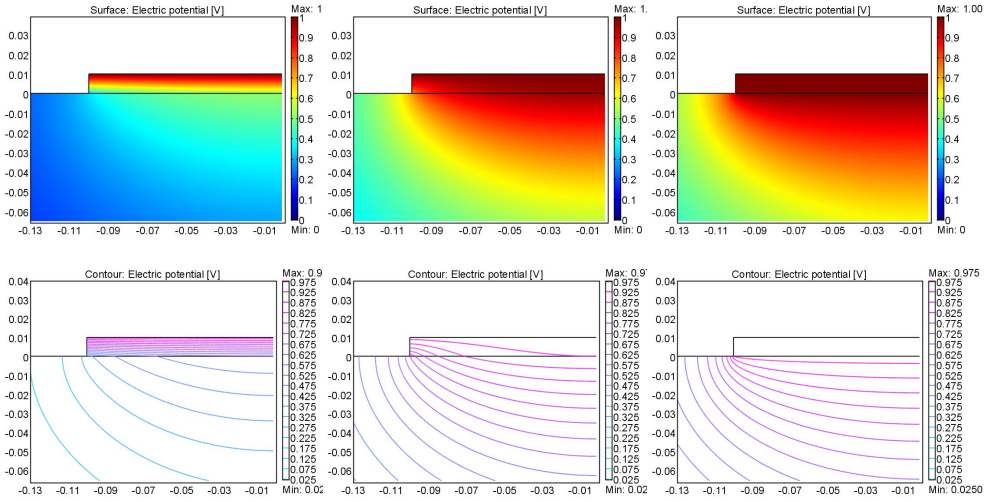


Figure 5.6: The absolute potential distribution at low, medium and high frequency of an impedance spectrum, with the whole electrode active at DC conditions, illustrating the changing potential distribution at the electrode/electrolyte interface. The upper row shows the potential distribution and the lower row shows equipotential lines.

bending of the equipotential lines is seen at the electrode edge, while the bending disappears at the high frequency limit of $freq. \rightarrow \infty$. The resulting shape of the impedance spectrum is similar to that of the spectrum in figure 5.6 page 42. If the edge effect is removed, and constant potential along the electrode/electrolyte interface is obtained in the two limiting situations of $freq. \rightarrow \infty$ and $freq. \rightarrow 0$, by changing the electrolyte media cylinder radius to that of the electrode radius, a perfect semicircle is obtained. The influence of a changing potential distribution on electrode parameters is clearly illustrated by doing impedance calculations on a pure capacitive electrode,

with the equivalent circuit $R_{electrolyte}C$ and the associated impedance:

$$Z_{total} = R_{electrolyte}(\nu) + \frac{1}{i\omega C(\nu)} \tag{5.16}$$

The calculated impedance is shown in the Nyquist impedance plot in the left figure of figure 5.7 page 43. At very low frequencies the behavior is ideal with a vertical line shifted $R_{electrolyte}$. As the frequency is increased, a clear change of $R_{electrolyte}$ is observed. The right figure of figure 5.7 page 43 shows the $R_{electrolyte}$ along with capacitance change as function of frequency. Two very clear plateaus are observed, corresponding to a constant potential distributions at low and high frequency with a shift in between the two limiting situations.

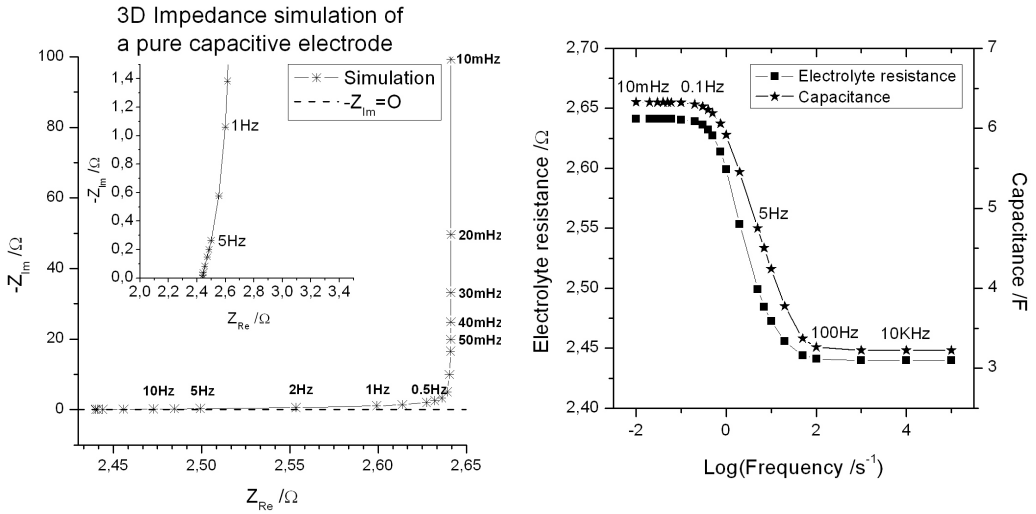


Figure 5.7: **Left:** Impedance of a pure capacitive electrode. **Right:** Electrolyte resistance and capacitance as function of frequency. The capacitance is calculated from the imaginary part of the impedance $C = 1/\omega(-Z_{Im})$.

## 5.5 Comparison with Literature

J. Fleig and J. Maier have made 2D impedance FEM simulations of modelled imperfect contacted electrodes by ascribing a thin air gap with constant thickness, a permittivity $\varepsilon_{Airgap}$ and the electrolyte a permittivity $\varepsilon_{electrolyte}$ and a conductivity $\sigma_{electrolyte}$ [52]. The result were impedance spectra with two overlapping semicircles that were claimed to consist of two perfect semicircles in series. However, reconstruction of the geometry with the stated

parameters, and setting the electrolyte permittivity $\varepsilon_{electrolyte} = 0$, reveals a similar distorted semicircle as the one shown in figure 5.6 page 42. Generally, the permittivity of the electrolyte $\varepsilon_{electrolyte}$ and the associated capacitance is of no interest, since it is extremely small and out of experimental reach due to the large capacitor plate separation in real measurements. Further, the selected geometry makes the electrolyte permittivity $\varepsilon_{electrolyte}$ behave as that of a perfect plate capacitor, and an perfect semicircle is achieved. Finally, Fleig and Maier made 2D simulations on a geometry with an nonlinear increasing air gap. This resulted in a clear distorted semicircle at high frequencies in agreement with the shape of the impedance spectra in figure 5.4 page 40 and the interpretation in section 5.4 page 41.

## 5.6 Simulated impedance spectra of films with lateral ohmic resistance

The cross section of the revolved model electrode geometry, chosen for investigations of the impedance response of films with lateral ohmic resistance, is shown in the upper left image of figure 5.8 page 47. The geometry is chosen so it resembles the geometry of the LSM films presented in section 8.2.3 page 122. The material properties of the different regions are represented by $\sigma 1$, $\sigma 2$, $\sigma 3$, $\sigma 4$ and $\varepsilon$. $\sigma$ is representing conductivity, while $\varepsilon$ is representing permittivity. The chosen electrolyte conductivity $\sigma 4$ value is an typical value for YSZ at $1000^0 C$. The remaining values are chosen so that the $freq. \rightarrow 0$ resistance and the capacitance determined from the low frequency semicircle are close to those estimated from impedance measurements on the LSM films presented in section 8.2.3 page 122. The upper right impedance spectrum of figure 5.8 page 47 shows a situation with some lateral resistance. Two semicircles are observed. The images in figure 5.9 page 48 shows the equipotential surfaces at selected frequencies. At a high frequency of 1MHz it is primarily the permittivity of the electrode that supplies the current and a constant potential throughout the electrode is achieved, meaning that Newmans formula 5.15 page 37 is valid. The 100Hz potential distribution corresponds to the situation where a shift from the high frequency semicircle to the low frequency semicircle in the impedance spectrum is observed. Significant lateral resistance is present, but by careful inspection it is possible to observe that the equipotential surfaces in the lateral direction is slightly bend forward in the permittivity layer compared to the conducting layer. This means that at this frequency and higher the current originating from the permittivity begins to have a magnitude that determines the potential distribution. At a very low frequency of 10mHz the electrostatic potential distribution is achieved, and the potential distribution of a ring electrode is observed.

The high frequency semicircle therefore corresponds to the shift from the electrostatic conducting parts of the electrode determining the potential distribution to the situation where it is the current originating from the permittivity thats determining the potential distribution. From figure 5.9 page 48 it can be seen that at the beginning of the high frequency semicircle 100Hz only a small part of the electrode is active. At the end of the high frequency semicircle 1MHz the whole electrode is active. The change in percentage of the electrode being active is associated with a change in electrolyte resistance. From the plot in figure 5.10 page 48, of the resistance according to Newmans formula as function of radius, it can be seen that the 100Hz resis-

tance corresponds to the situation where 40 percent of the electrode radius is active.
The resistance of the low frequency semicircle, that is the diameter of the semicircle, is the sum of lateral resistance ($\sigma 1$), reaction resistance ($\sigma 3$) and change in electrolyte resistance from the 10mHz to the 100Hz situation. Simulation of mixed conductivity by setting $\sigma 2 \neq 0$ lowers not surprisingly the total low frequency resistance, but leaves the high frequency semicircle intact. From the fit of the low frequency semicircle with a capacitor in parallel with a resistor deviation at the high frequency part of the semicircle can be observed. From the investigations presented in section 5.4 page 41 it can be concluded that the deviation represents a coupling between the potential distribution from the electrostatic conducting part and the potential distribution originating from the permittivity. Increasing the lateral resistance of the film significantly increases the coupling between the two different potential distributions as can be observed in the two impedance spectra presented in lower part of figure 5.8 page 47.
The question of key importance with respect to the impedance spectra presented in figure 5.8 page 47 is of course whether the layer with isotropic permittivity resembles the properties of the electrochemical double layer. The electrochemical double layer has a certain degree of anisotropy since it is positively charged on one side of the interface and negatively charged on the other side. Nevertheless the lateral resistance results in a non uniform polarization of the interface, thus a difference in charge in the lateral direction of the interface, which will give rise to a lateral current in the electrochemical double layer.

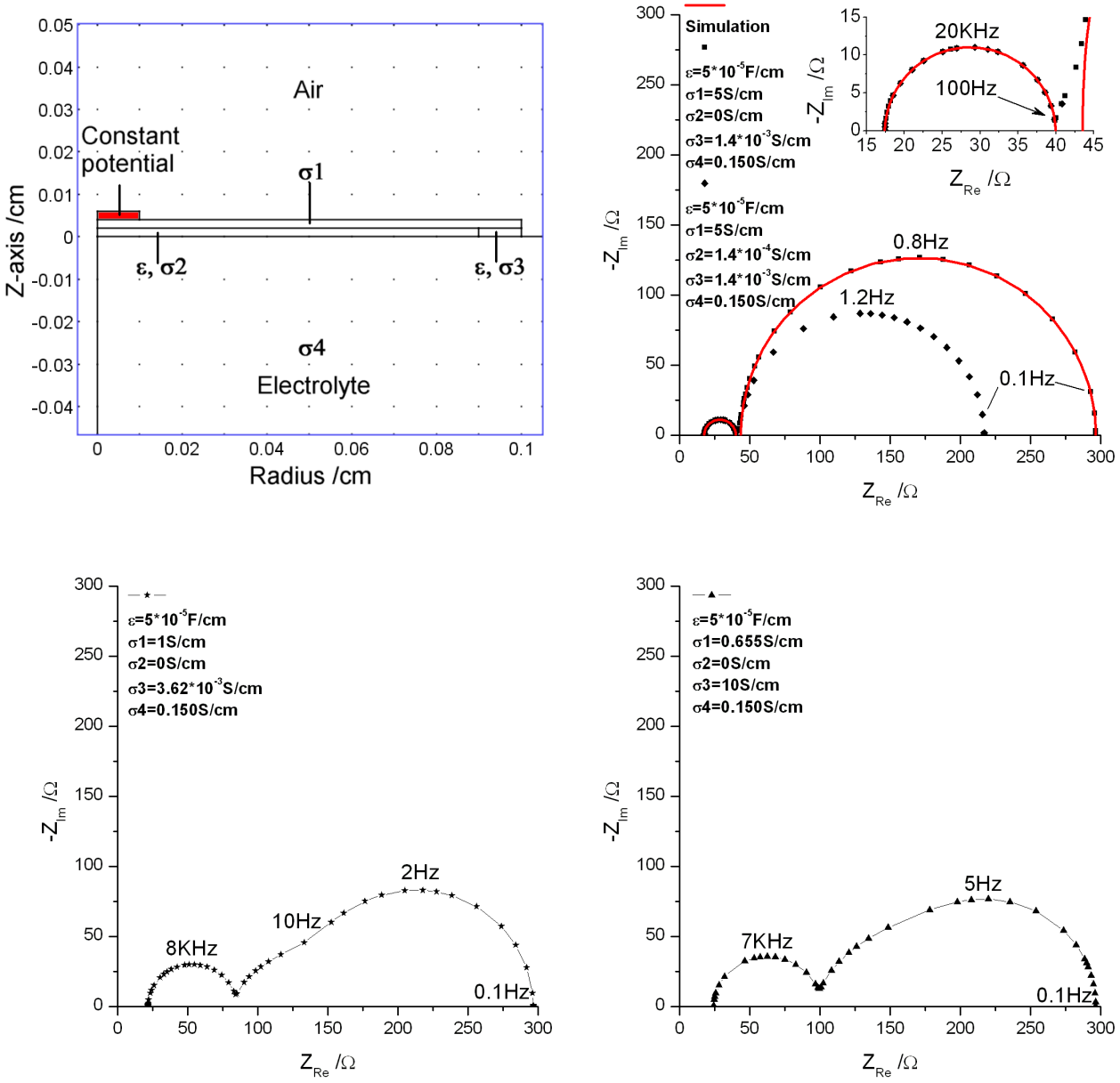


Figure 5.8: **Upper left:** Image of the cross section of the revolved model electrode geometry. **Upper right:** Simulated situations with and without mixed conductivity. Mixed conductivity is modelled by setting $\sigma 2 \neq 0$. The high frequency semicircle in the situation without mixed conductivity was fitted with a CPE parallel coupled with a resistor, while the low frequency semicircle was fitted with a capacitor in parrallel with a resistor. The fitted parameters are as following: $Q_{high} = 3.902 * 10^{-7}$, $\alpha = 0.9863$, $R_{high} = 22.56\Omega$ and $C_{Low} = 7.801 * 10^{-4}F$, $R_{Low} = 43.51\Omega$. **Lower left:** Impedance spectrum of the situation with increased lateral resistance. **Lower right:** Impedance spectrum with maximum lateral resistance without changing the $freq. \rightarrow 0$ resistance.

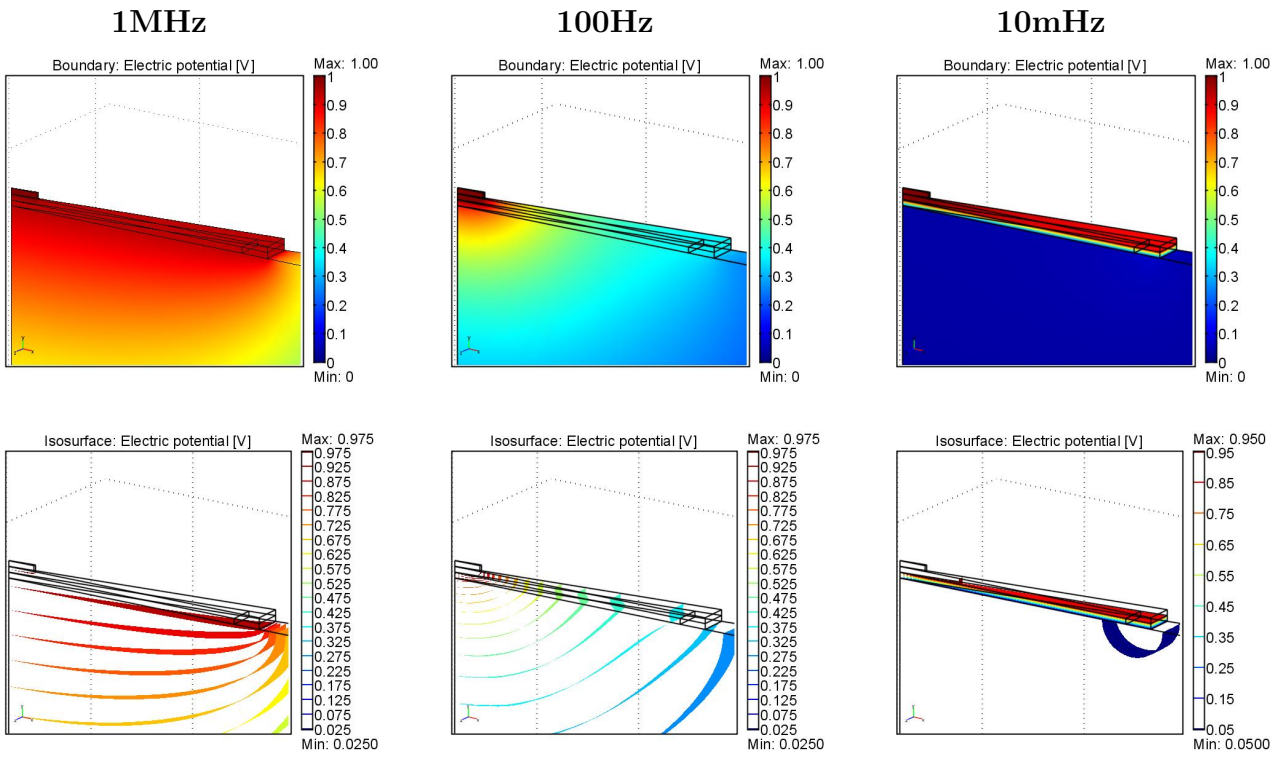


Figure 5.9: Contour plots and equipotential surfaces plots of the absolute potential at selected frequencies of the situation in the upper right image of figure 5.8 page 47.

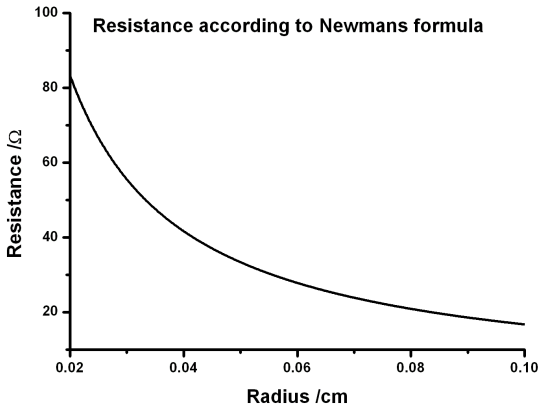


Figure 5.10: Constriction resistance of a desk according to Newmans formula as function of desk radius. The chosen electrolyte conductivity is 0.150S/cm.

# Chapter 6

# Platinum microelectrodes

## 6.1 Article

### Three-phase-boundary dynamics at Pt/YSZ microelectrodes

J. Nielsen, T. Jacobsen

Published in:
**Solid State Ionics 178 (2007) 1001-1009**

Available online at www.sciencedirect.com
ScienceDirect
Solid State Ionics 178 (2007) 1001 – 1009
SOLID STATE IONICS
www.elsevier.com/locate/ssi

# Three-phase-boundary dynamics at Pt/YSZ microelectrodes

J. Nielsen *, T. Jacobsen

*Department of Chemistry, Technical University of Denmark, DK-2800, Denmark*

Received 31 October 2006; received in revised form 13 March 2007; accepted 22 March 2007

**Abstract**

Strong electrode activation, inductive hysteresis and non-linearity are well-known phenomena on model Pt-YSZ cathodes, and recently also a regular current fluctuation pattern have been reported. The oxygen electrode reaction with YSZ as electrolyte is studied at Pt microelectrodes prepared by electrochemical etching of platinum wire. The result is a well-defined contact area of ~25 μm in diameter. Due to the small size and a favourable ratio between the three-phase-boundary (TPB) length and the contact area, microelectrodes should have an increased sensitivity to local events at the TPB compared to larger point electrodes normally applied. The electrode processes are studied by potential sweep, step and impedance techniques. Investigation of the YSZ and Pt surfaces afterwards reveals the growth of dendrite-like Pt structures from the TPB. The formation of these structures can explain the observed regular current fluctuation pattern and contributes to the explanation of the activation phenomena of the model Pt-YSZ and SOFC cathodes.


*Keywords:* SOFC; Microelectrodes; Three-Phase-Boundary (TPB); Pt cathode; Surface migration

## 1. Introduction

For improvement of solid oxide fuel cells (SOFC) knowledge of the oxygen electrode reaction is of great interest since it often is the limiting factor for the overall performance of the cell. In this respect platinum electrodes on yttria stabilized zirconia (YSZ) has been widely accepted as a useful foundation on which to build the understanding of SOFC cathodes. One obvious advantage of Pt electrodes compared to modern ceramic and more complex mixed conduction cathodes is the expected chemical inertness and the confinement of the electrode reaction to three-phase-boundary (TPB) region. In spite of the expected simplicity compared to ceramic SOFC cathodes, the details of the reaction are by no means fully understood. Strong activation upon moderate to high polarization is observed, resulting in non-linearity and inductive hysteresis in linear sweep voltammetry, even for sweep rates as low as 1 μV/s [1]. Lately, a characteristic saw-tooth-like noise pattern has also been identified [5]. Studies of the contact area between electrode and electrolyte have shown that changes at/near the TPB and interface itself take place [2–4]. Activation phenomena have also been reported for $La_{1-x}Sr_xMnO_3$ electrodes [6,8] and for the hydrogen electrode reaction at Ni|YSZ electrodes [7]. These observations strongly suggest that more careful studies of the electrode reaction and the induced morphological changes are needed. The aim of the present work is to contribute to this by a microelectrode study utilizing needle shaped Pt electrodes prepared by electrochemical etching. Due to extensive creeping upon contact with the polished YSZ tablet a well defined interface area is achieved enabling a reliable correlation between morphological changes and electrochemical response. Furthermore, microelectrodes give a more favourable TPB/area ratio and smaller TPB length, compared to normal larger point electrodes, and is thus expected to exhibit a higher sensitivity towards local events at the TPB.

## 2. Experimental

Pt microelectrodes with a contact area of ~25 μm in diameter were prepared by electrochemical etching of Pt wire. This was done by applying a 50-Hz AC voltage with 35 V amplitude to a Pt wire in an aqueous solution containing 40 vol.% of a saturated calcium chloride solution at room temperature [15]. After electrochemical etching the electrodes were cleaned in an ultrasonic bath with water and ethanol. The electrodes were mounted in a thin alumina tube inside another alumina tube (1 mm Ø) positioned a few millimetres

* Corresponding author. Tel.: +45 45252438.
*E-mail address:* jim@kemi.dtu.dk (J. Nielsen).

0167-2738/$ - see front matter © 2007 Elsevier B.V. All rights reserved.
doi:10.1016/j.ssi.2007.03.007

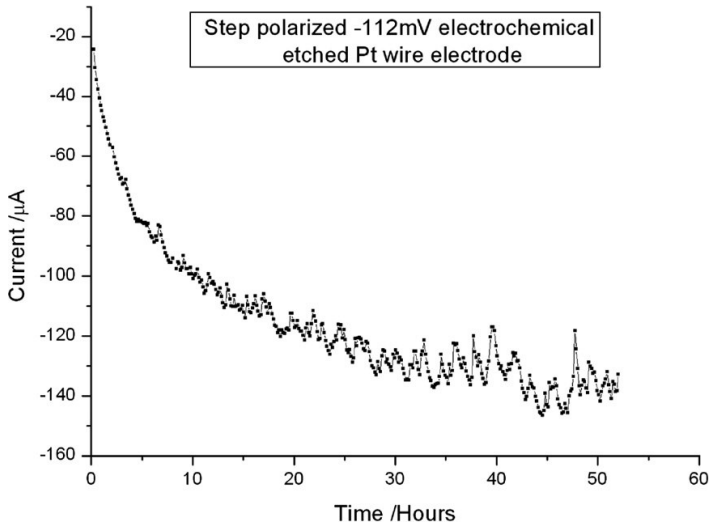


Fig. 1. Potential step from 0 to −112 mV of Pt electrochemical etched wire microelectrode on YSZ at 1000 °C in air.

above a polished (3µm diamond paste) 8% Yttria Stabilized Zirconia (YSZ) tablet, and the whole assembly was placed inside a tubular furnace and heated. At 1000 °C the electrodes were gently lowered and allowed to touch the electrolyte (YSZ). The weight on the electrodes was in between 2.5 and 6 g. The electrolyte tablets were equipped with Pt painted reference and counter electrodes as described in [3]. During measurements, air saturated with water at room temperature was passed through the furnace. The electrodes were allowed to creep until a stationary state had been reached before the electrochemical experiments were initiated. The characteristic time for reaching a stationary contact area was estimated by monitoring the electrolyte resistance with impedance spectroscopy.

50 Hz noise from the heating coils of the furnace was reduced as described in [3]. Step polarization and data requisition was done using a Hewlett Packard 75000/potentiostat/PC setup. The potentiostat used and PC software were of own construction. When the step polarization experiments were continuously monitored with impedance spectroscopy a Gamry FAS2 Femtostat potentiostat was used. The frequency range was 100 KHz–1 Hz with an AC amplitude of 25 mV RMS. The high frequency region was corrected with a measured standard curve constructed from measurements on resistances with values chosen close to the experimental values.

The impedance results were analysed using an electrolyte resistance $R_e$ in series with a polarization resistance $R_p$ in parallel with a constant phase element, $Q$, $(R_pQ)R_e$ in Boukamp notation [9]. Fitting was done with a laboratory developed program that enables automatic fitting of a series of impedance spectra with a given equivalent circuit.

## 3. Results

Fig. 1 shows the development of an electrochemical etched Pt wire microelectrode step polarized −112 mV. As expected, a strong activation of the electrode is seen resulting in an apparently steady-state current that is 7 times larger than the initial level. On closer inspection a slowly increasing fluctuation pattern during activation is also seen. This illustrates the higher sensitivity of microelectrodes towards discrete events at TPB compared to previous observations with larger electrodes [3,5]. On large electrodes the discrete events at TPB that gives rise to the fluctuation pattern are damped by averaging over a large TPB length. Furthermore, microelectrodes give a more correct impedance response of the processes of interest at TPB since a relative larger part of the electrode–electrolyte interface is involved in the process. On large single point and porous electrodes the processes at TPB are heavily damped by interfacial capacity of the otherwise passive interface and the part of the TPB not participating. Fig. 2 shows SEM images of the contact area on the electrolyte YSZ surface after the experiment. The hole in the middle of the branched pattern is from the rip off of the electrode. The images show very clearly that Pt has migrated from the electrode and formed what could be described as a 2-dimensional dendrite-like structure. An unquestionable identification of the dendrites being Pt by EDS is difficult due to strong overlap with peaks from yttrium and zirconium. However, SEM confirms that the dendrites are highly conductive. Beside this, the dendrites can only be removed by use of hot (70 °C) aqua regia. The surface of migrated Pt looks very smooth and rounded off with some droplets ranging from nm to µm in diameter. There is no crystalline tendency, almost as if it had been a liquid. But this cannot be the case, since the experiments have been conducted at 1000 °C, i.e. far from the melting point of Pt (1768 °C). Even though the polarization has been maintained during cooling of the furnace the cooling rate may have been too slow (~200 °C/h) to assure a quenching of the structure at 1000 °C. Therefore it cannot be ruled out entirely that the structure at 1000 °C has changed during cooling, probably to a structure with a larger degree of

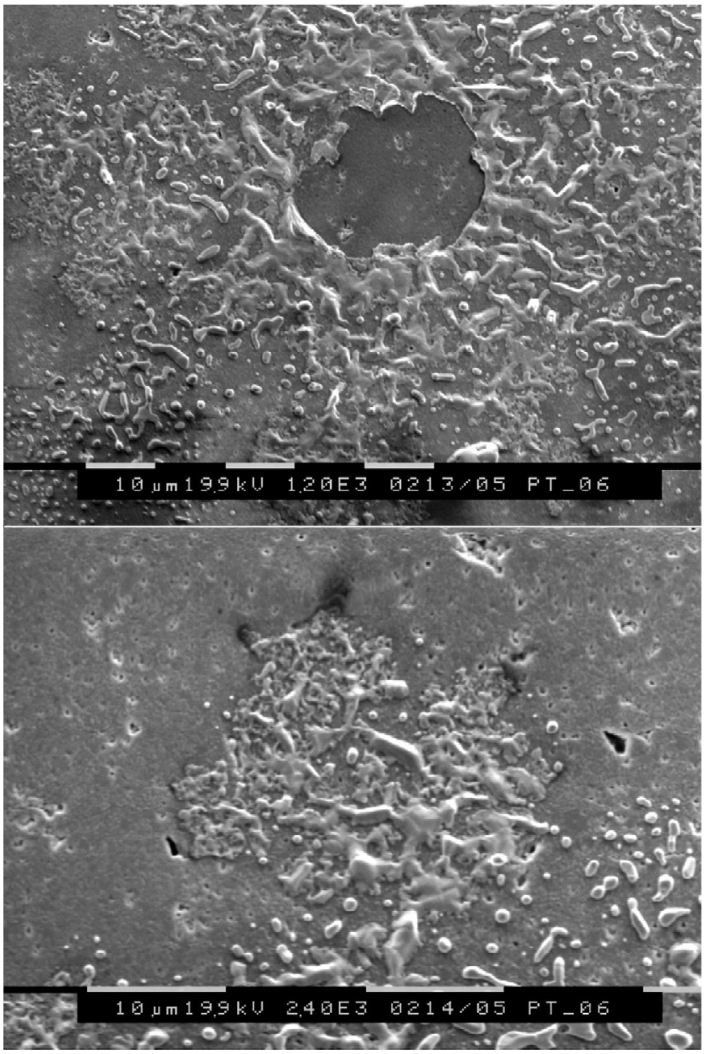


Fig. 2. SEM images of YSZ surface of disassembled Pt electrode–YSZ contact after experiment presented in Fig. 1.

isolated islands. The relative large increase of TPB length caused by the Pt migration explains the activation phenomena, and as will be discussed later also the observed fluctuation pattern.

Fig. 3 shows an electrochemical etched Pt wire microelectrode that has been subjected to a stronger polarization of −250 mV. Here the fluctuation pattern is very distinct with a characteristic saw-tooth-like look. This strongly confirms the recent observations in [5] where it is argued that the fluctuation pattern from Pt electrodes has a characteristic shape and not random. Fig. 3 removes any doubt with respect to this. From the onset of the fluctuation pattern at 25 h to the end of experiment at 260 h a general deactivation of the electrode is seen.

Overall measurements have been performed on 30 Pt electrodes on YSZ tablets. Some of these experiments have been performed on YSZ tablets prepared from powder of different vendors, meaning that the surface composition with respect to impurities etc. is expected to be different for some of the YSZ tablets. The sintering temperature has been varied (1300–1700 °C) as well. In all cases the electrodes showed inductive hysteresis in linear potential sweeps and activation behavior upon step polarization. Every time the contact area has been inspected by optical microscope or SEM Pt migration has been observed. The same Pt migration electrochemical characteristic on YSZ has also been observed on $Ce_{0.9}Gd_{0.1}O_{1.95}$ and $Ce_{0.6}Gd_{0.4}O_{1.8}$ (CG) tablets [14]. This indicates that Pt migration is not critically dependent on the chemical surface composition. However, there is some difference in how pronounced the activation is from electrode to electrode. In some cases the activation following step polarization was poor. Fig. 4 shows linear potential sweeps of an electrode that showed a poor activation with no detectable saw-

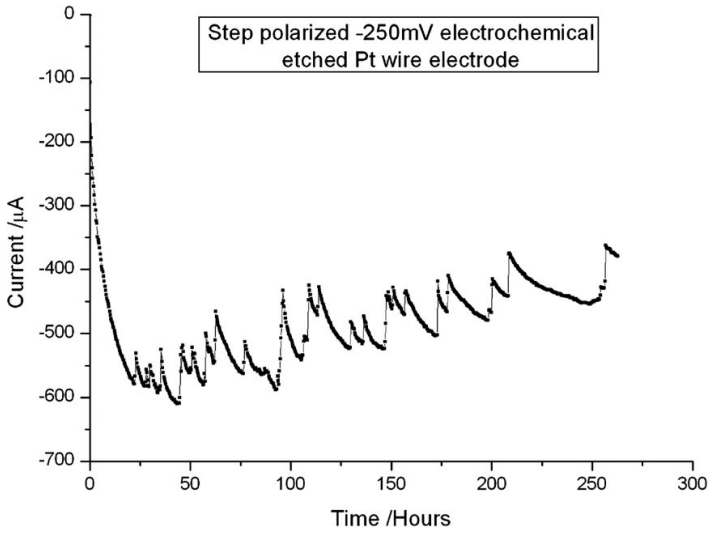


Fig. 3. Potential step from 0 to −250 mV of Pt electrochemical etched wire microelectrode on YSZ at 1000 °C in air.

tooth-like fluctuation pattern when step polarized to −112 mV. The potential was then swept from the higher step polarization potential (−112 mV) to −300 mV three times. The first two sweeps were with a sweep rate of 5μV/s and the final sweep with a rate of 1 μV/s. The 5-μV/s sweeps showed as expected inductive hysteresis though with a few abrupt changes in current near the end of the sweeps. At ultra-slow potential sweep rate (1 μV/s) the electrode begins to show the characteristic saw-tooth fluctuation pattern with a less open current loop. This, together with the representative step polarization responses shown in Figs. 1 and 3, suggests that the characteristic fluctuation pattern is correlated with the electrode being close to a steady-state. A common feature for all measurements seems to be that the electrodes cannot be reactivated to the same level as in the initial activation process.

The changes in electrode area due to Pt migration can be monitored as changes in electrolyte resistance with impedance spectroscopy. Results of a 100-μV/s potential sweep on a fresh electrode can be seen in Fig. 5 which shows a quantitative correlation between the current and electrode area in the cathodic polarized region. In the anodic polarized region a capacitive loop is

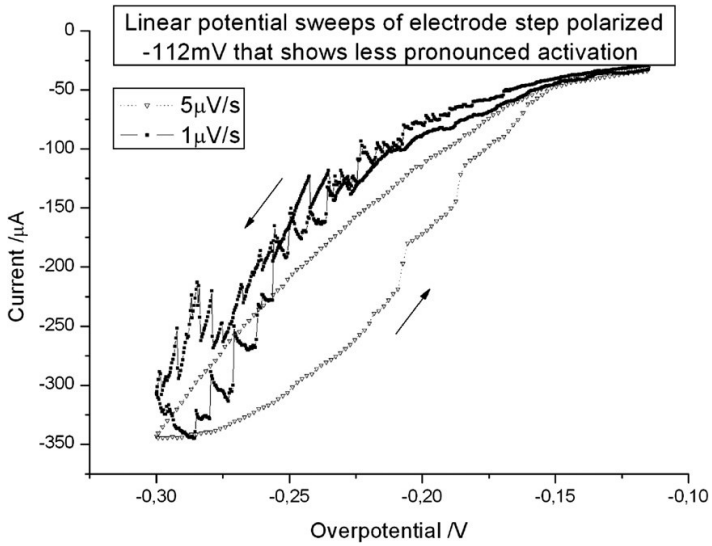


Fig. 4. Linear potential sweeps from −112 mV to −300 mV of electrode that showed poor activation upon step polarization from 0 to −112 mV at 1000 °C in air.

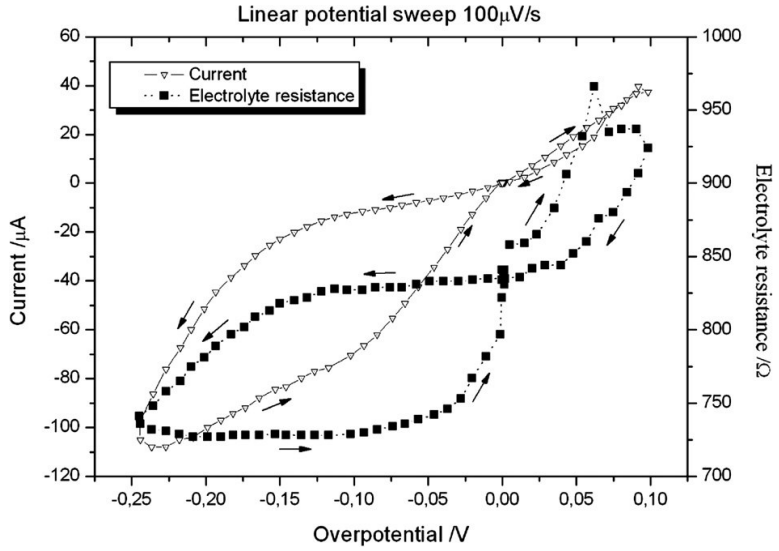


Fig. 5. Linear potential 100 μV/s sweep on a fresh Pt electrochemical etched wire microelectrode on YSZ with changes in electrolyte resistance monitored with impedance spectroscopy at 1000 °C in air.

observed with the current being larger on the forward sweep compared to the return sweep. The difference in current between forward and return sweep is also in this region well correlated with changes in electrolyte resistance. The capacitative behavior is most likely due to the fact that at anodic polarization oxygen is pumped to the electrode. A 100-mV polarization relative to equilibrium potential in air corresponds to a rather high oxygen partial pressure of 8 atm underneath the electrode which may reduce the interfacial contact. After the sweep in Fig. 5 the electrode was allowed to relax 4 h before a sweep was performed in opposite sweep direction showing a similar behavior as in Fig. 5. The electrode was allowed to relax 24 h and a 2-μV/s sweep was conducted. During the last

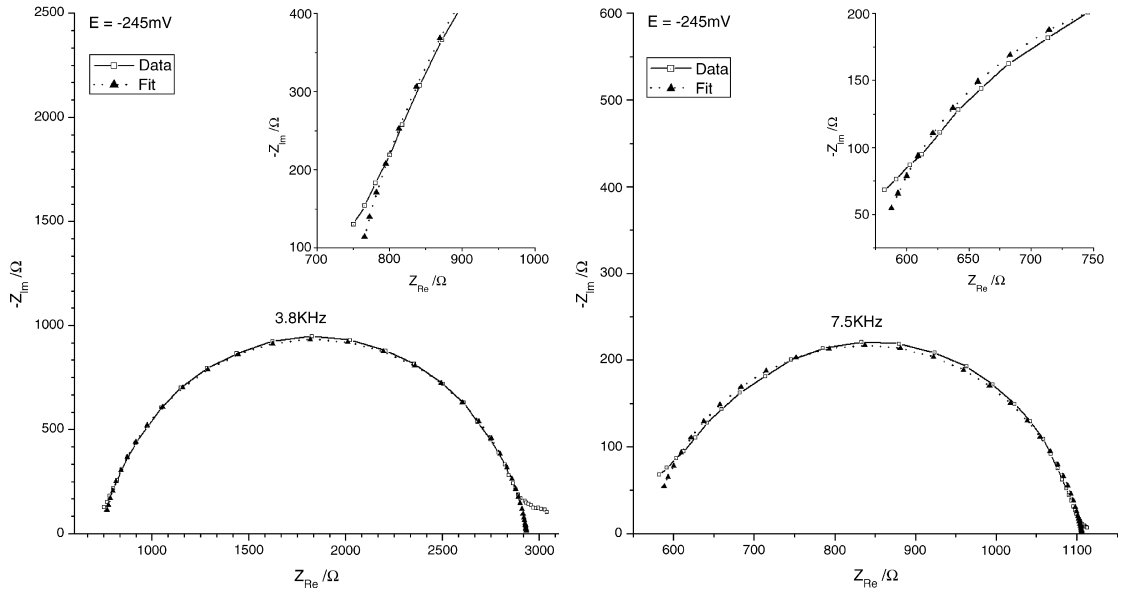


Fig. 6. Representative impedance spectra showing the change in impedance response during sweeps of the electrode presented in Figs. 5. and 7 fitted with $(R_pQ)R_e$ equivalent circuit. Left: typical impedance spectrum of the initial 100 μV/s sweeps (fit parameters $R_e$=740, $R_p$=2193, $Q=5.43\times10^{-8}$ and $\alpha$=0.90). Right: typical impedance spectrum after the maximum cathodic polarization of the final 2 μV/s sweep (fit parameters $R_e$=570, $R_p$=536, $Q=1.65\times10^{-7}$ and $\alpha$=0.87).

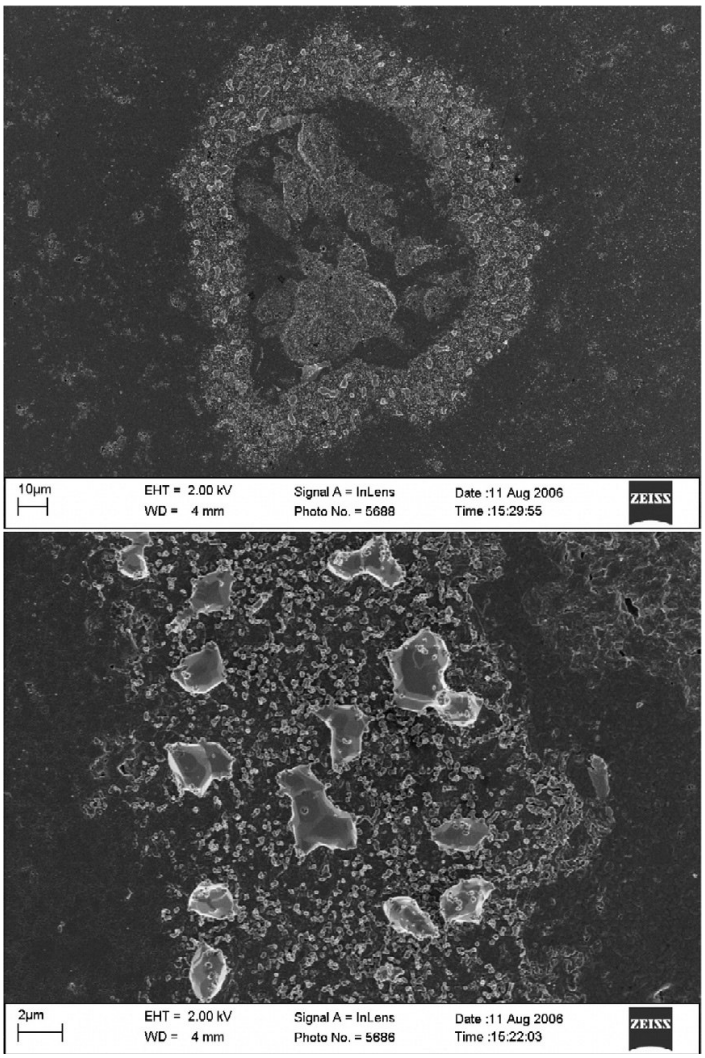


Fig. 7. SEM image of YSZ surface of disassembled Pt electrode–YSZ contact after experiments presented in Figs. 5 and 6.

sweep the impedance spectrum changed in the cathodic polarized region to a somewhat more asymmetrical shape as shown in Fig. 6. The asymmetrical shape was after the slow sweep permanent. A SEM image of the electrolyte surface afterwards can be seen in Fig. 7. The central crater is from the rip off of the electrode and the crystalline particles with a diameter of 1–2 µm in the ring around the crater, is Pt migrated during the potential sweeps. Treatment with aqua regia at 75 °C etched away the Pt, but the porous ring with particles of 100–200 nm in diameter remained. Since permanent shape change of the impedance spectra occurred during the very slow sweep (2 µV/s) and similar aqua regia etching experiments of −250 mV step polarized electrodes also shows non-Pt induced porosity, it indicates that another slower activation mechanism probably takes place at high cathodic polarizations (lower than ~−112 mV) besides the activation with Pt migration. The relaxations in between potential sweeps were also monitored with impedance spectroscopy and showed that at OCV the electrolyte resistance increased towards a certain value indicating a passive breakup/loss of electronic contact to the migrated Pt. The migration of Pt and the following break up seems to change the surface maybe by reorganization of the surface impurities, which could explain the less pronounced activation upon reactivation.

In Fig. 8 the current for a fresh activated microelectrode calculated as $i_{cal}=\eta/(R_{electrolyte}+R_{polarization})$ is compared to the changes in current measured. The agreement implies that the impedance describes the full cell response hence there are no frequency dependent elements at lower frequencies. Fig. 9 is a comparison of the same current fluctuations shown in Fig. 8 with fluctuations in electrolyte resistance estimated from impedance spectra. Since the major $R_{electrolyte}$ fluctuations are approximately

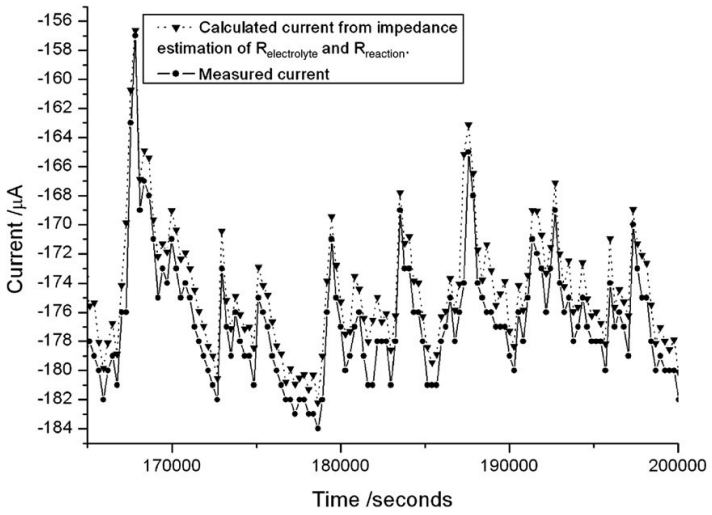


Fig. 8. Comparison of measured current and current calculated as $i=\eta/(R_{\text{electrolyte}}+R_{\text{reaction}})$ for a fresh activated Pt electrochemical wire microelectrode on YSZ at 1000 °C in air.

synchronous with the measured fluctuations in current it seems reasonable to conclude that a correlation between cathodic current fluctuations and electrode area, or rather the length of the TPB, exits.

## 4. Discussion

The very distinct saw-tooth like fluctuation pattern seen in Fig. 3 with the images of Pt migration in Fig. 2 in mind suggests that the abrupt decrease in current is due to loss of electronic contact to migrated Pt. The cut off of thin film like migrated Pt is probably caused by surface tension forces. The electronic unconnected migrated Pt could then further break up into islands. If no further break up occurs, an abrupt increase in current would be expected as contact to the lost electrode area is reestablished. Since the current increases gradually and Pt droplets are seen in Fig. 2 a tempting picture of the fluctuation mechanism is that at a certain time a considerable part of the Pt migration structure loses electronic contact to the electrode, probably due to surface forces. When left at equilibrium conditions the Pt film breaks up into circular islands. Since the islands are left at the equilibrium potential the concentration of oxidized Pt species, presumably Pt-oxygen complexes dissolved in a surface impurity film in the

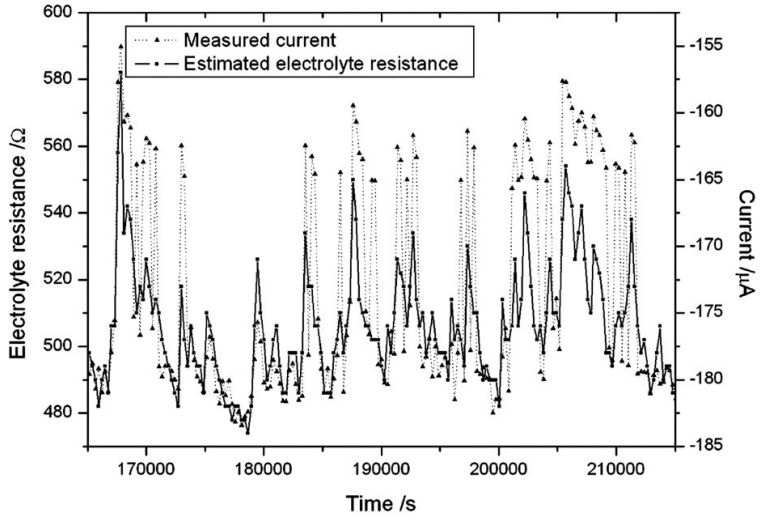


Fig. 9. Comparison of fluctuations in measured current with impedance estimated electrolyte resistance for the electrode presented in Fig. 8.

vicinity of a Pt island, will be higher than at the polarized Pt electrode. Thus isolated island will be dissolved and redeposit as dendrites on the nearest Pt surface which is in electronic contact with the polarized and the structure will slowly be reestablished. The correlation shown in Fig. 9 confirms this hypothesis, that the observed current fluctuation pattern of Pt electrodes is due to loss of electrode area and as a consequence TPB length. This suggests that the migrated Pt film is somehow stabilized when polarized. This is supported by Fig. 4 where the current return to the initial level after the sweeps. The large hysteresis in the 5-μV/s sweep compared to the 1-μV/s sweep shows that steady state conditions have not been reached, even at these low sweep rates. Fig. 5 shows a steep increase in electrolyte resistance as zero the equilibrium potential is approached from the cathodic region, this supports the picture of the Pt migration pattern breaking up, while the electrode is not polarized.

As already mentioned, the fluctuation pattern seems to be related to the electrode being close to or at a steady-state. In this respect it is important to keep in mind that the geometry change from a disk to a dendrite-like structure of the electrode upon activation changes the potential drop distribution across the reaction and electrolyte. Segregation of impurities from the bulk to the surface increases the electrolyte resistance at TPB. Influence of eventual migration of impurities to or from the TPB reaction zone is in this respect not clear. The segregation of impurities and morphological changes at/near the electrode–electrolyte interface reported previously [3] are expected to change the potential drop across the reaction zone. These processes proceed on a larger timescale and cannot be responsible for the fluctuations, but they may be involved in the apparently constant slow deactivation from 24 h in Fig. 3.

Generally there are two possible mechanisms for the formation of the Pt structure. It can either be through a gas phase or a surface transport mechanism. It is well known that chromium from interconnect materials can form volatile species that by gas phase are transported to the TPB of the electrode where they are reduced and block the electrode reaction [11–13]. Recently Pt migration from Pt current collectors have been reported to cause performance changes of La(Sr)$FeO_3$–SOFC cathodes [10]. In these investigations Pt migration was suspected to be caused by gas phase transport of Pt oxide to the TPB though no definitive migration mechanism was given. At 1000 °C in air the partial pressure of $PtO_2$(g) is in the order of $10^{-7}$ bar [16]. It is difficult to judge whether gas phase transport is likely to be the explanation based on this partial pressure of $PtO_2$(g) since the air flow in the furnace also plays an important role. No contamination of Pt along TPB on other electrodes such as strontium substituted lanthanum manganite electrodes from use of Pt wires and Pt paste counter and reference electrodes has been observed in the present work. But the diffusion path, from the closest Pt source to TPB, is much longer than in the Pt electrode case. If gas phase transport is responsible for the formation of the dendrite the significant difference in activation between individual Pt electrodes is unexpected. There will always be a negative overvoltage at the TPB that would reduce gaseous Pt-O species in equilibrium with the $PtO_2$ interface and increase the TPB of the Pt structure on the YSZ surface. This would most likely increase the TPB/current and not lead to a deactivation of the electrode as seen in Fig. 3. Further reactivation of the electrode to the same level as the initial activation with time would be expected if gas phase transport is the mechanism. These arguments suggest that gas phase transport is not the mechanism for the migration of Pt or at least not the complete picture.

A surface transport mechanism on the other hand would have a surface composition dependency. The dendrite like structure of the migrated Pt suggests that the transport mechanism depends on the potential or the current distribution. Locally sharp points along the electrode perimeter would, with a potential dependent growth mechanism, have a higher growth rate than a smooth electrode perimeter. Such a growth mechanism could give a dendrite like structure as observed. Thinking of potential dependent surface transport mechanisms charged Pt species dissolved in an impurity film on the YSZ surface could be responsible. But this is quite speculative and more conclusive experiments are obviously needed.

However, Pt migration cannot account for similar but less distinct activation behaviour observed for $La_{1-x}Sr_xMnO_3$ electrodes and the hydrogen electrode reaction at Ni|YSZ. This indicates that another activation mechanism or mechanisms are taking place but for Pt electrodes these are overshadowed by Pt migration.

## 5. Conclusion

Electrochemically etched Pt wire microelectrodes have proven to be useful in investigations of the dynamical structural changes at TPB upon polarization, with their higher sensitivity towards discrete events at the TPB. Pt migration was observed and can explain the electrochemical behaviour with a strong activation and accentuated current fluctuation pattern. The interpretation that the observed fluctuation pattern was due to changes in electrode contact area was supported by impedance spectroscopy data. Pronounced inductive hysteresis in linear potential sweeps is also observed at 900 °C and can be observed down to around 750 °C meaning that Pt electrodes may not serve as a good model system for the SOFC cathode in this temperature range. However, a better understanding of the fundamental mechanism behind the Pt migration is still of interest since Pt electrodes have often been used in kinetic studies and Pt paste and leads are widely used in experimental SOFC studies.

## Acknowledgement

This work is part of the research project “Efficient conversion of renewable energy by solid oxide cells” financed by The Danish Ministry of Science Technology and Innovation. Discussions with colleagues at Risø National Lab are greatly appreciated.

## References

[1] T. Jacobsen, B. Zachau-Christensen, L. Bay, M. Jorgensen, Electrochim. Acta 46 (2001) 1019.
[2] B. Luersen, J. Janek, S. Günther, M. Kiskinova, R. Imbihl, Phys. Chem. Phys. 4 (2002) 2673.
[3] L. Bay, T. Jacobsen, Solid State Ionics 93 (1997) 201.
[4] D.A. Emery, P.H. Middleton, I.S. Metcalfe, Surf. Sci. 405 (1998) 308.

[5] T. Jacobsen, K. Vels Hansen, E. Skou, J. Electrochem. Soc. 152 (11) (2005) A2203.
[6] Y. Jiang, S. Wang, Y. Zhang, J. Yan, W. Li, J. Electrochem. Soc. 145 (1998) 373.
[7] R.J. Aaberg, R. Tunold, M. Mogensen, R.W. Berg, R. Ødegård, J. Electrochem. Soc. 145 (1998) 2244.
[8] M. Odgaard, E. Skou, Solid State Ionics 86–88 (1996) 1217.
[9] B.A. Boukamp, Solid State Ionics 20 (1986) 31.
[10] S.P. Simmer, M.D. Anderson, L.R. Pederson, J.W. Stevenson, J. Electrochem. Soc. 152 (9) (2005) A1851.
[11] S.P.S. Badwal, R. Deller, K. Foger, Y. Ramprakash, J.P. Zhang, Solid State Ionics 99 (1997) 297.
[12] Y. Matsuzaki, I. Yasuda, Solid State Ionics 132 (2000) 271.
[13] K. Hilpert, D. Das, M. Miller, D.H. Peck, R. Weib, J. Electrochem. Soc. 143 (1996) 3642.
[14] L. Bay, Ph.D. thesis, Technical University of Denmark, (1998).
[15] A.J. Nam, A. Teren, T.A. Lusby, A.J. Melmed, J. Vac. Sci. Technol. B 13 (4) (1995) 1556.
[16] K. Hesselmann, O. Kubaschewski, O. Knacke, Thermochemical properties of inorganic substances, 2. editionSpringer, 1991.

## 6.2 Additional results with platinum

### 6.2.1 Transport mechanism of migrated Pt

In an attempt to determine whether the transport mechanism of migrated Pt is a surface or a gas phase transport mechanism, the experiment presented in last part of the article "TPB dynamics at metal/YSZ microelectrodes" page 84 was constructed. The basic idea is to have a Pt reservoir within the micrometer scale, in a controlled manor, of the TPB of a cathodic polarized LSM electrode. This is achieved by deposition of a slightly shifted Pt film on top of a LSM film as shown in the upper part of figure 6.1 page 59. The whole assembly is contacted with a gold point electrode and polarized at $1000^0C$. After 7 hours the furnace was turned off. The electrode remained polarized during cooling. EDS along and EDS Pt mapping of the LSM film

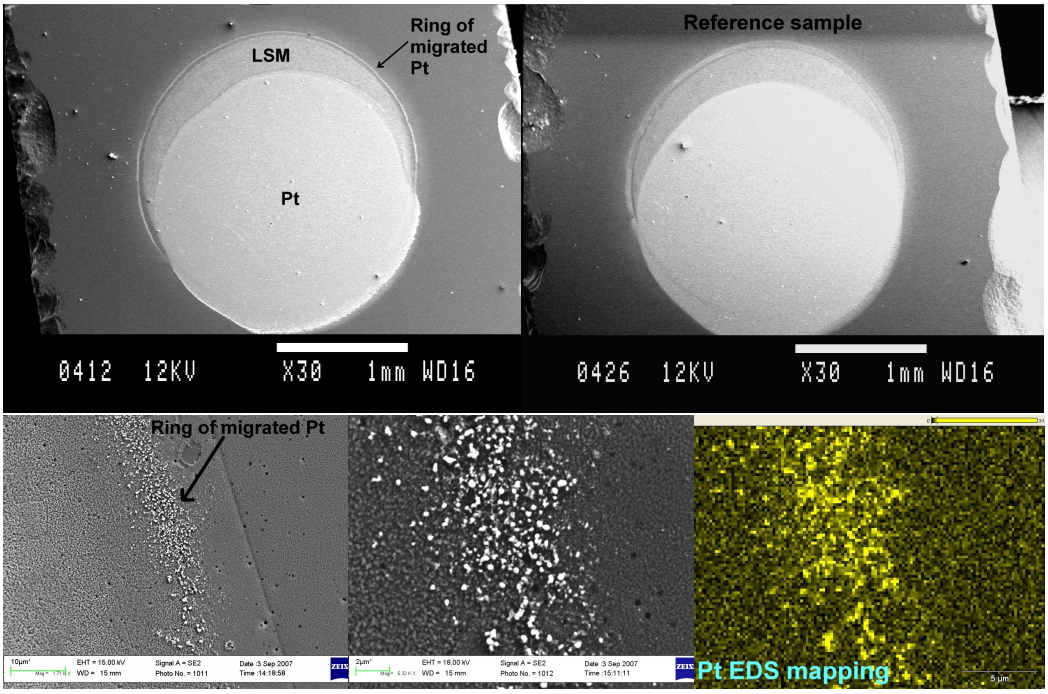


Figure 6.1: The upper part shows images of Pt/LSM film samples while lower part shows images and Pt EDS mapping of the LSM perimeter after experiment.

perimeter reveals unambiguously the presence of Pt. An EDS spectrum of pure Pt along with a typical spectrum of a point along the LSM perimeter is shown in figure 6.2 page 60 while the lower part of figure 6.1 page 59 shows EDS Pt mapping and SEM images of the perimeter. The presence

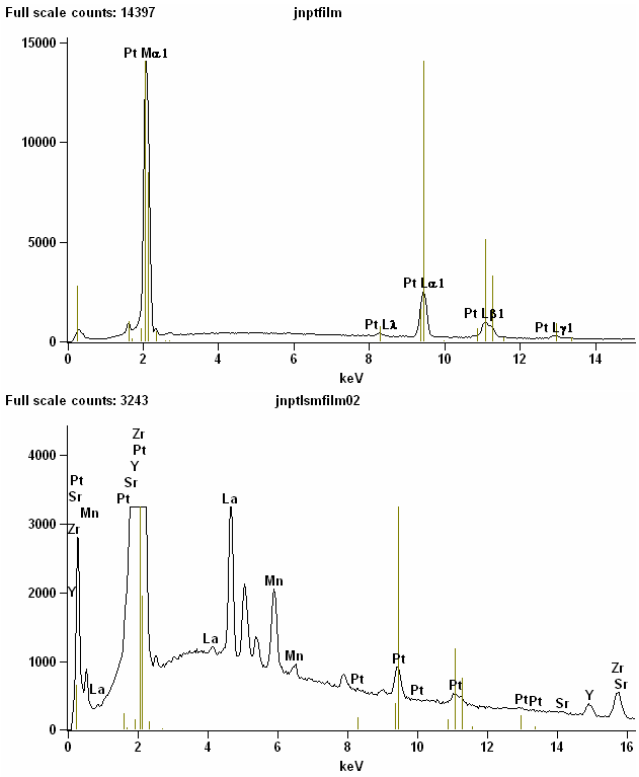


Figure 6.2: Top: EDS spectrum of pure Pt. Bottom: Typical EDS spectrum along the LSM TPB of the polarized Pt/LSM film sample shown in figure 6.1 page 59. The vertical lines show the energy location of Pt EDS peaks and the length of the vertical lines represent the mutual intensity between the different Pt peaks.

of Pt along the LSM perimeter suggest that Pt is transported through the gas phase as $PtO_2(g)$ and reduced by the cathodic polarization at the LSM TPB. It seems highly unlikely that any surface transport mechanism can account for the Pt at the LSM TPB, especially when taking the transported distance ($\sim 300\mu m$) into account. The complete evaporation of migrated Pt in the temperature treatment experiments, presented in figure 7.1 page 83, provides further evidence of a gas phase transport mechanism. The temperature treatment experiments of migrated Pt show that evaporation is part of the deactivation mechanism, since it is shown that the migrated Pt evaporates completely during the timescale of the Pt experiments. Evaporation along with passive breakup of the deposited film composes the deactivation mechanism.

### 6.2.2 Morphology of migrated Pt

Figure 6.3 page 61 and figure 6.4 page 62 show representative high resolution FEG-SEM closeup images of migrated Pt from Pt electrodes. These images

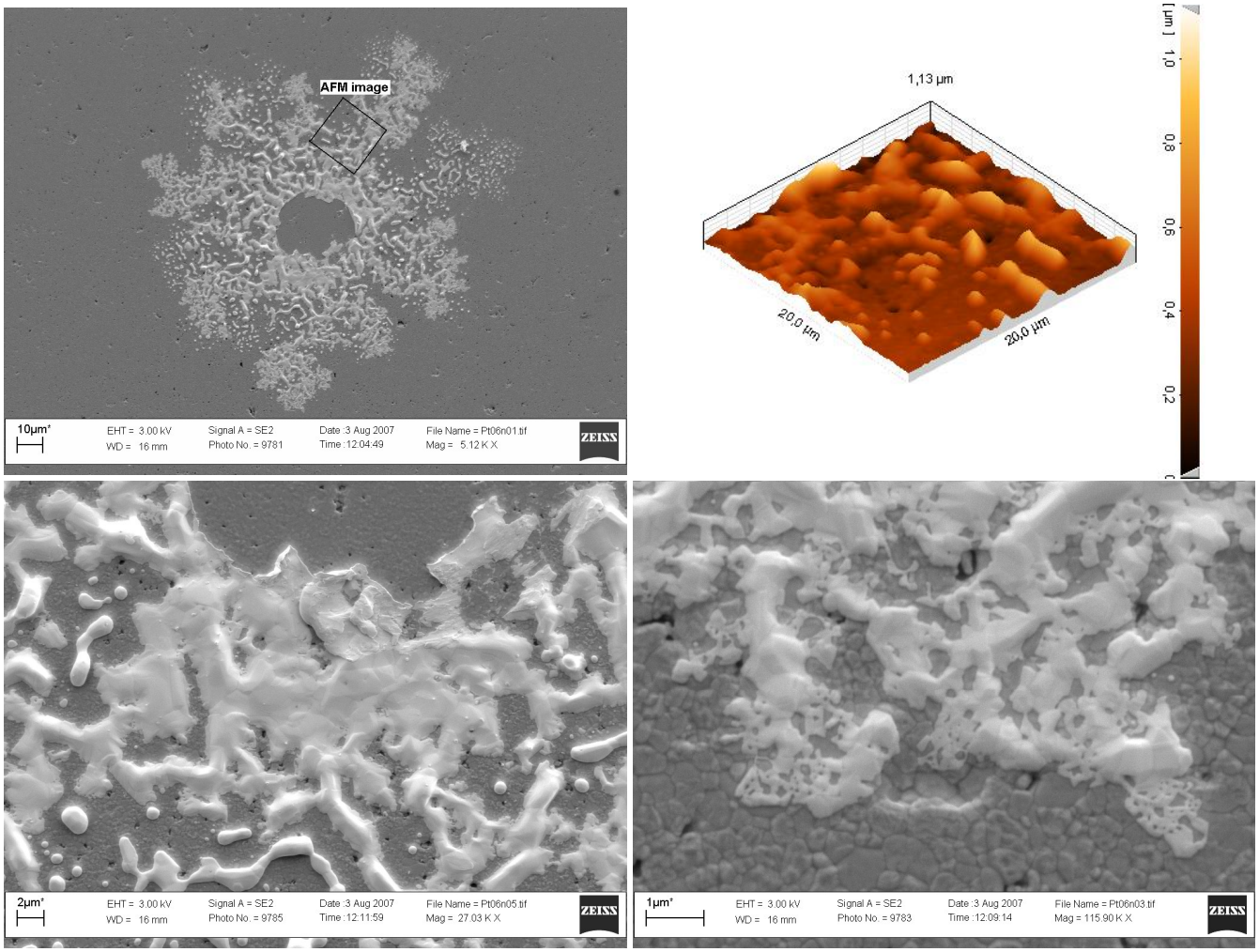


Figure 6.3: FEG-SEM images and AFM image of the Pt06 sample which is presented in the Pt article.

show that the migrated Pt do show a crystalline tendency and that parts of the migrated Pt have a film like look, but on closer inspection holes are observed at the thinner areas of the apparent film. The AFM 3D image in figure 6.3 page 61 gives a coarse estimation of the typical thickness of the migrated Pt to be in the range from 200nm to 600nm. Peaks of the migrated Pt are found to have a maximum thickness of $\sim 1\mu m$. The lower left image

of figure 6.3 page 61 shows examples of elongated Pt droplets that look like they are just about to break up into two separate droplets due to surface tension forces. Figure 6.5 page 64 shows initial smooth and geometrically well

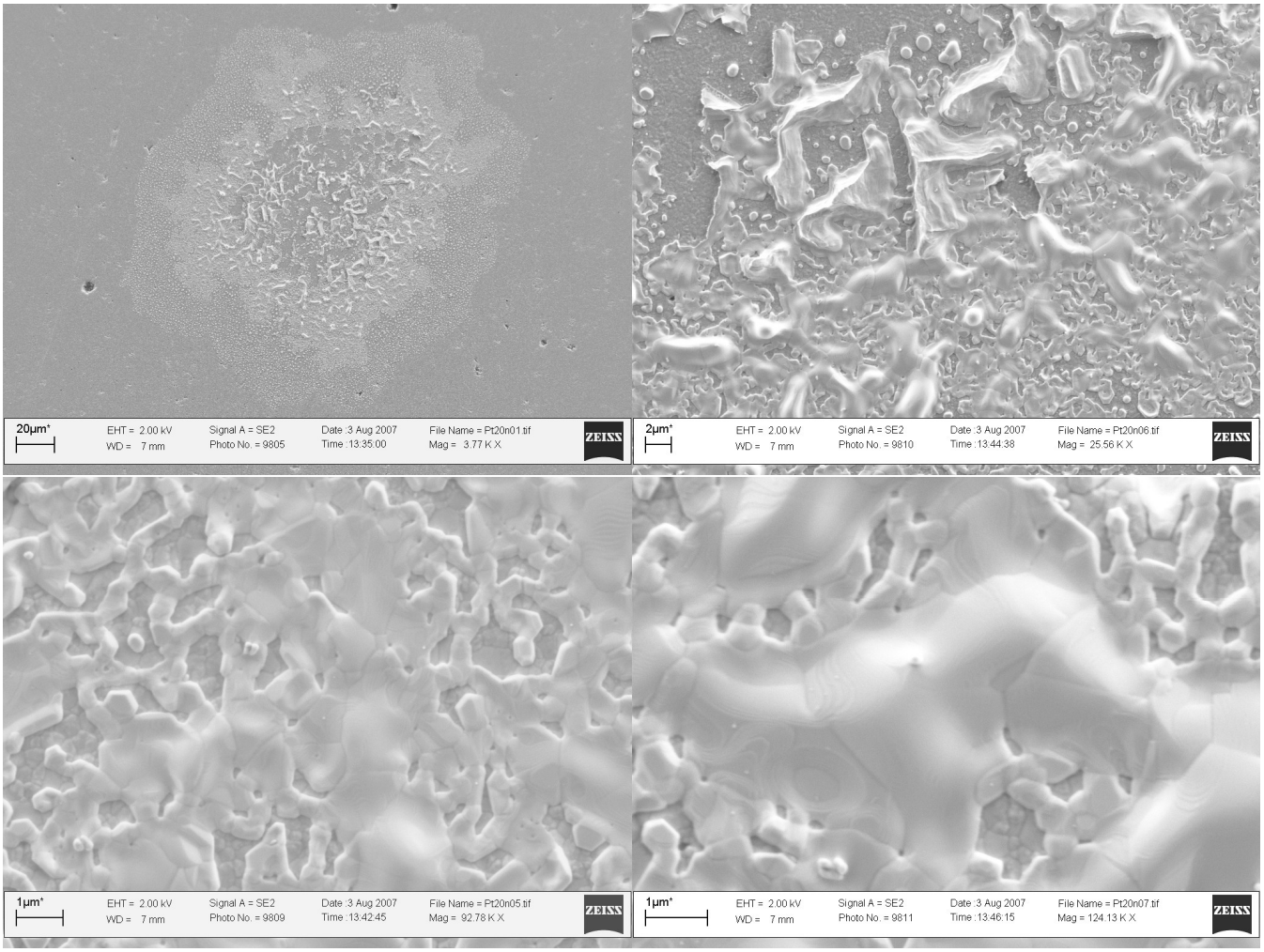


Figure 6.4: FEG-SEM images of sample Pt20 showing the structure of migrated Pt.

defined Pt films, deposited by PLD and heat treated at $1000^0C$ for 7 hours. The images show that the perimeter of the films has become frayed. Moving from the perimeter towards the center of the films a very frayed morphology with Pt droplets is seen at the perimeter. Then there is a shift to a Pt meshy structure which is followed by a smooth Pt film with a few holes and finally a smooth Pt film is observed. Similar break up of Pt films at $800^0C$ has been observed in [53]. Dependent on the chemical surroundings (wetting properties), thin films may not be thermodynamically stable. It is well known that

thin Pt films are not thermodynamically stable under the typical conditions in the experiments of the present thesis. Thermodynamics is not the only parameter that determines whether a film will break up. The kinetics of the break up has to be fast enough. Similar elongated Pt droplets, just about to break up into two separate droplets, as for the migrated Pt in figure 6.3 page 61 and figure 6.4 page 62, can be observed in the passive break up of the Pt films in figure 6.5 page 64. The similarities between the appearance of the migrated Pt and the heat treated thin Pt films suggest, that the migrated Pt is originally deposited as a film. However, due to thermodynamics, the film breaks up into the morphology observed in figure 6.3 page 61 and figure 6.4 page 62. This explanation is in agreement with the observed changes in electrolyte resistance during polarization presented in the article. The difference in current progression between the reported -112mV and -250mV step polarization experiments, in the article, with a more pronounced saw-tooth like behavior of the -250mV polarized electrode, can be explained with a more rapid Pt film growth for the -250mV polarized electrode than the -112mV polarized electrode. The initially formed Pt film has in both cases a certain thickness, and hence a certain lifetime, before it breaks up into islands. When the breakup occurs, the -250mV polarized electrode loses contact to a larger film, which causes a more pronounced saw-tooth like current fluctuation, than in the case of the -112mV polarized electrode. The fact, that loss of electronic contact to a large proportion of the formed Pt film is able to occur, might very well be correlated with the directional dependent growth of the Pt films. This will become more evident in the next section.

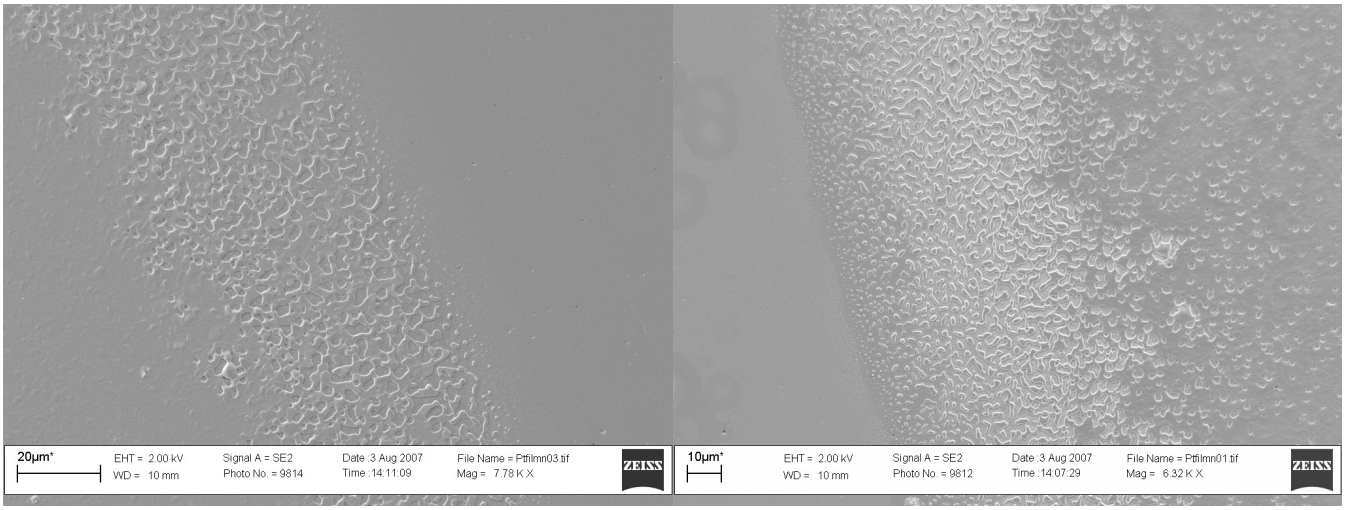


Figure 6.5: Two different PLD deposited Pt films that were heat treated at $1000^0C$ for approximately 7 hours.

### 6.2.3 Impurities

The step polarized -250mV electrochemical etched Pt wire microelectrode presented in figure 6.6 page 66 shows no saw-tooth like current fluctuation as the similar polarized electrode presented on page 53. The decrease in electrolyte resistance, and hence increase in contact area, seems to follow the increase in current with time. An inspection of the contact area, after experiment and removal of the electrode by rip off, reveals the images in figure 6.6 page 66. The images show extensive and evenly distributed migration of Pt from the perimeter of the original electrode. The even distribution of the migrated Pt from the perimeter of the original electrode reduces the probability, that migrated Pt loses complete electronic contact to the polarized electrode. The initial part of the deposited film, that breaks up into islands, is the oldest deposited part. That is, the part close to the perimeter of the original electrode. For electrodes with directional dependent Pt film growth, the resulting dendritic outgrown Pt is cut off as the inner part of the dendrites break up into islands. This loss of active electrode is prevented for electrodes with a homogeneous Pt outgrowth, since electronic contact is maintained due to the electronic contact perpendicular to the outgrowth direction. This can explain why some of the electrodes show characteristic saw-tooth like current fluctuations while other electrodes do not.
The closeup images on figure 6.6 page 66 reveal, beside crystalline Pt, the presence of fine grained, approximately 100nm sized, presumable impurity

particles. The presence of agglomerates made up of impurity particles is highly correlated with the presence of Pt. The non-contact YSZ area seems unchanged with a smooth surface. The dynamics, with break up of the Pt film and the passage of current, has an unknown impact on the transport of impurities. Electrophoresis might be involved. Each row in figure 6.7 page 67 shows images of a Pt electrode showing Pt migration, but also pronounced presence of impurities. The first row is that of the electrode presented in the Pt article in the figure on page 55. The first image in the first row is a closeup image of the migrated Pt along with impurity particles. The remaining two images in the first row show the contact area after the Pt has been removed by dissolution in $75^0C$ aqua regia. The images show that the suspected impurity particles are still present after the treatment. By a closer inspection it is also possible to see indentations in the YSZ surface where the Pt crystallites used to be. This could indicate that the YSZ surface is covered by an impurity film. Attempts to identify the composition of the suspected impurity particles and film by use of EDS have been unsuccessful. The particles are simply too small and the film too thin compared to the EDS interaction volume of approximately $1\mu m^3$. However, the presence of an impurity film and a rim ridge along the perimeter of the Pt crystallites are in accordance with results on anode model Ni point electrodes [54, 55, 56]. The second row of figure 6.7 page 67 is also a Pt microelectrode subjected to impedance monitored slow ($100\mu V/s$) linear potential sweeps. This shows the same general trends with an outgrowth of Pt and a pronounced presence of impurities. The last row of the figure shows images of the contact area of the -250mV step polarized electrode presented in the Pt article page 53. The first image in the row shows Pt migration and the following two images are after removal of Pt by dissolution in aqua regia showing the same trends as the electrodes in the rows above with presence of impurities, but also indentations as in the right image of the top row.

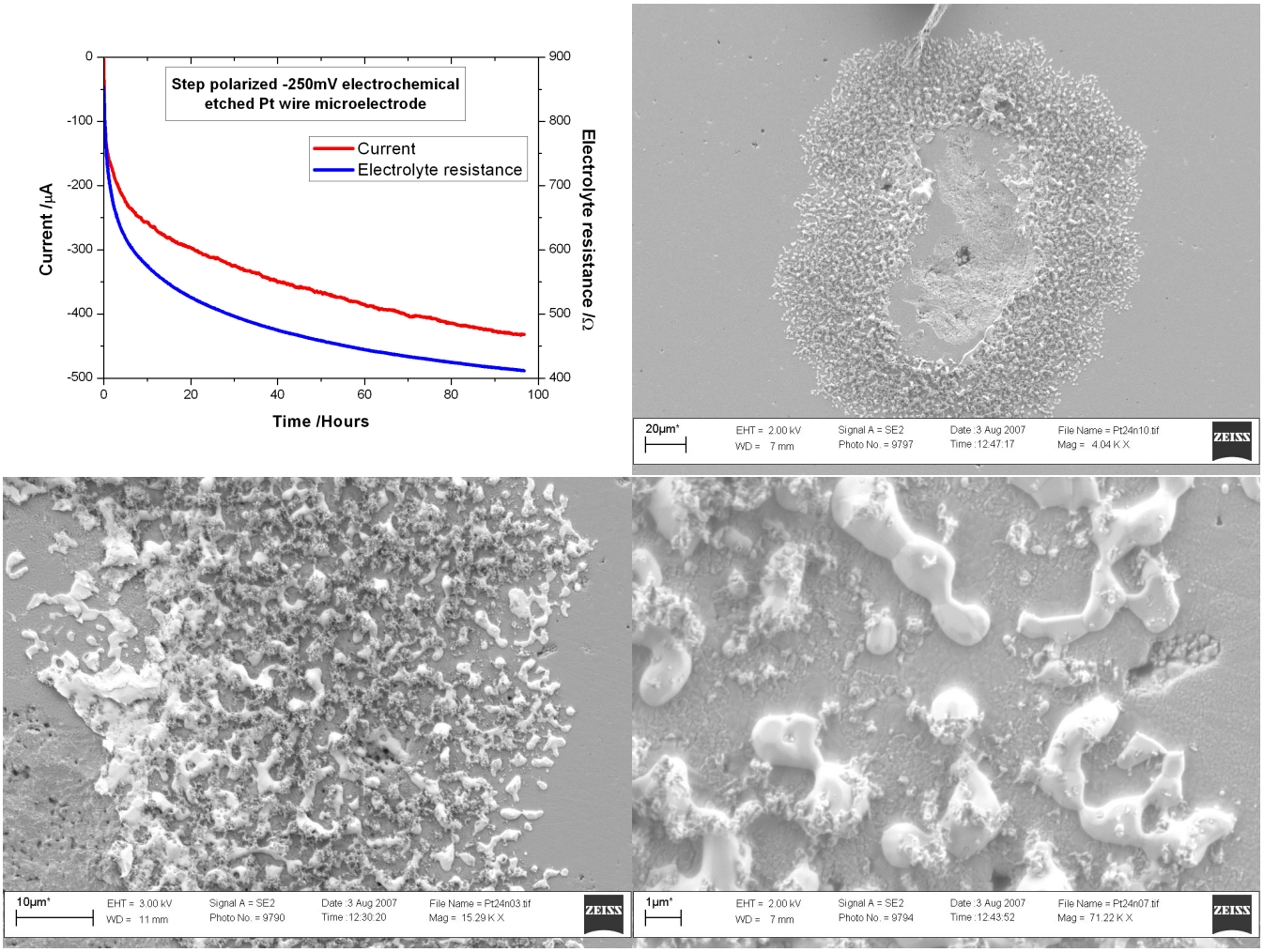


Figure 6.6: Microelectrode sample Pt24 step polarized -250mV with the resulting current and electrolyte resistance progression shown in the upper left image. The remaining images are of the contact area after experiment and removal of the Pt microelectrode by rip off.

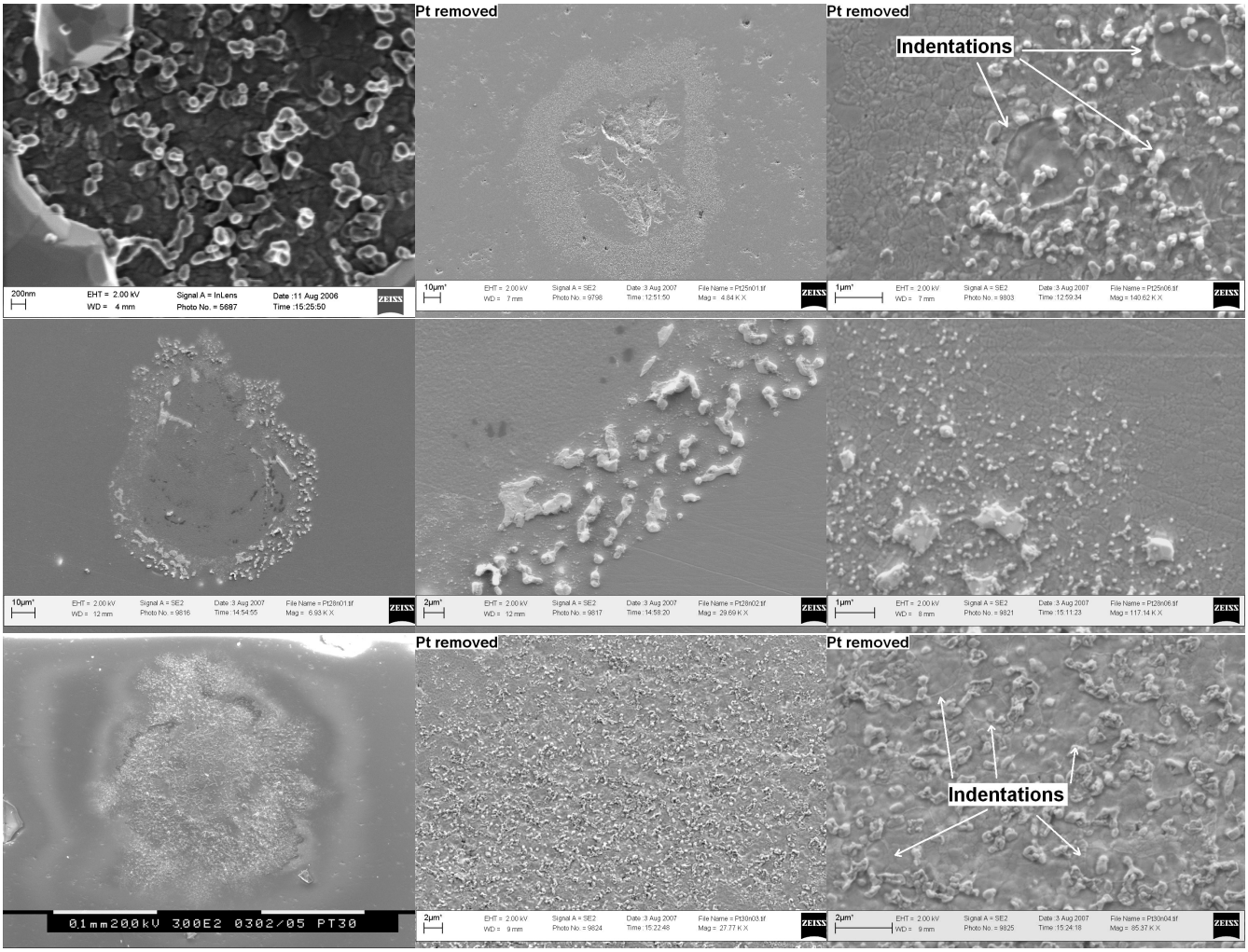


Figure 6.7: Three different electrode samples which show migration of Pt, but also the presence of impurities. Each row represents an electrode. In some of the images Pt has been removed from the sample by dissolution in $75^0C$ aqua regia.

### 6.2.4 Hotstage

#### Measurements and results

Figure 6.10 page 70 illustrates impedance spectra measurements on an array of Pt microelectrodes, immediately after the counter/reference electrode was heated to $900^0C$. The size of the 300-400nm thick Pt microelectrodes ranged from 20-250$\mu m$ in diameter. Typical images of the microelectrodes after the experiment are shown in figure 6.9 page 69. The large hole in the microelectrodes are from removal of the contacting needle. The electrodes are still dense, put the initial stage in the creation of holes and later break up into islands can be observed. For the largest electrodes $100 - 250\mu m$ the formation of pockets at the Pt/YSZ interface can be observed. Since the largest microelectrodes are most severe effected by pockets, it suggest that the formation is due to different expansion coefficients of Pt and YSZ.
Before each impedance spectrum recording the OCV was measured for 120s.

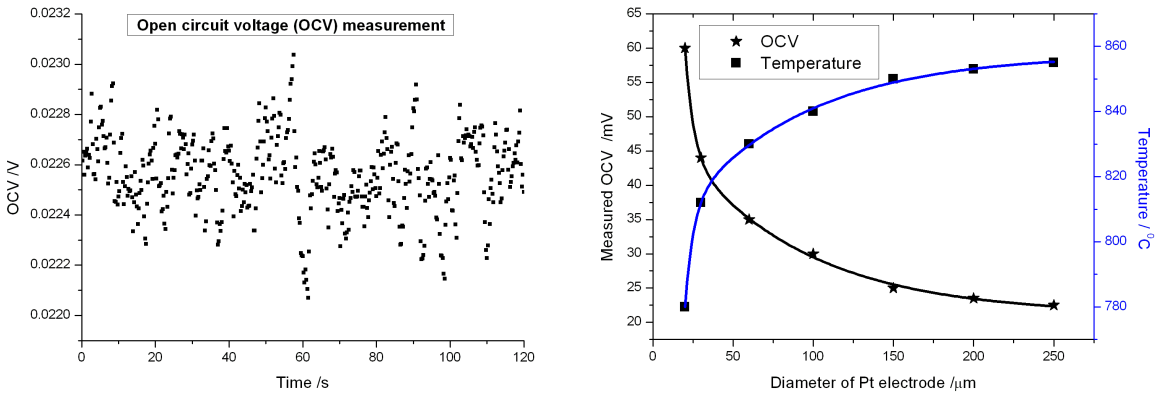


Figure 6.8: **Left:** An example of an OCV measurement before the impedance spectrum recording. **Right:** Measured OCV, with the counter/reference electrode at $900^0C$, as function of Pt microelectrode diameter. The OCV of the Pt microelectrodes are converted into temperature by using 0.5mV/K as a value for the thermoelectric power [57].

An example of such an OCV measurement is shown in figure 6.8 page 68. It is seen that the OCV was rather stable. The magnitude of the OCV reflects the temperature difference between the two sides of the YSZ slice [57]. As the Pt electrode size was decreased, the cooling effect of the contacting needle was increased and consequently the measured OCV increased. This is plotted in the right part of figure 6.8 page 68. The temperature difference

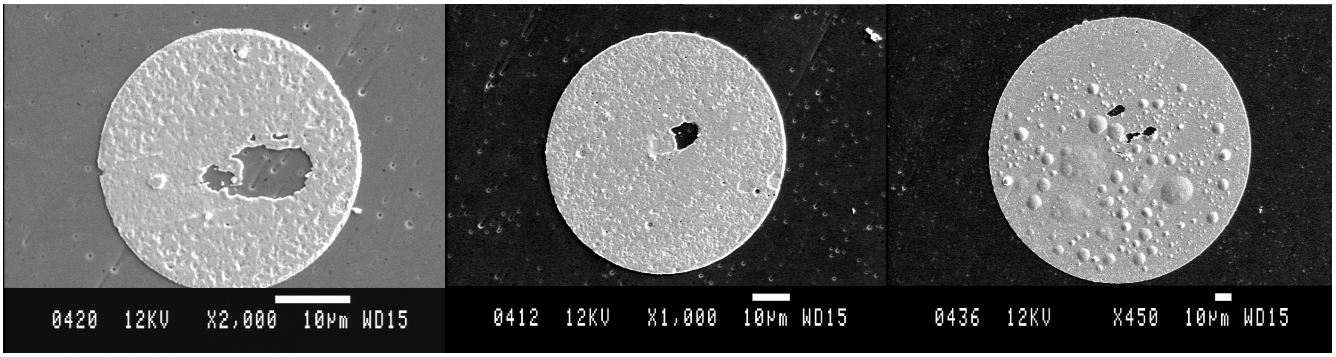


Figure 6.9: Microelectrodes after hotstage experiment. The large hole in the electrodes are from removal of the contacting needle.

across the YSZ slice for the largest microelectrodes, determined from OCV measurement, is in accordance with the calculated $\sim 50^0 C$ in appendix C page 136 and performed temperature control measurements with a two color pyrometer. The limiting factor for how small the electrodes can be and still provide reliable data, is in the present setup, the used microscope and the contacting needle. Measurements on $30\mu m$ electrodes can be done, while measurements on $20\mu m$ electrodes are difficult. Even though the precision of the contacting was to be greatly improved, it is very likely that the cooling effect of the contacting needle and the electrical noise of the setup set a limit to the electrode size on which measurements can be performed.
Inspecting the recorded impedance spectra in figure 6.10 page 70, it can be observed that, as the electrode size is decreased, the presence of two semicircles become evident. This means that two processes with different characteristic time constants are present. All the recorded spectra can satisfactory be fitted with a serial connection between an electrolyte resistance and two times a CPE, each in parallel with a resistor, $R_1(R_2Q_2)(R_3Q_3)$ in Boukamp notation [51]. Impedance measurement has been performed on a serial connection, between an $2k\Omega$ resistance and a 5nF capacitor in parallel with a $2M\Omega$ resistance, to see whether the response was an artifact. Nothing suspicious was observed. The presence of two semicircles for Pt point-electrodes have been reported [58, 59]. In the latter mentioned case, the presence of two semicircles were under anodic polarization, which lead to the conclusion that it was oxygen pockets at the Pt/YSZ interface, that gave rise to the presence of a second semicircle. Further, comparable impedance spectra with the 200 and $250\mu m$ Pt microelectrodes have been reported for elongated rectangular Pt pattern electrodes [60]. The impedance spectra were stated to consist of more than one semicircle arc, but unfortunately no fitting were performed.

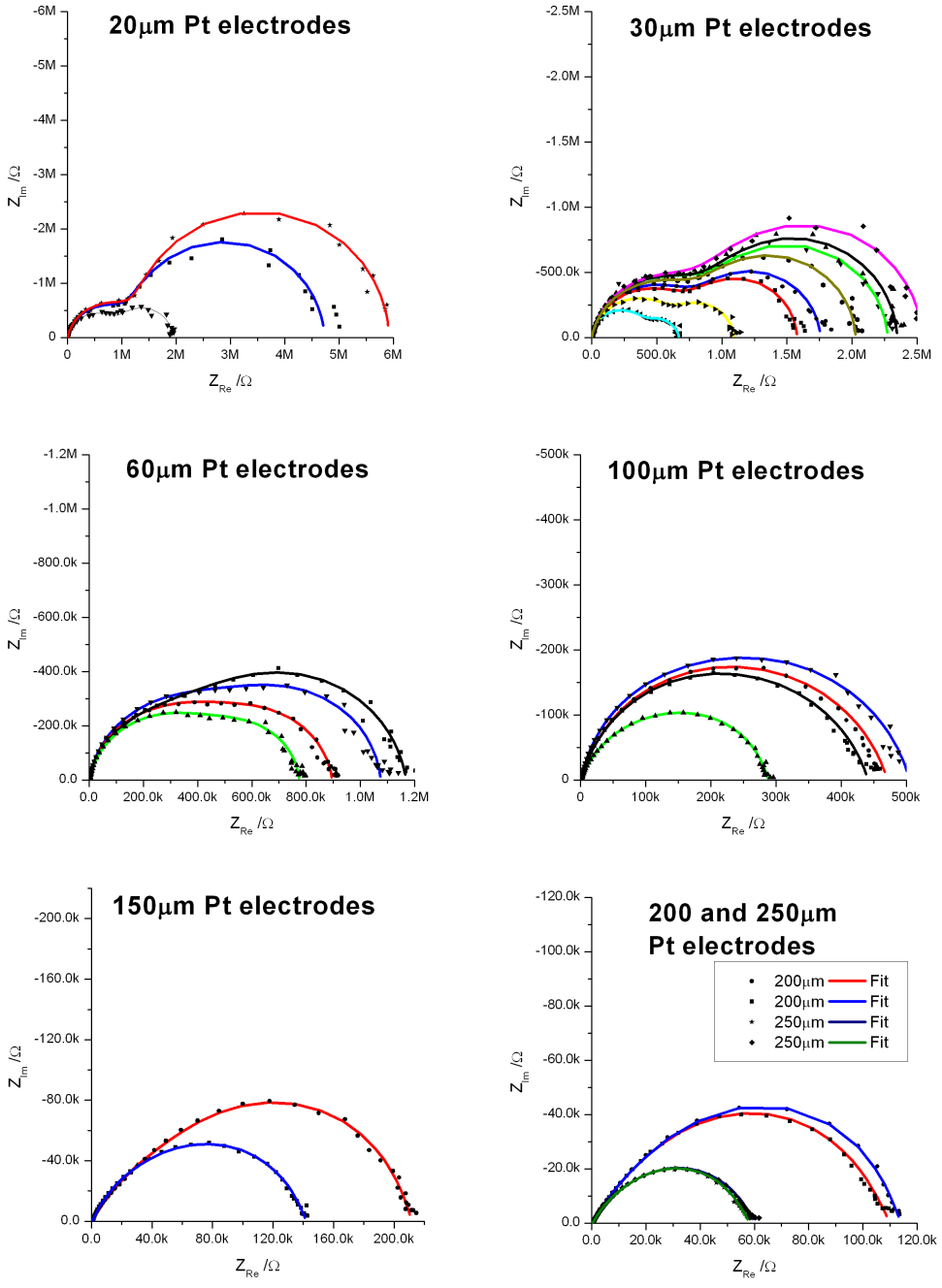


Figure 6.10: Impedance spectra of circular Pt microelectrodes at OCV with varying diameter. Each spectrum represents a microelectrode and is fitted with the equivalent curcuit $R_1(R_2Q_2)(R_3Q_3)$. The temperature of the counter/reference electrode was $900^0C$.

### Interpretation of the acquired results

During the initial fitting, one of the two CPE elements had an alpha value which was very close to 1. That CPE is in the following set as an ideal capacitor C. This change results in no, by the eye, detectable change in the quality of the fits. The change should make it easier to identify what is changing as function of electrode size, since the degree freedom in the fitting procedure is lower. The two equivalent circuits $R_1(R_2Q_2)(R_3C_3)$ (Circuit I) and $R_1(R_2Q_2(R_3C_3))$ (Circuit II), in Boukamp notation [51], are used in the following analysis of the impedance data in figure 6.10 page 70. The latter mentioned equivalent circuit is used to describe the situation with oxygen pockets at the Pt/YSZ interface. It describes three contributions in parallel, which are serially connected with an electrolyte resistance $R_1$. The $R_2Q_2$ term describes oxygen pockets at the interface, with a finite reservoir of oxygen, $R_3$ describes the electrode reaction at the TPB and $C_3$ describes the double layer capacity. The fitted parameters from the Circuit I serves as a basis for the analysis of the obtained results. The trends of the Circuit I parameters are in the end, compared with the trends of the fitted Circuit II parameters.
The physical properties, such as the reaction resistance $R_{reaction}$, the CPE $Q_2$ and the capacitance $C_3$ are expected to be proportional to a radius dependency. This can conveniently be expressed in the following way, when taking $R_{reaction}$ as an example:

$$R_{reaction} = k \cdot r^n \tag{6.1}$$

$\Downarrow$

$$Log(R_{reaction}) = n \cdot Log(r) + Log(k) \tag{6.2}$$

k is a constant, r is the radius of the electrode and n is a positive or negative exponent. Similar expressions apply to the CPE $Q_2$ and the capacitance $C_3$. Therefore, by plotting the logarithm of the different quantities as function of the logarithm of the radius, it is possible determine the radius dependency from the slope. As already mentioned some of the microelectrodes are measured at different temperatures. Assuming that the specific electrode conductivity $\sigma = 1/R_{reaction}$ has an Arrhenius temperature dependence provide:

$$R_{reaction}(T) = R_0 exp(\frac{E_a}{RT}) \tag{6.3}$$

The relation between $R_{reaction}$ at a temperature $T_1$ and $R_{reaction}$ at another temperature $T_2$, is as a consequence of equation 6.3:

$$R_{reaction}(T_2) = R_{reaction}(T_1) exp(\frac{E_a}{R}(\frac{T_1 - T_2}{T_1 T_2})) \tag{6.4}$$

The unknown parameter in equation 6.4 is, in the present case, the activation energy $E_a$. The activation energy $E_a$ for chemical reactions typically lie in range from 1eV to 2eV. This is in accordance with reported activation energies for the cathodic reaction, on Pt/YSZ, as function of oxygen partial pressure [60]. In order not to overcorrect, an activation energy of $E_a = 1eV$ was used in all situations where temperature corrections were performed. This provides values that are closer to the true values without the possibility of overcorrection. The CPE $Q_2$ and the capacitance $C_3$ are assumed, in temperature corrected data, to have no temperature dependency.
Figure 6.11 page 72 shows average values of the reaction resistance $R_{reaction}$ as function of electrode size. The reaction resistance is determined as $R_{reaction} = Z(freq. \rightarrow 0) - Z(freq. \rightarrow \infty)$. Two regions can be observed, and they become even more evident, when $R_{reaction}$ values are temperature corrected. The region with microelectrodes from $100\mu m$-$250\mu m$ in diameter has a slope very close to -2. This means that $R_{reaction}$ is inverse proportional to the area of the electrodes. The region with microelectrodes from $20\mu m$-$100\mu m$ in diameter has a less steep slope of around -1. This indicates that $R_{reaction}$ is inverse proportional to the perimeter of the electrodes. In the case where it

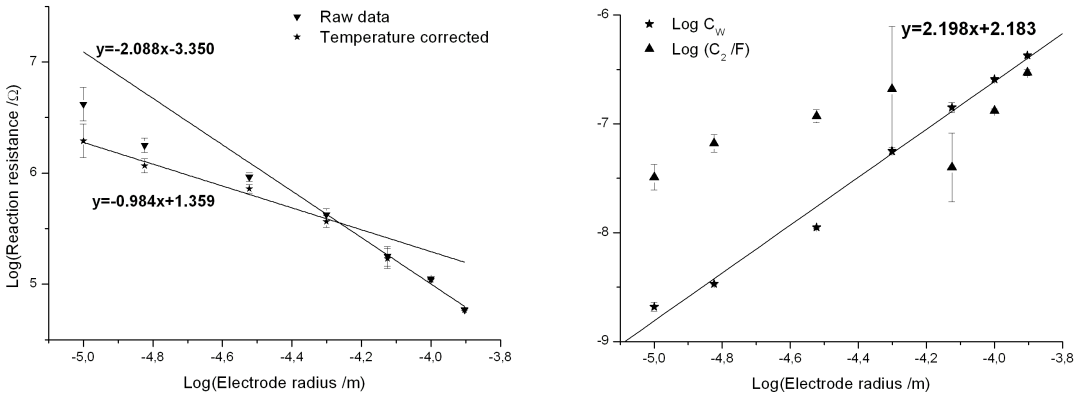


Figure 6.11: **Left:** The average reaction resistance $R_{reaction}$ values as function of electrode size. **Right:** The average CPE $Q_2$ and the capacitance $C_3$ values, determined from impedance fitting, as function of electrode size.

is possible for oxygen to diffuse through the thin film of platinum two reaction pathways are possible. The resistance from the reaction at the TPB will depend on the perimeter (Pathway I), while the resistance from diffusion of oxygen through the bulk of the film will depend on the area (Pathway II). Due to the different dependencies on the radius r of the pathways, the two

contributions (Pathway I and II) to the total reaction resistance $R_{reaction}$ is dominant at different r values. For $r \rightarrow \infty$ the $R_{reaction}$ is inverse proportional to the area, while for $r \rightarrow 0$ the $R_{reaction}$ is inverse proportional to the perimeter. This means that a shift between the two pathways I and II will be observable when scanning $R_{reaction}$ as function of r. This is exactly what is observed in the left representation of figure 6.11 page 72. However, the author of the present thesis, is not aware of any reported indications in the literature that oxygen diffusion through platinum is of any significance. Bulk oxygen diffusion through silver has, though, been reported by M. Kleitz et al [61]. They observed two semicircles as in the present case. If any significant oxygen is able to be dissolved in Pt, this would provide an explanation for the abnormal high capacitance of Pt electrodes as discussed in section 2.1.1 page 13. It would also confirm the postulation made by M. Kleitz, that a reservoir of electroactive neutral oxygen exist for cathode reactions [5]. The 300-400nm thick Pt microelectrodes are intact after a few hours of experiments at $800 - 850^0C$, as shown in figure 6.9 page 69. This leaves bulk oxygen transport as the only apparent explanation that can account for the $r^{-2}$ dependency of $R_{reaction}$ and would at the same time explain the presence of two semicircles. If oxygen is dissolved in the Pt bulk it should, though, be possible to provoke an impedance warburg diffusion response.
The clearly observed pockets at the Pt/YSZ interface for the largest electrodes $100 - 250\mu m$ can also explain the presence of two semicircles.
From the CPE $Q_2$ a capacitance $C_W$ can be calculated according to [69] as:

$$C_W = (R^{1-\alpha}Q)^{1/\alpha} \tag{6.5}$$

The right part of figure 6.11 page 72 shows $C_W$ along with $C_3$ as function of electrode size. A slope of 2 is observed for $C_W$. This means that $C_W$ is proportional to the area of the electrode. $C_3$, on the other hand, has a sudden abrupt change in magnitude from the $150\mu m$ to the $100\mu m$ in diameter electrodes. Both a bulk reservoir of oxygen and a double layer capacitance are expected to be proportional to the electrode area. More correct, the bulk reservoir of oxygen capacitance is expected to depend on the volume, but the height of the microelectrodes are constant. However, the double layer capacitance is not expected to have a significant temperature dependence, while a capacitance in the form of dissolved oxygen in the Pt bulk is. The normal trend for solubility is a decrease with increasing temperature. When measurements are made on smaller and smaller electrode sizes, it is not only the size that is changed, but unfortunately also the temperature of the electrodes, as shown in the right part of figure 6.8 page 68. This might explain the abrupt change in $C_3$. $C_3$ is smaller than $C_W$ for the three largest microelectrodes, and larger than $C_W$ for the remaining electrode sizes. This

can also be explained with the decrease in temperature as electrode size decreases.
In the case of no bulk transport of oxygen the following relations are valid:

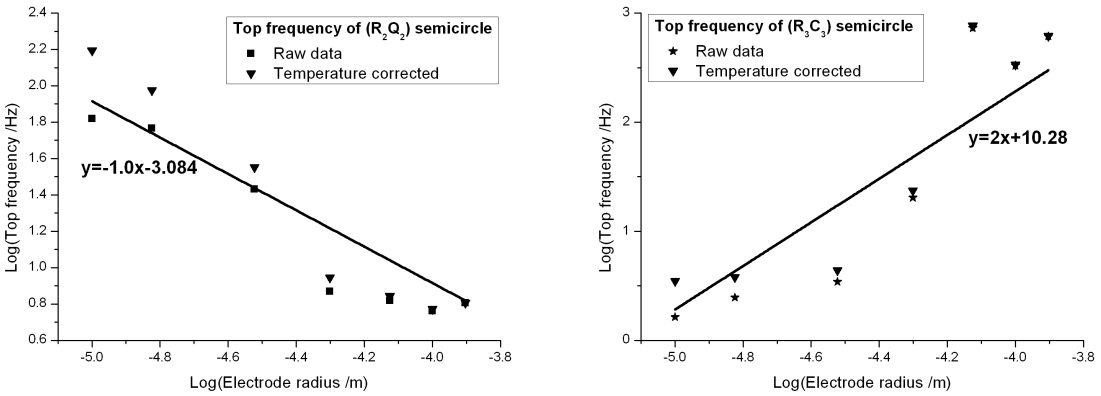


Figure 6.12: **Left:** The top frequency of the $R_2Q_2$ semicircle as function of electrode size. **Right:** The top frequency of the $R_3C_3$ as function of electrode size. The average parameter values, acquired from fitting the impedance spectra with the equivalent circuit $R_1(R_2Q_2)(R_3Q_3)$, were used in the calculation of the top frequencies.

$$R_{reaction} \propto \frac{1}{r}, \qquad C \propto r^2 \tag{6.6}$$

For the top frequency $\nu_{top}$ of an ideal semicircle this implies:

$$\nu_{top} = \frac{1}{2\pi RC} \propto \frac{1}{r} \tag{6.7}$$

If bulk transport of oxygen is dominating $R_{reaction} \propto \frac{1}{r^2}$, then $\nu_{top}$ would be constant as function of the electrode radius. The top frequencies of the two $R_2Q_2$ and $R_3C_3$ semicircles, in the fit with the equivalent circuit $R_1(R_2Q_2)(R_3C_3)$, are plotted as function of electrode size in figure 6.12 page 74. The top frequency $\nu_{top}$, of the $R_2Q_2$ semicircle, is for the four largest microelectrodes almost constant , while $\nu_{top}$, for the remaining microelectrodes, has a radius dependency close to $r^{-1}$. The top frequency increases with decreasing electrode size. This is opposite for the $R_3C_3$ semicircle, where $\nu_{top}$ decreases with decreasing electrode size. The dependency on the radius is in the neighborhood of $r^2$.

Comparing the presented fitted parameters of Circuit I with the fitted parameters of Circuit II provides the same general trends. $R_{reaction}$ is of course independent of the chosen equivalent circuit. The same area dependency of $C_W$ is observed and an abrupt change in $C_3$ from the $150\mu m$ to $100\mu m$ microelectrode is observed. However, $C_3$ is constant for microelectrodes smaller and larger than abrupt change from the $150\mu m$ to the $100\mu m$ microelectrode. The trend of the top frequencies do not show any new clear dependence on the radius. Since $C_3$ depends on the chosen equivalent circuit the interpretation of it is unclear. The data from fitting with the Circuit I and II equivalent circuits can be found in appendix B page 133. Further analysis of the impedance spectra are necessary in order to elucidate the complete physical meaning of the impedance spectra in figure 6.10 page 70. This is unfortunately not possible in the present thesis due to lack of time.

# Chapter 7

# Noble metal microelectrodes

## 7.1 Article

## Three-phase-boundary dynamics at metal/YSZ microelectrodes

J. Nielsen, T. Jacobsen

Accepted for publication in:

**Solid State Ionics**

**Three-Phase-Boundary dynamics at metal/YSZ microelectrodes**

J. Nielsen, T. Jacobsen

Department of Chemistry, Technical University of Denmark, DK-2800, Denmark

**Abstract**

Studies on microelectrodes prepared by electrochemical etching show that noble metals catalytically active towards oxygen reduction like Pt, Pd and Ag are not as inert at high temperature as commonly assumed. The results show that the morphology of the electrode and the reaction zone changes during polarization. Electrode material migrates from the electrode surface and deposits on the YSZ surface forming dendritic structures. Au electrodes, which are catalytically poor towards oxygen reduction, seem in comparison to be inert. The transport mechanism for the electrode material migration is studied by comparing the electrochemical responses and physical properties of the different noble metal electrodes. Also heat treatment of migrated electrode material experiments and polarization of geometric well defined dense thin ½-1μm layered Lanthanum-Strontium-Manganite (LSM) and Pt films on YSZ experiments, were conducted in order to distinguish between a surface and gas phase transport mechanism.

**Keywords:** SOFC, Microelectrodes, Three-Phase-Boundary (TPB), Cathode, Surface migration.

**Corresponding author:** Email address: jim@kemi.dtu.dk; Tel.: +45 45252438

## 1. Introduction

Electrode overvoltage and especially the cathode overvoltage in solid oxide fuel cells (SOFC) is the main contributor to performance decrease. Without further understanding of the dynamics at the electrode/electrolyte and the electrochemistry, the overvoltage can be reduced by optimization of the reaction zone. For the cathode this implies increasing the Three-Phase-Boundary (TPB) length or introduction of materials with mixed ionic and electronic conduction, but after all this is not without problems and limits. Therefore, further insight and knowledge about reaction mechanisms and reaction pathways as well as changes of the reaction zone associated with operation is desirable. In order to exclude interference from chemical reactions between electrode and electrolyte, noble metal point electrodes have often been applied as model systems in more fundamental studies, and more recently geometrically well defined pattern electrodes have also been employed. As shown for Pt/YSZ electrodes, the TPB reaction zone is by no means a constant parameter due to migration of Pt when polarized at $1000^0$C [1]. The Pt migration can cause undesirable effects, e.g. when Pt is used as current collector in SOFC research [2], but it also may be crucial for the interpretation of work reported in the literature on high temperature systems involving Pt and especially Pt/YSZ. The characteristic current fluctuations as a consequence of Pt electrode material migration have been shown, in temperature sweeps, to exhibit a strong temperature dependency [10]. It was found that below $950^0$C the current fluctuations are to close to non-existing. A natural question that arises is whether Pt is exceptional with respect

to electrode material migration or if it is a common occurring phenomenon for high temperature cathode/YSZ systems. The purpose of the present study is to clarify how general electrode migration is and in doing so provide further clues concerning the transport mechanism. For comparison with Pt results and increase the possibility for detecting any electrode material migration with respect to other noble metals, experiments are conducted at $1000^0$C and in the case of Ag at $920^0$C.

**2. Experimental**

Pd and Ag microelectrodes were prepared by electrochemical etching of wires. This was done by applying a 50Hz AC voltage with 35V ±5V amplitude to the wire in an aqueous solution containing 40vol% of a saturated calcium chloride solution at room temperature [3]. After electrochemical etching the electrodes were cleaned in an ultrasonic bath with water and ethanol. Ball shaped gold point electrodes were prepared by melting a drop at the end of a gold wire in a gas flame. The electrodes were mounted in a thin alumina tube inside another alumina tube (1mm Ø) positioned a few millimetres above a polished (3µm diamond paste) 8% Yttria Stabilized Zirconia (YSZ) tablet, and the whole assembly was placed inside a tubular furnace and heated. At $1000^0$C the electrodes were gently lowered and allowed to touch the electrolyte (YSZ). The weight on the electrodes was in between 2.5-6g. The electrolyte tablets were equipped with a large porous Pt painted counter electrode, the potential of which

is very close to the reversible oxygen electrode potential. This is also used as reference electrode. Thus, all potentials reported in this work are relative to the oxygen electrode potential in air. No attempts to correct for IR drops were made. During measurements, air saturated with water at room temperature was passed through the furnace. The electrodes were allowed to creep until a stationary state had been reached before the electrochemical experiments were initiated. The characteristic time for reaching a stationary contact area was estimated by monitoring the electrolyte resistance with impedance spectroscopy.

50Hz noise from the heating coils of the furnace was reduced as described in [4]. Step polarization, cyclic voltammetry and data requisition was done using a Gamry FAS2 Femtostat potentiostat.

**3. Considerations regarding the selection of metal electrodes**

Pd is chosen for the following reasons: catalytically similar to Pt, oxides of Pd are as the oxides of Pt not thermodynamic stable at $1000^0$C in air and as can be seen in Fig. 1 the partial pressure of PdO(g) is almost a factor 10000 lower than the partial pressure of $PtO_2$(g) at $1000^0$C. Electrode material transport of Pd through the gas phase with reduction of PdO(g) at TPB is therefore expected to be negligible compared with Pt electrodes.

Ag is similar to Pt with respect to being a good cathode in SOFC. The partial pressure of AgO is comparable to that of $Pt/PtO_2$ and it is also widely utilized in SOFC research as counter electrode and current collector. The high

activity of Ag towards oxygen reduction is partly a result of oxygen dissolution in the Ag bulk that enables mixed conductivity and hence extends the reaction zone [6].

Au is in contrast to Pt, Pd and Ag a poor cathode material in SOFC and as Fig. 1 shows the partial pressure of AuO is very low compared to $PtO_2$, AgO and even PdO.

Therefore, comparison of physical properties of the mentioned metal electrodes and the respective electrochemistry should give further knowledge about electrode material migration and the SOFC cathode electrochemistry at high temperature on YSZ.

## 4. Results

### 4.1 Palladium microelectrodes

As is shown in Fig. 2 step polarization of fresh Pd electrodes results in a very rapid strong activation of the electrodes that takes place on the timescale of seconds. The current increases a factor of around 40 and fluctuates dramatically in a saw-tooth like manner with amplitude 30-50 percent of the total current during the first 1½ hour after which the fluctuations dies out. Further Fig. 2 shows that the fluctuations can be revived by step wise increase of the cathodic polarization, in the present case from -150mV to -300mV. The experiment was terminated by the program due to a setting of max current to 1mA. Fast linear

potential sweeps of a fresh Pd microelectrode can be seen in Fig 3. Inductive hysteresis in the cathodic polarized region is seen for all fast sweeps even for sweep rates as high as 1V/s. In the 100mV/s sweep the onset of current fluctuations can be observed and at a sweep rate of 10mV/s the fluctuations become very pronounced. At very low sweep rates of 5μV/s the inductive loop is almost closed with no sign of regular characteristic current fluctuations indicating that the electrode is at a steady state during the sweep.

SEM images of the contact area afterwards can be seen in Fig. 4 showing a belt around the contact area of migrated Pd. The belt consists of 10-100 nanometer sized apparently non crystalline spherical Pd particles.

### 4.2 Silver microelectrodes

Fig. 5 shows linear potential sweeps of a fresh Ag microelectrode at $920^0$C. At the highest sweep rate (100mV/s) the sweep is very close to being reversible. As the sweep rate is decreased from 100mV/s an increasing opening of an inductive loop in the cathodic region is observed. Fig. 6 shows step polarization of the electrode performed after the sweeps shown in Fig. 5 and results in an activation of the electrode on the timescale of hours. The activation is smooth with only a few minor abrupt changes in current. The current is increased 50 percent during 12 hours.

Inspection of the contact area by SEM afterwards gives images like Fig. 7. The images show Ag outgrowth of fingers, with dendritic shape, from the electrode contact area. EDS confirms without any doubt that the outgrowth is Ag. The images strongly indicate that the outgrowth is driven by the electric field. The lack of outgrowth from the hollow part of the otherwise circular interface seen on the left in Fig. 7 shows, that the electric field is the driving force.

### 4.3 Gold electrodes

Step and linear potential sweeps similar to those for Pd and Ag electrodes were conducted on Au electrodes. The contact area was of the same order of magnitude as the Ag electrode shown in Fig. 7. Small currents (<1μA), no significant activation and no inductive loop in the cathodic region of the linear potential sweeps was observed. Inspection of the electrode contact areas afterwards showed no sign of migration of electrode material.

### 4.4 Temperature treatment of migrated electrode material

Since air flow in the furnace also plays an important role besides the partial pressures given in Fig.1 contact areas with migrated Pt and Pd were heat treated at $1000^0$C and Ag at $920^0$C for 105 hours. The upper left of Fig. 8 shows the Pt contact area before temperature treatment. It was not possible to locate

the contact area afterwards leading to the conclusion that all migrated Pt had evaporated.

In the upper right of Fig. 8 is shown an image of the Ag electrode in Fig. 7 after heat treatment. The outgrown tree like structures had almost disappeared and the inner half circular extensive Ag rim has been considerable reduced.

The lower left of Fig. 8 shows an image after temperature treatment of the Pd contact area in Fig. 4. The image shows that only a small part of the Pd has evaporated and that the small Pd particles have come together and grown into larger crystals. The lower right of Fig. 8 is a zoom in on the left image showing that a lot and maybe all of the Pd has become crystalline.

**4.5 Polarization of dense layered LSM/Pt films**

A ½-1μm thick circular dense film of $(La_{0.85}Sr_{0.15})_{0.95}MnO_{3+\delta}$ (LSM) on a polished 8% YSZ was prepared by Pulse Laser Deposition (PLD) using a 1mm thick cobber mask with holes of 2mm in diameter. A similar shaped and sized, slightly shifted 0.2-0.5μm thick dense Pt film was deposited on top of the LSM film. The films were electronically contacted by placing a gold point electrode down on the Pt layer. The whole assembly was heated to $1000^0$C with a heating rate of $100^0$C/hour and immediately polarized at -140mV. The furnace was turned off after 7 hours, but with the polarization kept on during cooling. Fig. 9 shows the polarized Layered films together with a reference set of layered films on the same YSZ tablet that has not been subjected to polarization, but otherwise with

the exact same history. Comparison of the two set of films shows that the one, which had been subjected to polarization, shows Pt migration. Pt migration is as expected observed along the Pt/YSZ perimeter, but a thorough inspection of the LSM/YSZ perimeter also shows the presence of droplets of migrated Pt. Pt is identified with EDS by the high energy peaks at 9.437eV, 11.074eV and 11.263eV. Beside this, similar polarization experiments with pure LSM films show no sign of droplet formation along the perimeter. The experiment has been conducted several times to check for reproducibility. It is therefore concluded that the observed droplets along the LSM/YSZ perimeter consist of Pt.

**5. Discussion**

The observed migration phenomena can conveniently be described in terms of an activation and deactivation process. The activation process involves an electric field driven electrode material migration process involving either a gas phase transport mechanism with metal oxides being reduced at the TPB or some kind of a surface transport mechanism. The known ingredients in the deactivation process are migrated metal evaporation and surface tension forces. The significance of eventual electrolyte surface changes is unknown, but probably very important in case of an electrode material surface transport activation mechanism.

Comparing the activation/deactivation process of the different electrodes shows that Pd has both the fastest activation and deactivation with characteristic

time constants of seconds while Pt and Ag seem to have comparable activation rates with characteristic time constants of hours, but certainly significantly different deactivation rates. The lack of a regular current fluctuation pattern for Ag electrodes means that the Ag deactivation does not take place, while Pt deactivation happens abruptly on the time scale of seconds. The very low rate of the Ag deactivation process probably reveals how the Pt and Pd electrode material migration would look like if no interference from the deactivation occurred. The deactivation results in a cut off of the outgrown fingers with tree like look thereby disturbing the potential distribution. This disruption causes a new potential distribution which results in a change in the outgrowth of electrode material that can lead to structures as the Pt structure shown in [1]. In the Pd case the fast deactivation mechanism results in an immediate breakup leaving an ocean of small Pd particles as shown in Fig. 4.

A somewhat puzzling phenomenon is the difference in current fluctuation pattern between Pt and Pd. In the case of Pt an abrupt decrease of the current followed by a slow increase is observed. This was interpreted as a cut off of electronically connected Pt followed by an outgrowth/regain of Pt with electronic contact to the electrode. This interpretation is in accordance with impedance spectroscopy data. For the Pd case the opposite is observed. Here a slow current decrease is seen followed by an abrupt increase. This behavior seems at first sight to be in conflict with the Pt current fluctuation hypothesis, but it is not totally clear for the Pd case at what situations the TPB length has an optimum, what influence surface forces has and whether these are affected by polarization.

It is unfortunately not possible to monitor the Pd migration with impedance spectroscopy since Pd changes are faster than impedance recording.

It is well established that chromium from interconnect materials can form volatile oxidized chromium species that can be transported through the gas phase to the cathode TPB where they are reduced and causes a poisoning [7,8,9]. It is therefore very tempting to conclude that something similar, but with electrode metal oxides, is taking place in the present study. As already mentioned it is difficult to judge whether a gas phase transport mechanism is likely to occur based on the partial pressures given in Fig. 1 since air flow in furnace etc. also is of importance. The results of subsequent temperature treatment of the contact areas with migrated electrode material shown in Fig. 8 and presented in section 4.4 shows that evaporation of Pt and Ag occur on the same timescale as the electrode activation. This is not the case for Pd where all the migrated Pd shown in Fig. 4 is transported within 3 hours but with the majority of Pd still remaining after 105 hours at $1000^0$C. Instead of Pd evaporation a growth of considerable larger crystalline structures has taken place pointing towards some kind of Pd surface transport. The partial pressures reported in Fig. 1 are generally in agreement with temperature treatment experiments. The Pt migration distance, from the source Pt film to the perimeter of the LSM film, in the experiments presented in section 4.5 is very convincing evidence of a gas phase transport mechanism for the migration of Pt. Since Ag is very alike Pt in all comparisons, except the apparent lack of deactivation, it suggests that Ag migration also proceeds through the gas phase. The partial

pressure of gold oxide is very low as can be seen in Fig. 1 and the poor catalytic activity of Au towards oxygen reduction results in a very low current density. This means that neither an electrode material migration mechanism through the gas phase nor an electro migration mechanism is expected. This is in accordance with observations.

The possibility of different electrode material migration mechanisms can in principle not be excluded. Pd migration can only be explained by a surface transport mechanism based on the rapid activation with dramatically current fluctuations that can be revived by increasing the cathodic polarization further stepwise. Also the temperature treatment experiment shows no significant Pd evaporation. These arguments points to the conclusion that Pd migration takes place by an unknown surface transport mechanism, while Pt and Ag migration take place by reduction of gaseous metal oxides at the cathodic potential drop across the TPB.

**6. Conclusion**

It was shown that Pt electrode migration upon polarization and the corresponding activation is not a unique feature for Pt, since Ag and Pd shows similar behavior. Temperature treatment experiments of migrated electrode material at the same temperature and timescale, at which the transport of electrode material takes place, revealed in the case of Ag and Pt that evaporation is fast enough to suggest, that the observed electrode Ag and Pt material migration and hence the resulting activation is caused by reduction of gaseous metal oxides at the TPB.

This interpretation and the lack of Au electrode migration and Pd evaporation are in accordance with the partial pressures of the metal oxides. The Pt gas phase transport mechanism is further supported by cathodic polarization of geometrically well defined electrodes of layered dense LSM/Pt films. However, the gas phase transport mechanism cannot explain the observed Pd electrode behavior. The behavior of Pd electrodes seems to be distinctly different from the behavior of Pt and Ag electrodes. Only a surface transport mechanism seems to be ably to explain the behavior of Pd electrodes.

**Acknowledgement:**

This work is part of the research project “Efficient conversion of renewable energy by solid oxide cells” financed by The Danish Ministry of Science Technology and Innovation. Discussions and cooperation with colleagues at Risø National Lab are greatly appreciated. In particularly the authors thank Nini Pryds and Katarzyna Rodrigo for the PLD preparation of thin layered LSM and Pt films and Ming Chen for help regarding Factsage and Thermo-Calc.

**References:**

[1] J. Nielsen, T. Jacobsen, Solid State Ionics, **178**, 1001-1009, (2007).

[2] S. P. Simmer, M. D. Anderson, L. R. Pederson, J. W. Stevenson, J. Electrochem. Soc., **152(9)**, A1851-A1859, (2005).

[3] A. J. Nam, A. Teren, T. A. Lusby, A. J. Melmed; J. Vac. Sci. Technol., **B 13(4)**, 1556-1559, (1995).

[4] L. Bay, T. Jacobsen; Solid State Ionics, **93**, 201, (1997).

[5] K. Hesselmann, O. Kubaschewski, O. Knacke; Thermochemical properties of inorganic substances, 2. edition, Springer (1991).

[6] R. Jimenez, T. Kloidt, M. Kleitz, J. Electrochem. Soc., **144**, 582, (1997).

[7] S. P. S. Badwal, R. Deller, K. Foger, Y. Ramprakash and J. P. Zhang; Solid State Ionics, **99**, 297-310, (1997).

[8] Y. Matsuzaki and I. Yasuda; Solid State Ionics, **132**, 271-278, (2000).

[9] K. Hilpert, D. Das, M. Miller, D. H. Peck and R. Weib; J. Electrochem. Soc. **143**, 3642-3647, (1996).

[10] T. Jacobsen, K. V. Hansen, E. Skou, J. Electrochem. Soc. , 152(11), A2203-A2206, (2005).

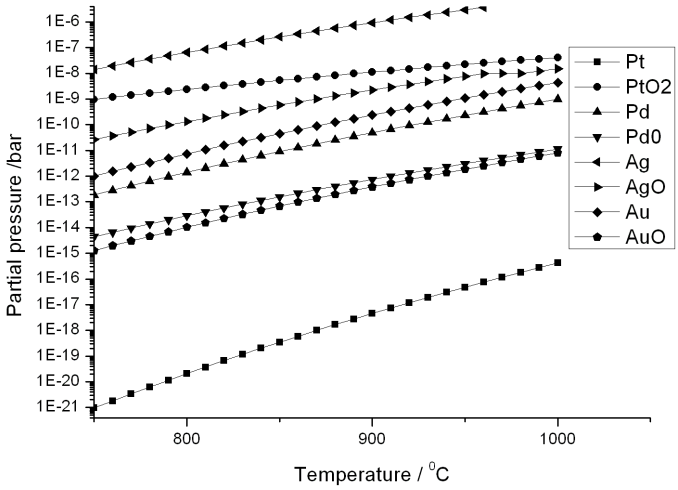


Figure 1: Partial pressure of selected metals and the oxides as function of temperature. The partial pressures are calculated using thermodynamic data from Factsage database, Thermo-Calc database and [5].

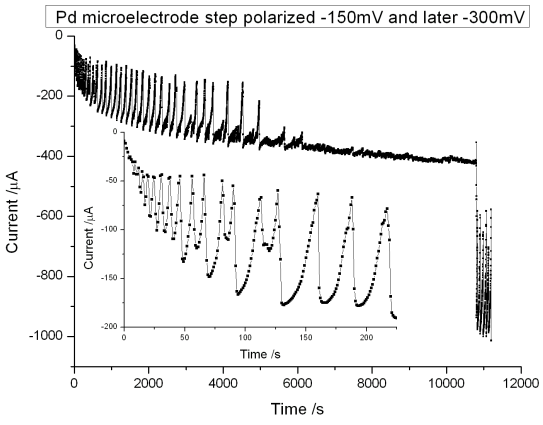


Figure 2: Fresh Pd microelectrode step polarized -150mV and later -300mV.

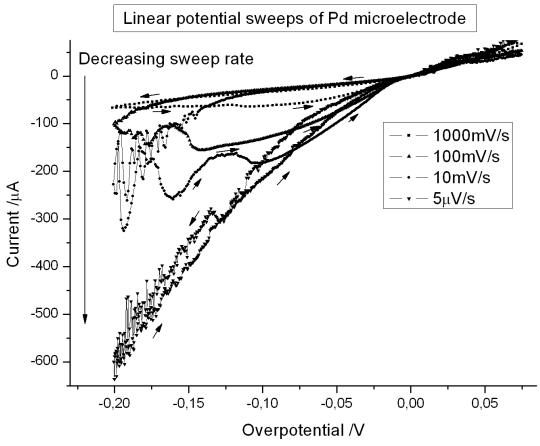


Figure 3: Linear potential sweeps of fresh Pd microelectrode.

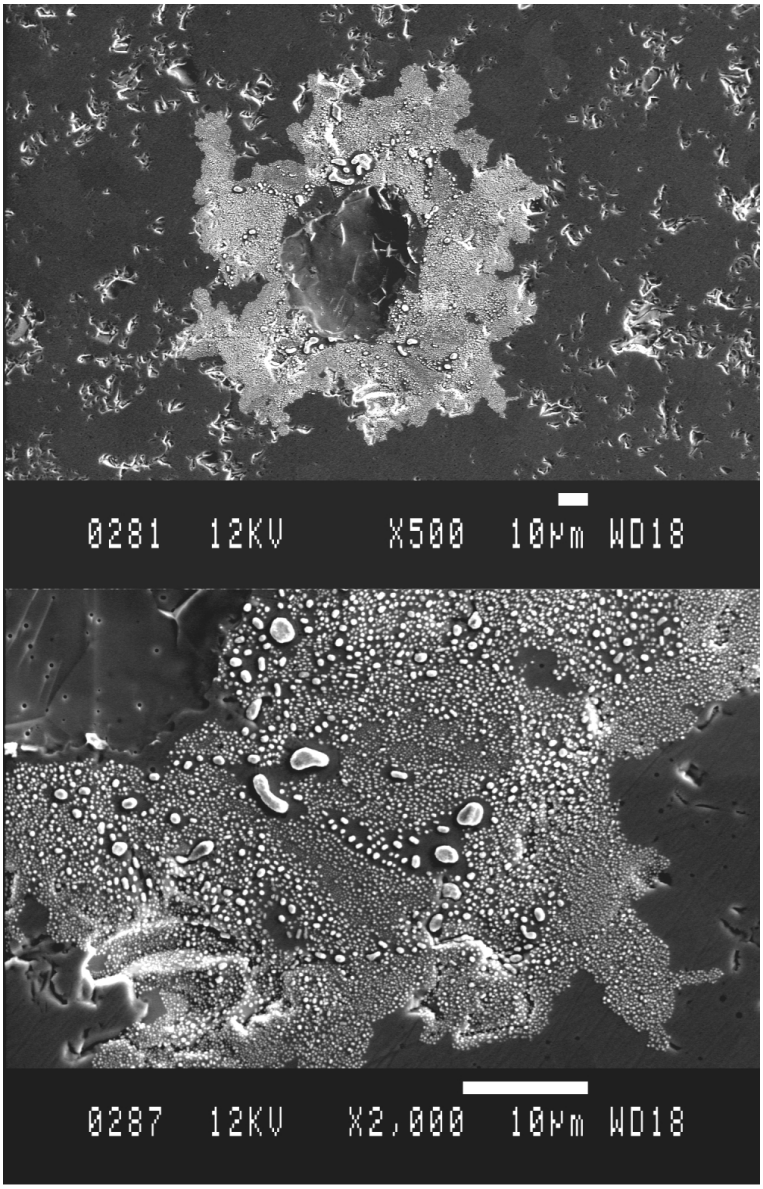


Figure 4: Images of contact area of step polarized Pd electrode after the experiment in Fig. 2 was performed. The large central crater is from rip off of the electrode.

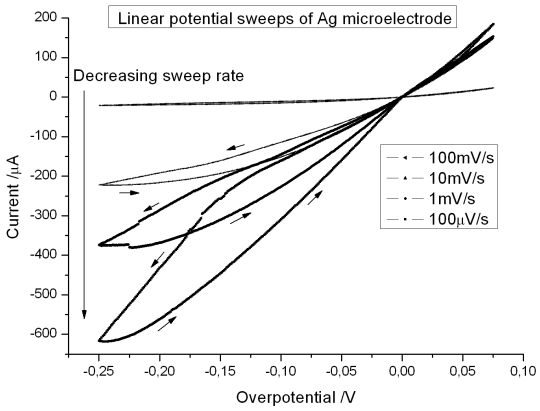


Figure 5: Linear potential sweeps of fresh Ag microelectrode.

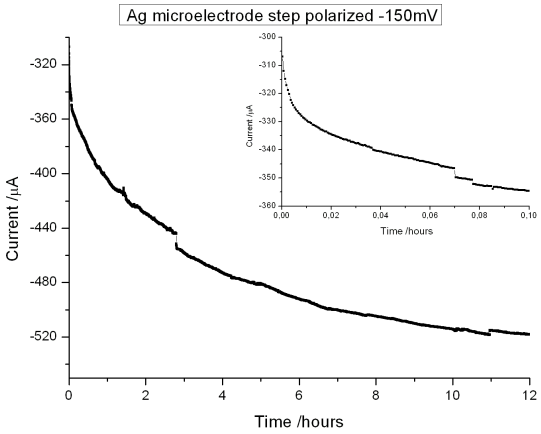


Figure 6: Step polarization of Ag microelectrode after the sweeps in Fig. 5.

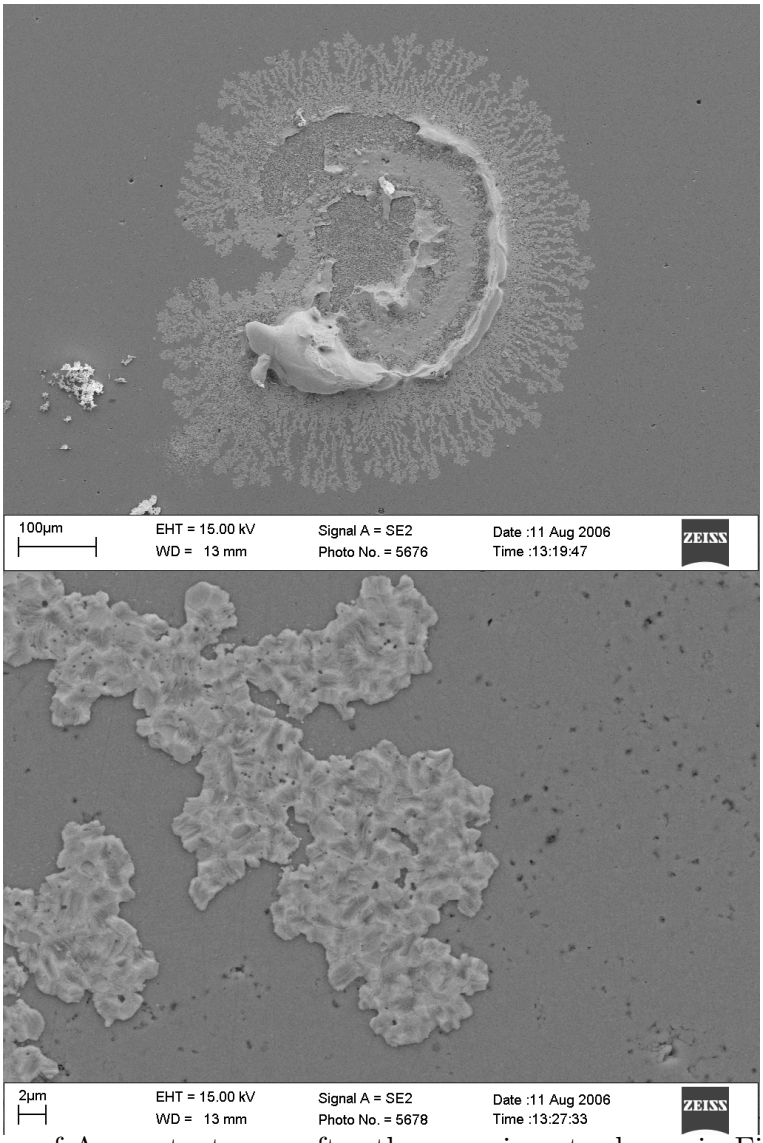


Figure 7: Images of Ag contact area after the experiments shown in Fig. 5 and 6. The breakage in the middle of the top image is from rip off of the electrode.

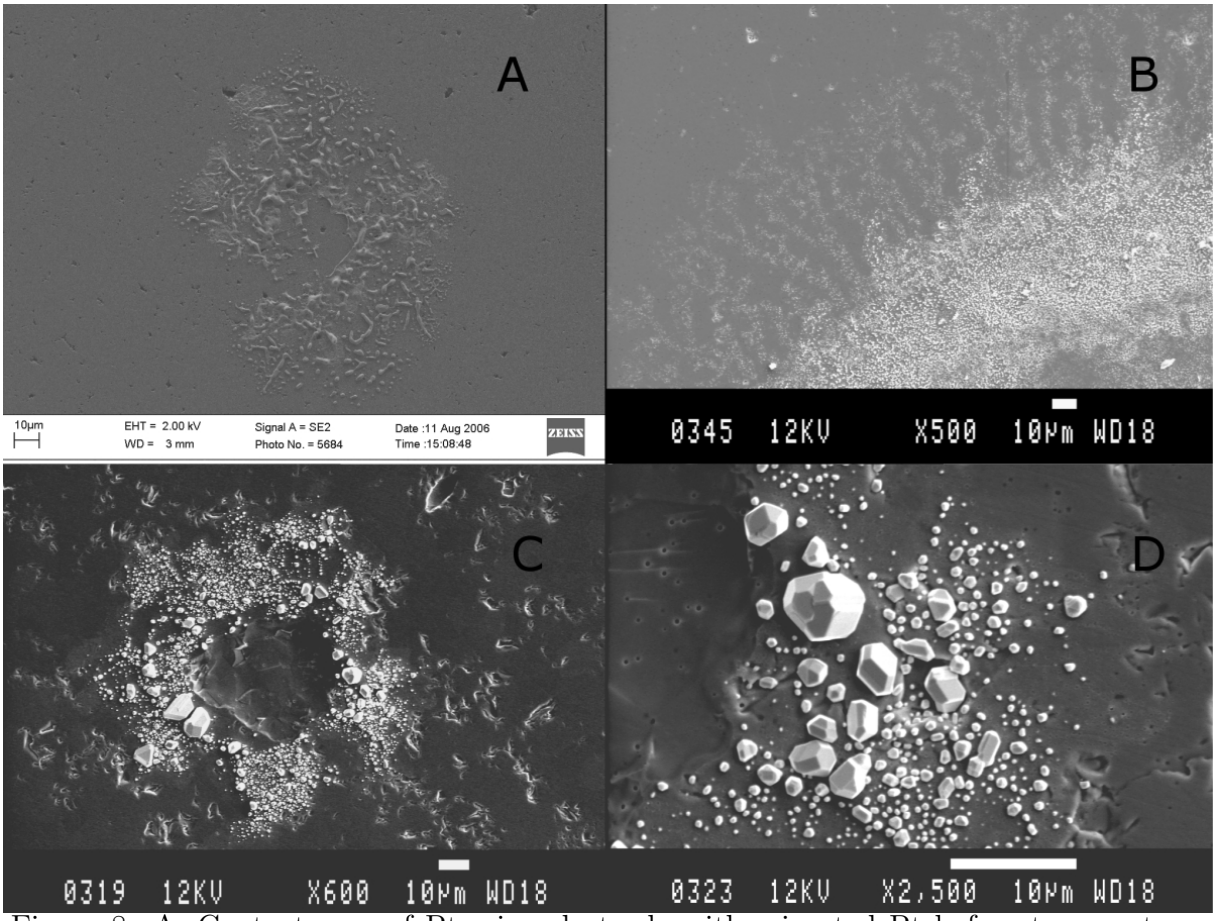


Figure 8: A: Contact area of Pt microelectrode with migrated Pt before temperature treatment at $1000^0C$ in 105hours. B: Ag contact area shown in Fig. 7 after temperature treatment at $1000^0C$ in 105hours. C: Pd contact area shown in Fig. 4 after temperature treatment at $1000^0C$ in 105hours. D: Zoom in on the image in C.

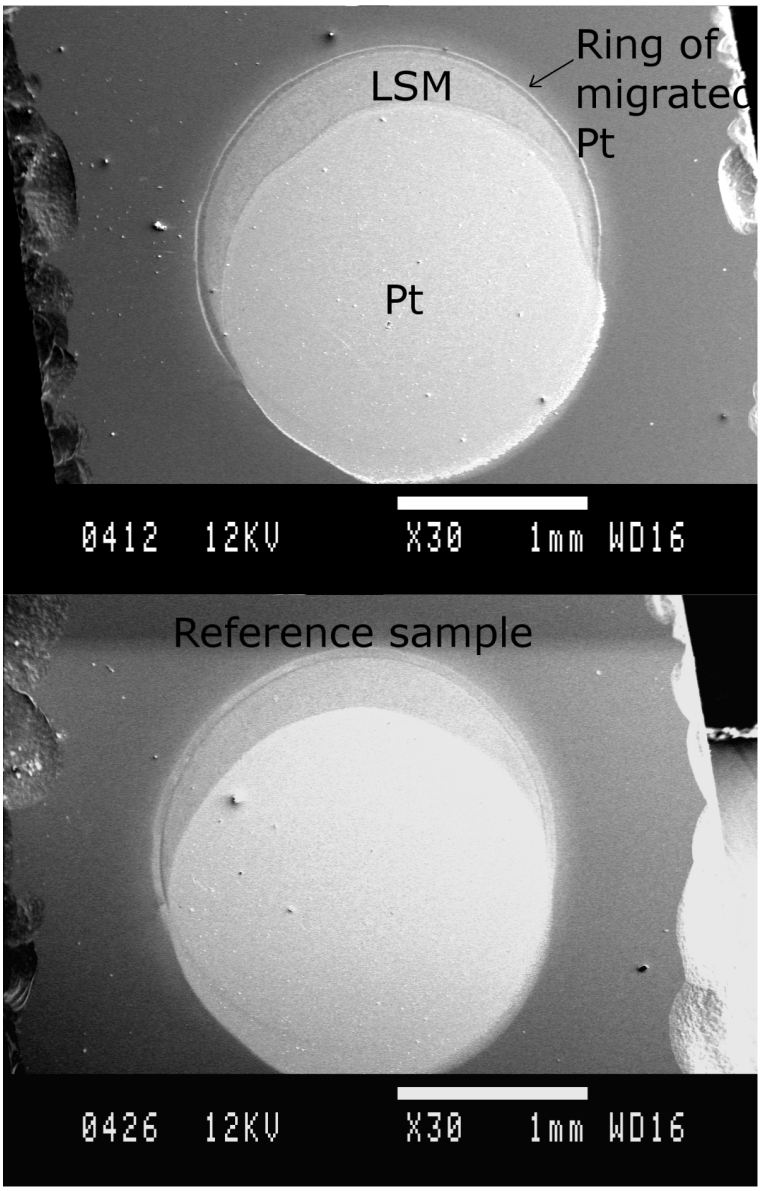


Figure 9: Upper image: 7 hour polarized overlapping LSM and Pt films at $1000^0C$. Lower image: Reference set of films not subjected to polarization.

## 7.2 Additional results with noble metals

### 7.2.1 Pd microelectrodes

Figure 7.1 page 97 illustrates the reproducibility of the rapid activation which is followed by pronounced current fluctuations of Pd microelectrodes upon cathodic step polarization from OCV. The current fluctuations are damped and die out within approximately 1-2 hours, and a final slow deactivation with time is observed. These general trends are similar to what is observed for Pt microelectrodes and is most clearly illustrated by the current progression of the -250mV step polarized Pt microelectrode page 53. Figure 7.2

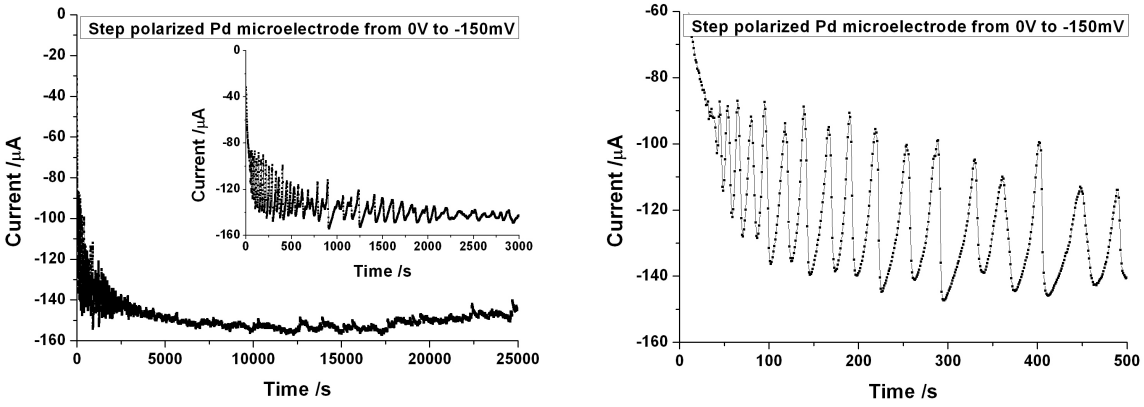


Figure 7.1: Current progression of a typical Pd microelectrode that has been step polarized from OCV.

page 98 shows selected images of polarized Pd microelectrodes. The upper left image is the contact area of a Pd microelectrode on YSZ, which has been subjected to a series of systematic linear potential sweeps, showing a finger like dendritic outgrowth of Pd from the perimeter of the Pd electrode/YSZ contact area. This supports the idea that if no deactivation of the electrode material outgrowth were to occur, outgrown fingers of electrode material from the electrode/YSZ contact area would be seen, like in the case of Ag microelectrodes page 94. The upper right image is a typical image of migrated Pd. As in the case of migrated Pt from Pt microelectrodes, examples of elongated droplets that look like they are just about to break up into two separate droplets, due to surface tension forces, can be observed. Besides this, it can be observed that the YSZ surface below the migrated Pd is significantly altered compared to the YSZ surface without migrated Pd. The

altered surface seems to consist of holes. This is supported by the lower left image showing a closeup, of the 105 hours temperature treated at $1000^0C$ migrated Pd, which is already presented in the article page 95. The mechanism of hole formation is unknown, but it is tempting to believe that Pd particles have been on top of or partly inside the holes at some point. To the lower right of the figure is an EDS spectrum of the particles in the images, confirming that it really is Pd that has migrated.

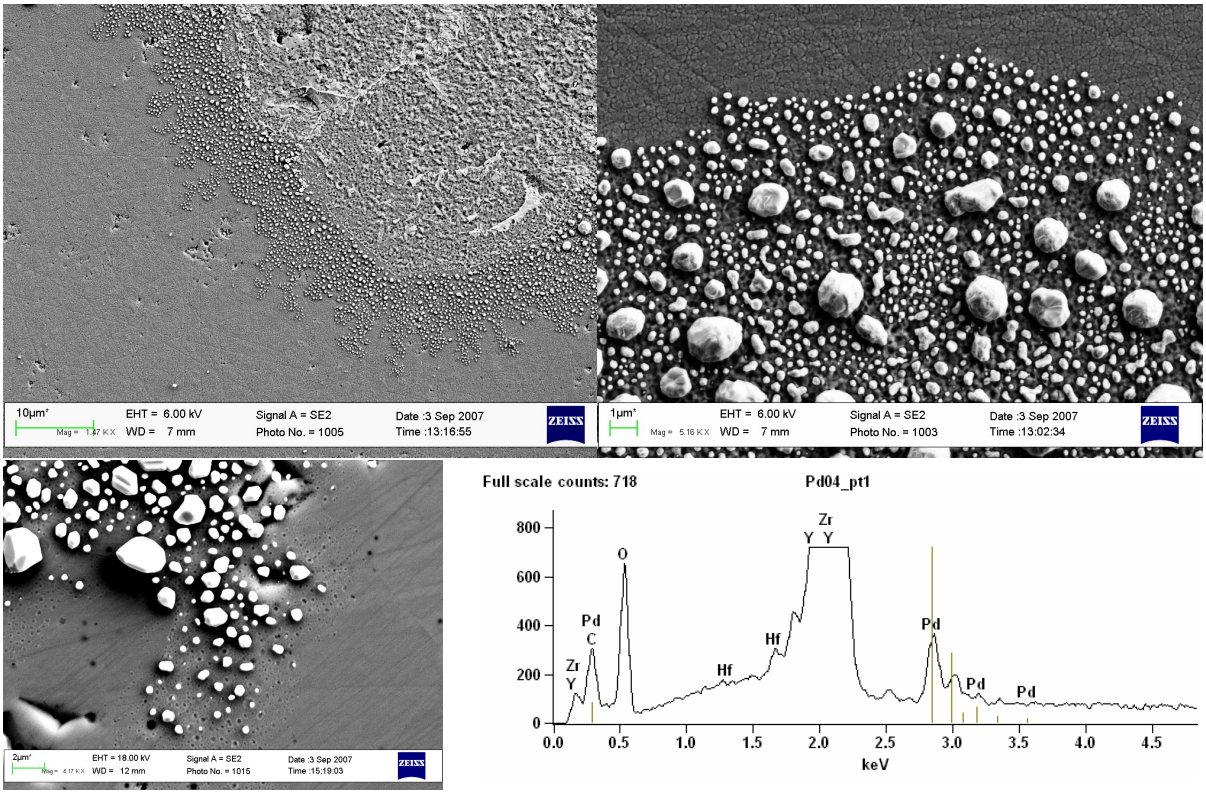


Figure 7.2: Selected images of migrated Pd upon polarization of Pd microelectrodes, along with an EDS spectrum of the migrated Pd particles.

### 7.2.2 Ag microelectrodes

Figure 7.3 page 99 shows a closeup image of the migrated Ag presented in the article page 94, along with an EDS spectrum of the migrated material confirming that it really is Ag. The closeup image reveals a morphology and

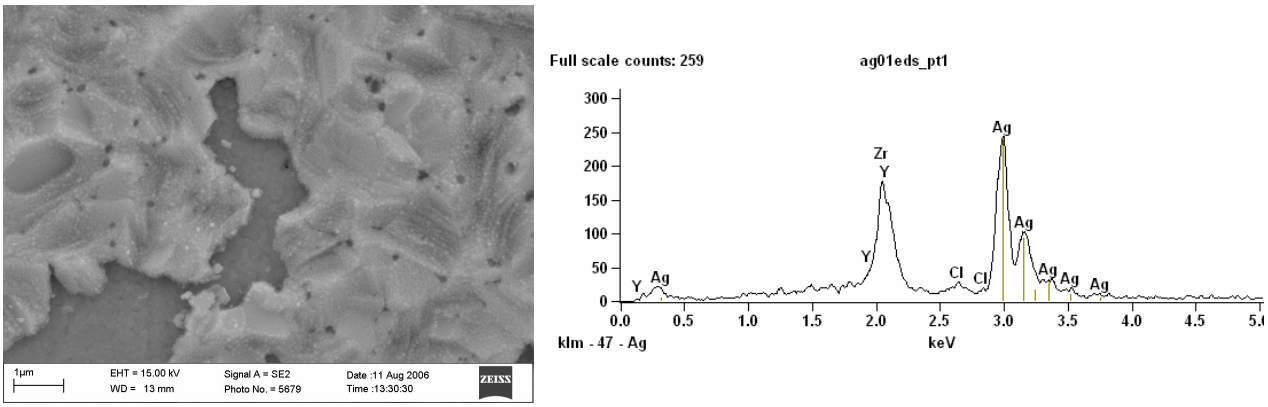


Figure 7.3: Closeup image of migrated Ag presented on page 94 and an EDS spectrum of the migrated electrode material.

a structure of the migrated Ag that seems comparable to that of migrated Pt presented on page 61 and 62.

# Chapter 8

# LSM and Au electrodes

## 8.1 Article

### SOFC cathode/YSZ - non-stationary TPB effects

J. Nielsen, T. Jacobsen

Submitted to:

**The 16th International Conference on Solid State Ionics (2007)**

**SOFC cathode/YSZ – non-stationary TPB effects**

Jimmi Nielsen and Torben Jacobsen

Department of Chemistry, Technical University of Denmark, DK-2800, Denmark

jim@kemi.dtu.dk

***Abstract***

The origin for the dynamic nature of $(La_{0.85}Sr_{0.15})_{0.95}MnO_{3\pm\delta}$ (LSM) cathodes with activation and deactivation processes was studied by comparison between measurements on and electrode/YSZ interfacial changes of Au, LSM point electrodes and thin ½-1µm thick LSM film electrodes on YSZ. The techniques used in the study were linear potential sweeps and long term (250-300hours) step polarization. The electrodes were after experiments removed by dissolution and the YSZ contact areas were studied by SEM and EDS. The results show current induced YSZ morphological changes, which lead to an increase in the Three-Phase-Boundary (TPB) length and consequently an activation of the electrode. In the case of LSM electrodes a current enhanced formation of $La_2Zr_2O_7$ was observed that can result in deactivating phenomena of LSM electrodes. The interplay between these processes can to a large extent explain the dynamic nature of LSM electrodes.

Keywords: SOFC, LSM, Gold, Non-stationary effects, Microstructure

## *1. Introduction*

It is well known for Solid Oxide Fuel Cell (SOFC) electrodes and SOFC model electrodes on Yttria Stabilized Zirconia (YSZ) that their properties are dynamic with activation and deactivation processes [1-8]. Despite the important impact on performance and stability most

research has been focused on electrode kinetics. Knowledge about the nature and origin of the observed activation and deactivation phenomena is therefore very sparse. Especially the role which polarization or current might have on the long term stability is unknown. Numerous studies have been conducted on solid state chemical reactions between strontium substituted lanthanum manganite cathodes and YSZ showing that insulating phases such as $La_2Zr_2O_7$ are formed and cause a degradation of the cathode [9-12]. However, this does not explain the reported activation of LSM cathodes. The exceptional strong activation of SOFC cathode, Pt model point and paste electrodes upon step polarization has recently been correlated with migration of Pt from Pt electrodes, resulting in an increase in the length of the electrochemical active Three-Phase-Boundary (TPB) and hence of the current [13]. Pt migration however, can not account for the activation processes of other SOFC electrodes such as Strontium substituted Lanthanum Manganite point and porous cathodes. This suggests the presence of another activation mechanism. The present study is an attempt to gain further knowledge about and to characterize the general non-stationary processes taking place at different polarizations by comparing electrochemical measurements on gold (Au) and dense sintered $(La_{0.85}Sr_{0.15})_{0.95}MnO_3$ (LSM) point electrodes and thin dense LSM films.

## *2. Preliminary considerations*

Gold electrodes are found to be stationary with respect to electrode perimeter upon polarization in contrast to Pt electrodes [13] and are therefore used as model electrodes. For the LSM experiments, LSM powder synthesized with excess manganese by the method used for commercial SOFC's were chosen in order to mimic the behavior of practical SOFC cathodes. For experiments on point electrodes is cannot be ruled out that the LSM/YSZ interface is damaged by scratching, rip offs etc. during disassembly for postmortem analyses.

Use of thin films as electrodes is a way to avoid damaging the LSM/YSZ interface after experiments by dissolution of the film in conc. hydrochloric acid, but the films are also expected to provide information about the role of contact pressure applied to point electrodes in electrochemical experiments.

### *3. Experimental*

The different electrode setups are sketched in figure 1. The electrodes were mounted in thin alumina tubes on top of polished 8% Yttria Stabilized Zirconia (YSZ). The YSZ electrolytes were sintered at 1500-1700$^0$C for 2 hours to achieve crystal sizes of several micrometer making it easier to detect and study any changes of the electrode/YSZ interface that might have occurred. The whole electrode assembly was placed inside a tubular furnace and heated to 1000$^0$C. The weights on the gold electrodes were in between 2.5-6g while the weights on LSM point electrodes were 6-12g. Gold electrodes were allowed to creep until a stationary state had been reached (1-2 days at 1000$^0$C) before electrochemical experiments were initiated. For the electrochemical experiments two electrode setups with reference/counter electrodes of Pt paste painted on the bottom of YSZ tablets were used. During measurements, air saturated with water at room temperature was passed through the furnace. $(La_{0.85}Sr_{0.15})_{0.95}MnO_3$ (LSM) powder was obtained from Topsoe Fuel Cell A/S. ½-1μm thick circular dense films of LSM on 1mm thick polished (1/4 μm diamond suspension) 8% YSZ were prepared by Pulsed Laser Deposition (PLD) using a 1mm thick cobber mask with holes of 2mm in diameter. After electrochemical experiments Au and LSM electrodes were removed by dissolution in aqua regia and hydrochloric acid respectively. The changes at and near the electrodes/YSZ interfaces were studied by SEM and EDS.

50Hz noise from the heating coils of the furnace was reduced as described in [4]. Data acquisition was done using a Gamry Femtostat FAS 2 potentiostat.

## *4. Results*

### 4.1 GOLD POINT ELECTRODES

Figure 2A shows representative linear potential sweeps of Au electrodes followed by a long term (200-300hours) step polarization. The sweeps show an almost exponentially increase in current in the anodic region and an unexpected sweep rate dependence of the current below -300mV in the cathodic region, where the current increases with decreasing sweep rate and at a slow sweep rate of 100μV/s a pronounced inductive hysteresis indicating an activation reaction is seen. Step polarization to a potential in the activating region results in a current progress shown in the inset figure in figure 2A. During 250 hours the current increases by a factor of approximately 40. Removal of the electrode by dissolution in aqua regia and inspection of the contact area reveals images like the one in figure 2B. Three distinct regions are observed. From the right is the Au/YSZ interface with a structure similar to the well known hill and valley structure reported for anode model Ni point electrodes [14-16], in the middle is the TPB region with the hill and valley structure but with a significant more rough surface morphology and to the left is the non-contact area with an unchanged YSZ surface. EDS shows only the presence of zirconium and yttrium and no crystallographic structural change is detectable by confocal raman spectroscopy with a interaction volume of approximately 1 $\mu m^3$.

**4.2 LSM POINT ELECTRODES**

Figure 3A shows representative linear potential sweeps initiated from 0V in the anodic direction on fresh LSM point electrodes. The sweep direction is found to have no significant influence. The inset figures show the initial sweeps with decreasing sweep rate in the potential window -150mV to 50 mV which was followed by a series of sweeps with a wider potential window from -250mV to 50mV. As sweeps are conducted a clear decrease in current from sweep to sweep is observed. The shape of the initial 100mV/s sweep is comparable to that expected from the classical Volmer-Butler equation as shown by the fit in the 100mV/s figure of figure 3A, but it is altered as irreversible processes take place during slower sweeps. At high sweep rate, 100mV/s, the current from the chemical capacitance, change in oxygen stoichiometry, $i=C_{chem}*dV/dt$ is predominant and results in capacitive hysteresis. As the sweep rate is decreased the response of activating and deactivating processes can be observed as inductive and capacitive hysteresis respectively. Further, increasing current fluctuations from the electrode reaction for overpotentials lower than approximately -75mV can be observed as the sweep rate is decreased. At a sweep rate of 10mV/s an inductive loop is seen in the overpotential range -75mV to 0mV, where the electrode still has a capacitive loop at lower overpotentials. As the sweep rate is decreased the inductive loop increases and below 100μV/s the cathodic region behaves purely inductive. The general trend from measurements on approximately 20 LSM point electrodes is the existence of an inductive and capacitive loop in the cathodic region meaning that two parallel processes are taking place. The interplay between the two different processes is dependent on the thermal and polarization history of the electrodes as well as the geometry of the contact area or areas between LSM/YSZ. In situations with both capacitive and inductive loops in the sweeps, the inductive loop is always observed at low cathodic polarizations typical from approx. -100mV to 0V while the

capacitive loop is observed from approx. -100mV to lower potentials. In some situations one of the processes is predominant as illustrated in the 10μV/s sweep of figure 3A with a pure inductive loop the cathodic region.

Removal of the electrodes by rip off and cleaning the YSZ surface in ultra sonic bath with conc. hydrochloric acid, water and ethanol after the electrochemical measurements results in a representative image of the LSM/YSZ contact area like the one shown in figure 3B. A porous hill and valley like structure is observed along the electrode perimeter while the interface between LSM and YSZ looks extensively damaged. Figure 3C shows that EDS on selected points and EDS mapping identifies the spongy like morphology of the interfacial area to contain lanthanum.

#### 4.3 LSM FILMS AS ELECTRODES

Two LSM films were deposited on top of each YSZ tablet. One of the LSM films is contacted with a gold electrode as shown in figure 1 and subjected to electrochemical experiments while the other LSM film serves as a reference with exactly the same preparation and thermal history. The films have a declining thickness as the perimeters of the circular films are approached from the middle. This variation in thickness is due to the shadowing effect of the holes in the mask during deposition. Further, the edges of the films are not abrupt but a gradual transition caused by imperfect contact between mask and the polished YSZ slice. Figure 4A shows linear potential sweep experiments of LSM films similar to those performed on point electrodes. The initial sweeps in the potential window -150mV to 50mV show, in contrast to the LSM point electrode sweeps presented, a slight increase in current with decreasing sweep rate although the following sweeps from -250mV to 50mV show the same decrease in current with decreasing sweep rate and hysteresis trends as the point

electrode sweeps. The shape of the initial 100mV/s sweep is more linear than in the case of the point electrode sweep and is probably due to lateral electronic resistance in the film. Beside this no fluctuating current with decreasing sweep rate is observed. After the sweeps the film was step polarized from 0V to -250mV. The current response can be seen in the inset figure of the 10μV/s sweep figure and shows initially deactivation, then activation and finally deactivation.

Figure 4B shows the film after experiments with the gold electrode removed. A clear transformation from an initially smooth dense film to a film with a surface structure consisting of 1 μm sized crystallites is observed. The reference film showed only a minor change from the initial film morphology. A heat treatment experiment of a film in nitrogen atmosphere at $1000^0$C for 250 hours showed a similar change as the film presented in figure 4B. It is therefore concluded that the change is thermodynamic favorable but limited by kinetics which becomes enhanced as the oxygen superstoichiometry of LSM is diminished by cathodic polarization or a lowering of the oxygen partial pressure.

Figure 4C is an image of the LSM/YSZ contact areas after the LSM films have been removed by dissolution in conc. hydrochloric acid followed by cleaning in ultrasonic bath of water and ethanol. The bright areas in the image contain lanthanum according to EDS. Comparison between the reference and polarized film shows that the amounts of lanthanum along the perimeter of the films as well as the interfacial area are significantly larger for the polarized film. Further the whole contact area of the polarized film is changed to a rough surface morphology with a homogeneous distribution of islands. In contrast to this, the surface of the reference film contact area is smooth with only minor humps along the grain boundaries. The humps along grain boundaries in the interfacial area and the lanthanum containing ring along the perimeter of the reference film is most probably passive formation

of $La_2Zr_2O_7$. It represents the areas where the LSM is easiest depleted for manganese due to passive diffusion which lead to the formation of $La_2Zr_2O_7$.

### *5. Discussion*

The apparent induced activation of Au electrodes for overpotentials lower than approximately -300mV shown in figure 2A can, with the morphological changes in figure 2B in mind, can be interpreted as an extension of the TPB length by channel formation along the electrode perimeter. Since the structural changes are by far largest close to the electrode perimeter with passage of current, it is tempting to interpret the changes as current induced. Gold electrodes are poor catalysts towards the reduction of oxygen and relatively large overpotentials are needed to achieve appropriate current densities for the current induced activation to take place. This means that similar activation phenomena are expected at lower cathodic overpotentials for better catalysts such as LSM.

The similarities between linear potential sweeps of LSM point electrodes and films suggest that the high contact pressure of point electrodes is of minor importance for the interpretation of the electrochemical measurements. Whether the observed electrochemical sweep rate dependent current fluctuations for point electrodes are due to a higher sensitivity or the presence of a high contact pressure is difficult to judge, but they strongly indicate that a process with a given characteristic time constant is taking place. The observed hill and valley like structure induced along the perimeter of LSM point electrodes and hence activation due to increase in TPB length seems to be similar to the activating morphological changes observed for gold electrodes, and as expected from the gold electrode experiments, the changes occur at considerable lower cathodic overpotentials. This however, is not the only process that takes place since the overall trend is a clear deactivation from sweep to sweep. The high abundance

of spongy lanthanum containing material insoluble in hydrochloric acid at the LSM/YSZ interface and electrode perimeter suggests that $La_2Zr_2O_7$ phases have been formed causing the general deactivation. The activation due to morphological changes is initiated at potentials with inductive hysteresis in the sweeps presented sweeps but at higher cathodic polarization it is overshadowed by the formation of $La_2Zr_2O_7$, resulting in the capacitive loops observed in the entire potential range. Hence, both the activation and deactivation process are current induced but with different overpotential dependencies. Inspection of figure 3C indicates that the highest abundance of what is presumed to be $La_2Zr_2O_7$ is correlated with the current density of the electrode. The region with activation upon step polarization in one of the inset figures of figure 3A could be due to the film becoming leaky during the transformation from a dense smooth film to a film consisting of 1μm crystallites. The final long term degradation could conveniently be interpreted as a blocking of the TPB by formation of $La_2Zr_2O_7$ at the leaky areas with a higher current density. This would explain the existence of the island LSM/YSZ interface morphology after removal of the film. This current induced formation of $La_2Zr_2O_7$ is supported by electrochemical experiments on LSM films with Au paste painted on top of the film. The interfacial areas with Au on top are unchanged while current supporting areas are found to be greatly enriched with $La_2Zr_2O_7$.

The understanding the electrochemical properties of LSM has widely been based on the work of M. Kleitz and co-workers who attempted to provide an overview of LSM properties by steady-state I-V characteristic measurements at $960^0$C in air [17]. They observed difficulties in reaching a steady state from -150mV to -200mV that can be explained by the results of the present study, which indicate that the I-V characteristic measured by M. Kleitz is not that of LSM but that of a poorly defined mixture of solid state chemical reaction products and LSM and a continuous changing morphology of the interface. At cathodic overpotentials

higher than -200mV they observed an exponential like increase in current that was interpreted as the onset of mixed ionic and electronic conductivity. The present results on Au point electrodes along with results on LSM electrodes question this interpretation by strongly indicating that other processes take place which might be the main reason for the exponential like increase in current from cathodic polarization of approximately -200mV and higher.

### *6. Conclusions*

Strong indications of current induced YSZ morphology activating changes from measurements on Au electrodes together with LSM electrode measurements have been presented. In the case of LSM electrodes it was shown that current significantly enhances the formation of unwanted insulating $La_2Zr_2O_7$ even though LSM with excess manganese was used. The fact that the formation of $La_2Zr_2O_7$ is enhanced by the current density may be of key importance for the SOFC long term stability/efficiency.

**Acknowledgement:**

This work is part of the research project "Efficient conversion of renewable energy by solid oxide cells" financed by The Danish Ministry of Science Technology and Innovation. Discussions with colleagues at Risø National Lab and in particular Nini Pryds and Katarzyna Rodrigo for the PLD preparation of thin LSM films are greatly appreciated.

### *References:*

[1] Y. Jiang, S. Wang, Y. Zhang, J. Yan, W. Li, J. Electrochem. Soc. 145, (1998) 373.

[2] M. Odgaard and E. Skou, Solid State Ionics 86-88, (1996) 1217.

[3] R. J. Aaberg, R. Tunold, M. Mogensen, R. W. Berg, R. Ødegård, J. Electrochem. Soc. 145, (1998) 2244.

[4] L. Bay, T. Jacobsen, Solid State Ionics 93, (1997) 201.

[5] S. Sridhar, V. Stancovski, U. B. Pal, J. Electrochem. Soc. 144, (1997) 2479.

[6] F. H. Van Heuveln, H. J. M. Bouwmeester, J. Electrochem. Soc. 144, (1997) 134.

[7] V. A. C. Haanappel, A. Mai, J. Mertens, Solid State Ionics 177, (2006) 2033.

[8] Wei Wang, San Ping Jiang, Solid State Ionics 177, (2006) 1361.

[9] Hee. Y. Lee, Seung M. Oh, Solid State Ionics 90, (1996) 133.

[10] A. Mitterdorfer, L. J. Gauckler, Solid State Ionics 111, (1998) 185.

[11] H. Y. Tu, Y. Takeda, N. Imanishi, O. Yamamoto, Solid State Ionics 100, (1997) 283.

[12] T. Kawada, N. Sakai, H. Yokokawa, M. Dokiya, I. Anzai, Solid State Ionics 50, (1992) 189.

[13] J. Nielsen, T. Jacobsen, Solid State Ionics 178, (2007) 1001.

[14] K. V. Jensen, S. Primdahl, I. Chorkendorff, M. Mogensen, Solid State Ionics 144, (2001) 197.

[15] K. V. Jensen, R. Wallenberg, I. Chorkendorff, M. Mogensen, Solid State Ionics 160, (2003) 27.

[16] M. Mogensen, K. V. Jensen, M. J. Jørgensen, S. Primdahl, Solid State Ionics 150, (2002) 123.

[17] E. Siebert, A. Hammouche, M. Kleitz, Electrochim. Acta 40, (1995) 1741.

***Figure captions:***

Figure 1: Sketch of experimental setup of the different electrodes.

Figure 2: **A:** Representative linear potential sweeps of fresh Au point electrodes followed by step polarization. **B:** Representative image after experiments and removal of Au electrodes of the YSZ changes along the Au electrode perimeter.

Figure 3: **A:** Representative linear potential sweeps of fresh LSM point electrodes on YSZ. Initially sweeps with a sweep rate from 100mV/s to 10µV/s were conducted in the potential window from -150mV to 50mV followed by similar sweeps in the potential window from -250mV to 50mV. **B:** Representative image after experiments and removal of LSM electrode of the LSM/YSZ contact area. **C:** EDS on selected points and lanthanum EDS mapping.

Figure 4: **A:** Representative linear potential sweeps of fresh LSM films as electrodes on YSZ. Initially sweeps with a sweep rate from 100mV/s to 10µV/s were conducted in the potential window from -150mV to 50mV followed by similar sweeps in the potential window from -250mV to 50mV. **B:** Image of LSM film after experiments with the electronic connecting Au electrode ripped off. **C:** Representative image after experiments and removal of reference and polarized LSM films of the LSM/YSZ contact areas.

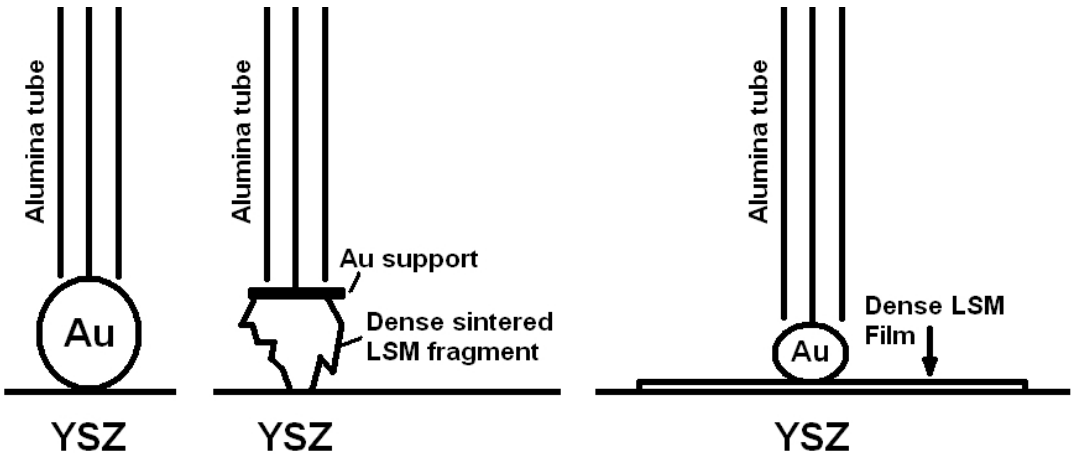


Figure 1: Sketch of experimental setup of the different electrodes.

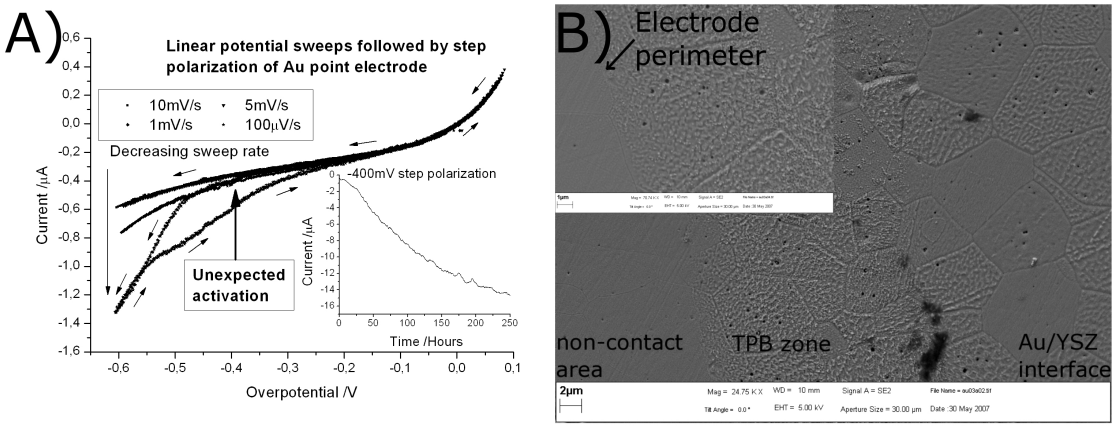


Figure 2: **A:** Representative linear potential sweeps of fresh Au point electrodes followed by step polarization. **B:** Representative image after experiments and removal of Au electrodes of the YSZ changes along the Au electrode perimeter.

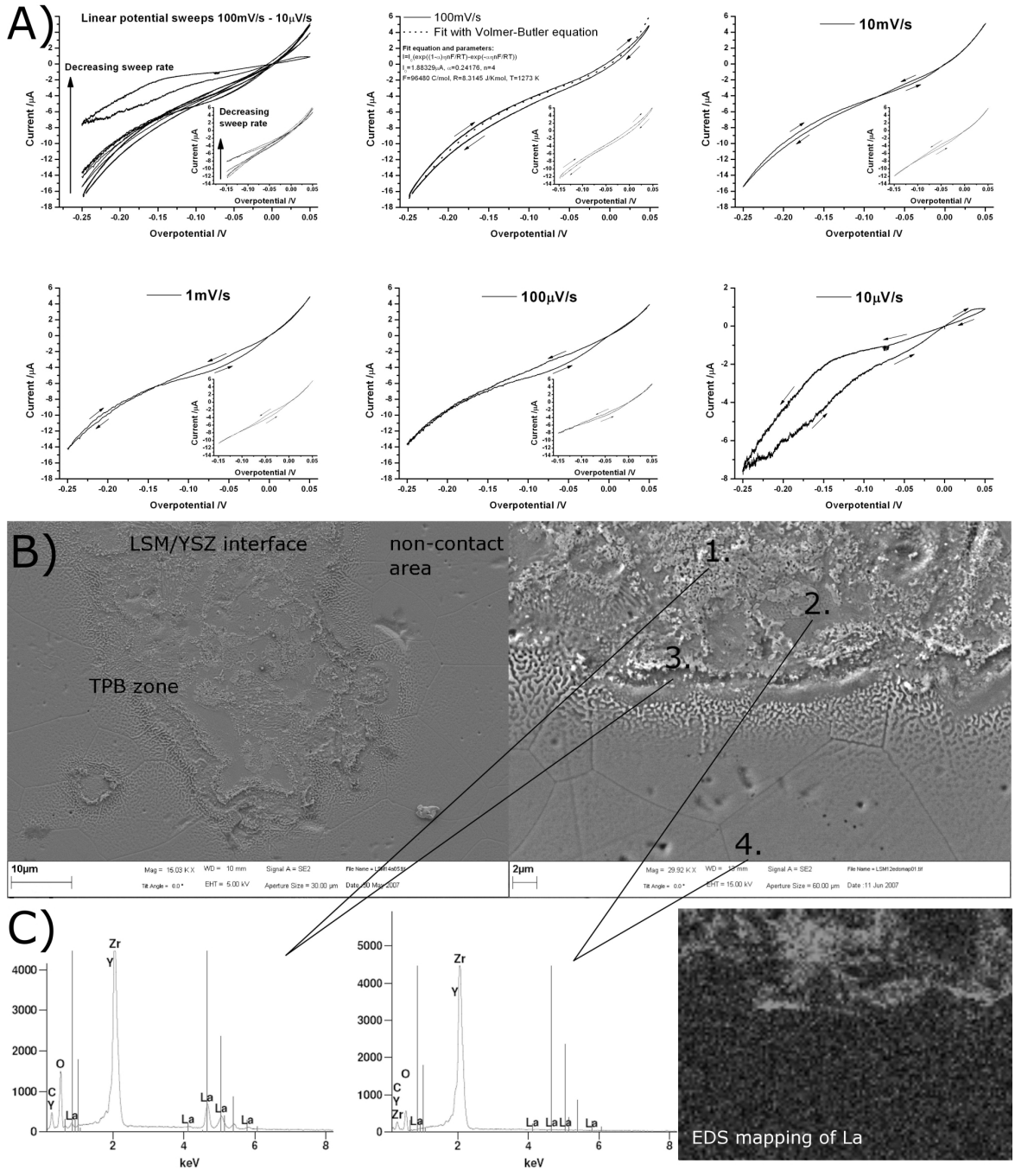


Figure 3: **A:** Representative linear potential sweeps of fresh LSM point electrodes on YSZ. Initially sweeps with a sweep rate from 100mV/s to 10 V/s were conducted in the potential window from -150mV to 50mV followed by similar sweeps in the potential window from -250mV to 50mV. **B:** Representative image after experiments and removal of LSM electrode of the LSM/YSZ contact area. **C:** EDS on selected points and lanthanum EDS mapping.

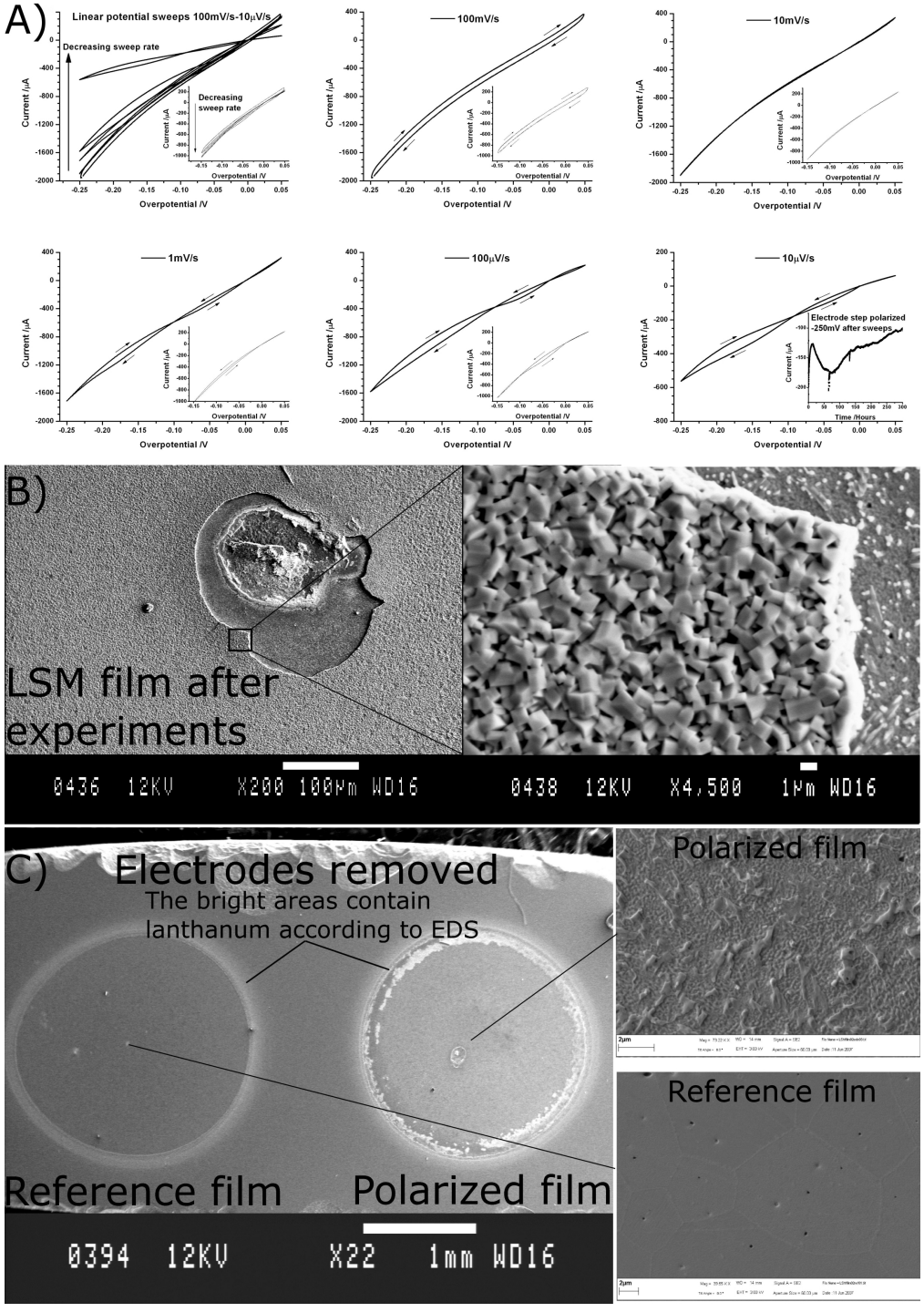


Figure 4: **A:** Representative linear potential sweeps of fresh LSM films as electrodes on YSZ. Initially sweeps with a sweep rate from 100mV/s to 10 V/s were conducted in the potential window from -150mV to 50mV followed by similar sweeps in the potential window from -250mV to 50mV. **B:** Image of LSM film after experiments with the electronic connecting Au electrode ripped off. **C:** Representative image after experiments and removal of reference and polarized LSM films of the LSM/YSZ contact areas.

## 8.2 Additional results with LSM and Au electrodes

### 8.2.1 Au point-electrodes

Figure 8.1 page 116 shows the activating current progression of an Au point electrode step polarized from 0V to -400mV along with an image of the contact area after experiment and removal of Au electrode. The behavior is in

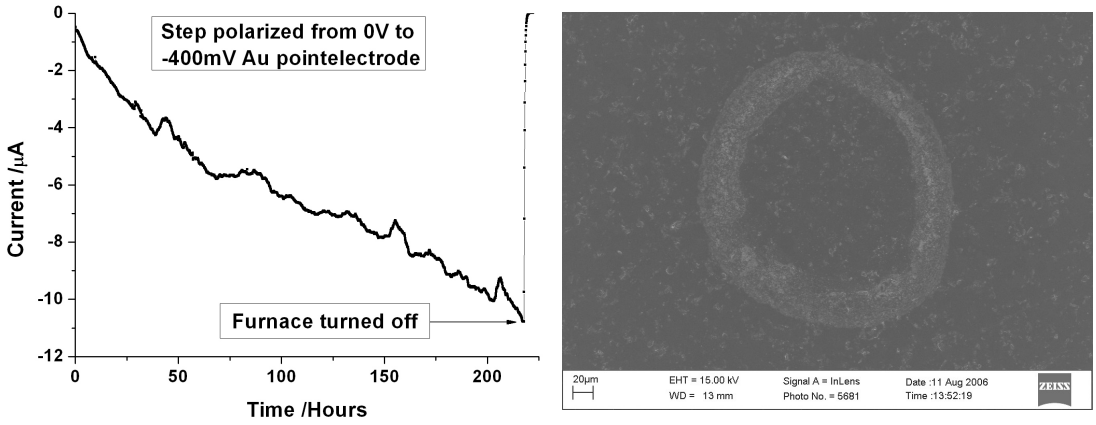


Figure 8.1: **Left:** Current progression of Au electrode step polarized from 0V to -400mV. **Right:** Overview image of the Au/YSZ contact area after removal of the electrode by dissolution in aqua regia and cleaning in an ultra sonic bath with water and ethanol.

accordance with the results presented in the article page 104. A clear belt of a more rough surface morphology is seen along the perimeter of the contact area. This illustrates how a porous structure is formed from the original perimeter and inwards. The formed porous structure, which oxygen can diffuse through, results in an increase of the reaction zone and hence increase in current. The continuous increase in current with time upon cathodic step polarization can, in this interpretation, be explained by the formation of the current induced interfacial porous YSZ structure. Since the changes are current induced the rate, of which the reaction zone increases, is expected to slow down as the oxygen diffusion length, within the formed porous structure, increases. Further, the loss of Au electrode support, by formation of a porous structure underneath the Au electrode, increases the YSZ and Au electrode contact pressure. This will, at some point, lead to a creeping of

the electrode, and thereby a collapse of the formed porosity. These feed-back mechanisms provide a limit to the extent of which the reaction zone can increase.
The observations, with the most pronounced changes along the current-

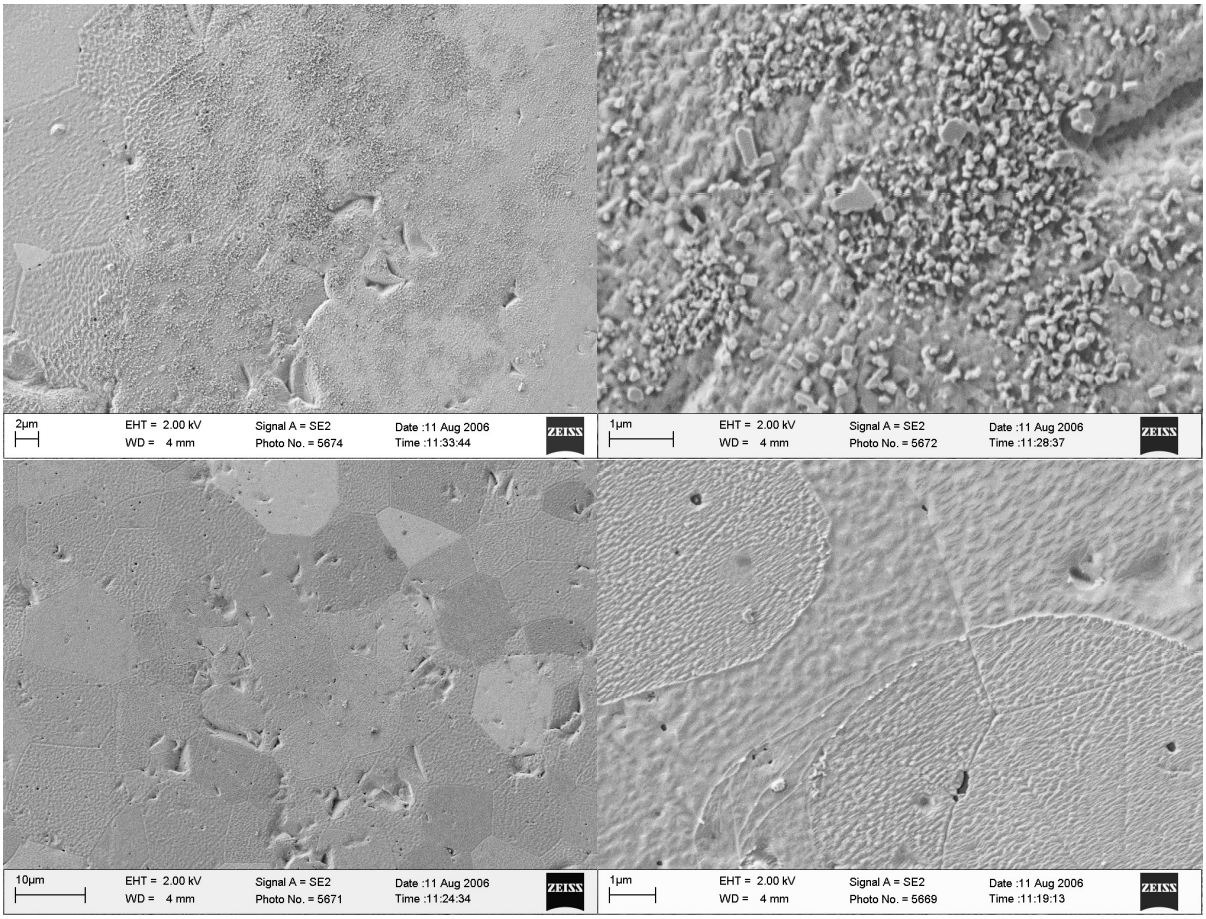


Figure 8.2: **Upper left:** Image of the perimeter of the Au electrode/YSZ surface contact area. **Upper right:** Close up image of the perimeter showing the induced rough surface morphology. **Lower left:** The interface between the Au electrode and the YSZ surface. **Lower right:** Close up image of the interface between the Au electrode and YSZ surface.

carrying perimeter, support the conclusion that it is current that is causing the changes. Closer inspections of the rough surface morphology along the perimeter and the interfacial morphology changes are illustrated in figure 8.2 page 117. The images of the interface shows that the "Hill and Valley structure" is formed on selected crystallite facets. The different energy of the

different crystallite facets is apparently sufficient to cause variations in the "Hill and valley structure" formation.
Point EDS at the perimeter and the interface is unsuccessful in detecting any presence of impurities.

### 8.2.2 LSM point electrodes

Using fragments of dense sintered LSM as electrodes generally provide uncontrollable sized contact areas with ill defined interfacial morphology. In some cases a very small contact area is achieved. The impedance spectrum of such a case is shown to the left in figure 8.3 page 119. The impedance response is

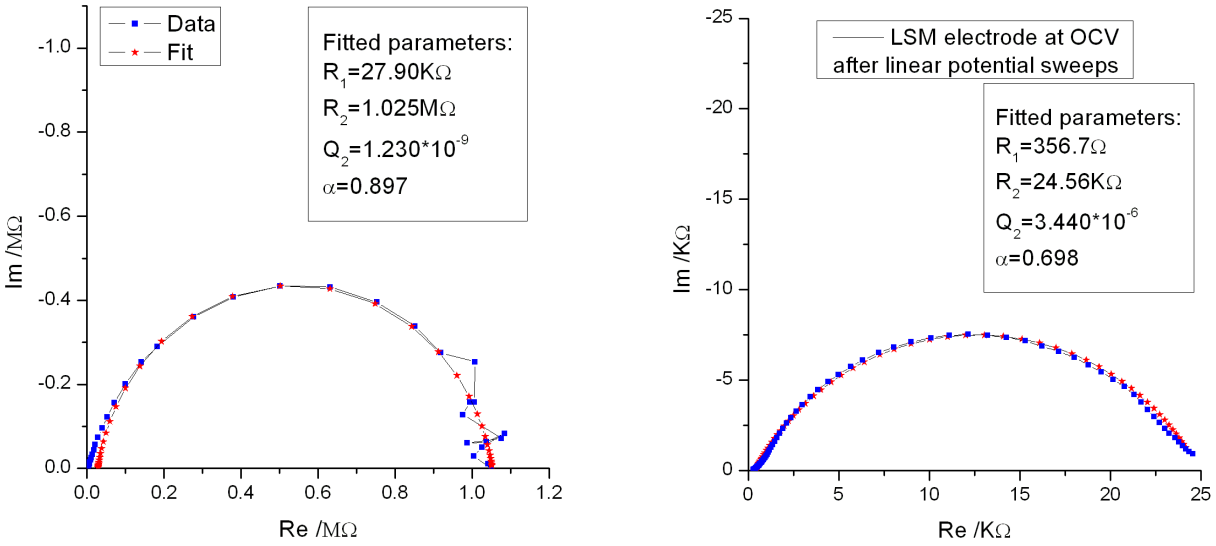


Figure 8.3: **Left:** The impedance spectrum of a LSM electrode, with a small contact area, at OCV immediately after heated to $1000^0C$. **Right:** The impedance spectrum of a LSM electrode after substantial series of conducted linear potential sweeps.

fairly well behaved and can almost be described with a slightly suppressed semicircle. The $\alpha$ value of 0.897 is the same as that, typically observed for impedance spectra of Pt microelectrodes, when using electrochemical etched Pt wires as electrodes. However, deviation from the suppressed semicircle is observed in the high frequency part of the impedance spectrum. The deviation has been reported many times in the literature [28, 67, 68] and it is interpreted as an interfacial reaction resistance at the LSM/YSZ interface. This interpretation relies merely on the fact that an interfacial charge transfer reaction resistance is expected to be observed at the high frequency part of the impedance spectrum. There is however, a good resemblance between the simulated impedance spectrum presented in section 5.5 page 41 and the left LSM impedance spectrum in figure 8.3 page 119. In this interpretation the deviation at high frequencies is due to LSM being only a moderately

good electronic conductor, compared to metals such as Pt and Au. The high frequency impedance response of LSM electrodes is further discussed in the LSM film section page 122.
The typical impedance response of a LSM electrode at OCV, after different performed linear potential sweeps, is presented to the right in figure 8.3 page 119. The impedance response can be described as a considerable suppressed semicircle with $\alpha = 0.698$. Nonetheless, deviation can be observed, and in many cases a single suppressed semicircle is insufficient in describing the impedance response at OCV of LSM electrodes with a polarization history. This is not surprising, when inspecting the LSM/YSZ interface after cathodic polarization experiments. This reveals images as those presented in figure 8.4 page 120. The interfaces are heavily altered with formation of a

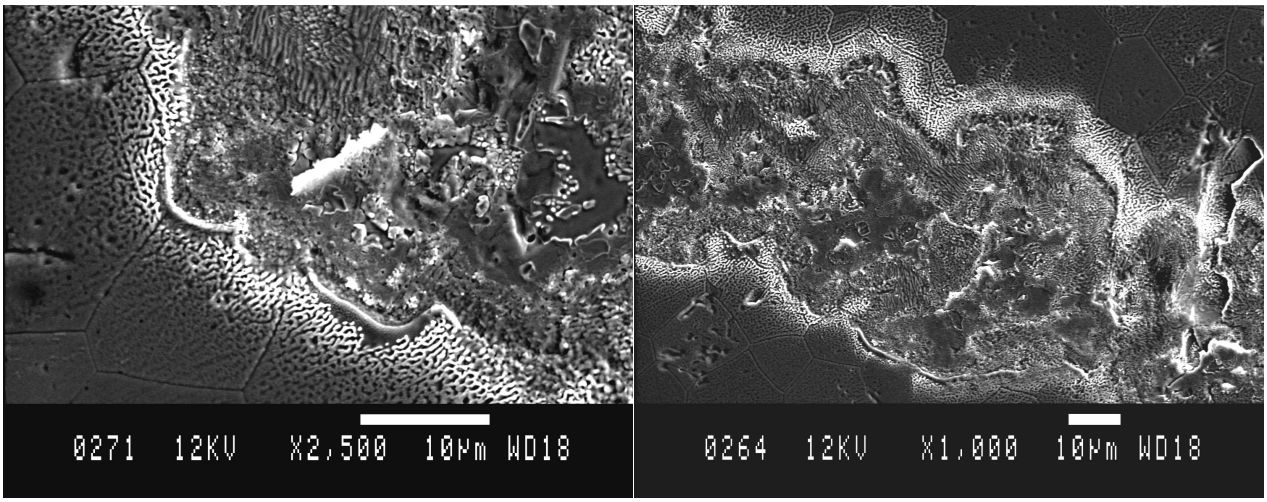


Figure 8.4: LSM/YSZ contact areas after various polarization experiments.

$La_2Zr_2O_7$ phase and induced porosity by the formation of the "Hill and valley structure". The interface is a poor defined mixture of different materials and a rough interfacial morphology, which depends on the polarization and thermal history. The dynamic nature of the LSM/YSZ interface is clearly illustrated by consecutive linear potential sweeps. Figure 8.5 page 121 shows selected linear potential sweeps in a comprehensive series of sweeps. From the sweeps to the left of the figure, the presence of a inductive and a capacitive loop is clearly observable. This is interpreted with the "Hill and Valley structure" formation process being dominating in the potential range from 0 to -100mV, while the formation of $La_2Zr_2O_7$ is dominating in the potential range from -100mV to -300mV. At a sweep rate of $100\mu V/s$, pronounced current fluctuations are observed in the potential range with capacitive hys-

teresis, indicating that competitive processes are taking place. By continuously conducting sweeps and changing the atmosphere it is possible to play around with the interplay between the two processes and thereby to force the interface into different states. This gives rise to different responses in linear potential sweeps as illustrated by the sweep to the right of figure 8.5 page 121.

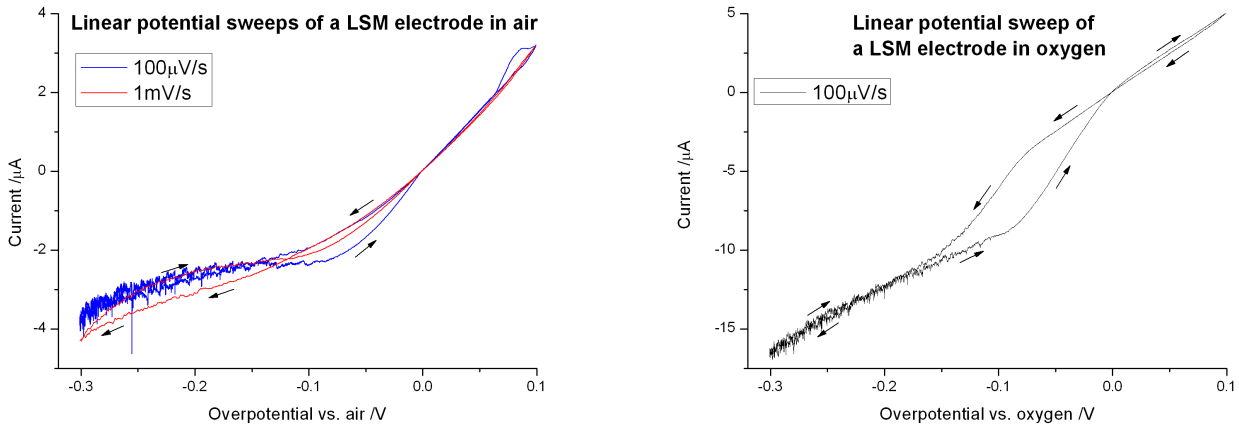


Figure 8.5: Linear potential sweeps of an old LSM electrode with a long linear potential sweep history in the potential window -300mV to 100mV. **Left:** Early sweeps in the electrode sweep history. **Right:** Late $100\mu V/s$ sweep in the electrode sweep history.

### 8.2.3 LSM films as electrodes

In order to gain further knowledge about the role of bulk oxygen transport versus the TPB, more and more researchers have focused their attention on electrochemical measurements on dense ceramic films. However, the electronic conducting properties of ceramics can lead to significant lateral ohmic resistance of the prepared films. The influence and significance of lateral ohmic resistance in electrochemical measurements has generally not been clarified. The lateral ohmic resistance $R_{film}$ is therefore calculated for the, in this thesis, relevant LSM and Pt films as function of thickness L, using the following derived formula in appendix A:

$$R_{film} = \frac{ln(1 + \frac{a}{R})}{2\pi\kappa L} \tag{8.1}$$

$\kappa$ is the conductivity, a is the radius of the film and R is the radius of the contacting electrode at the center of the film. The results are shown in figure 8.6 page 122. These calculations show, that significant lateral resistance

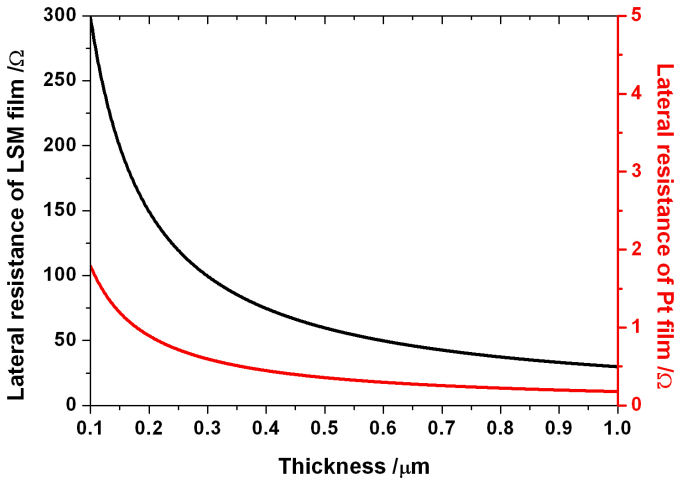


Figure 8.6: Lateral resistance of LSM and Pt films as function of thickness L. The used values for a and R are 1mm and $1\mu m$ respectively. The used conductivities $\kappa$ for LSM and Pt at $1000^0C$ are according to [62] 12850S/m and $2.13 * 10^6 S/m$ respectively.

are expected for the LSM films, while this is not the case for Pt films. A typical impedance spectrum of LSM films, immediately after reaching $1000^0C$ at OCV, is shown to the left in figure 8.7 page 123. The right image of the

figure shows an impedance spectrum of a LSM film with similar prehistory and conditions, but with painted Au paste on top. In both cases high and

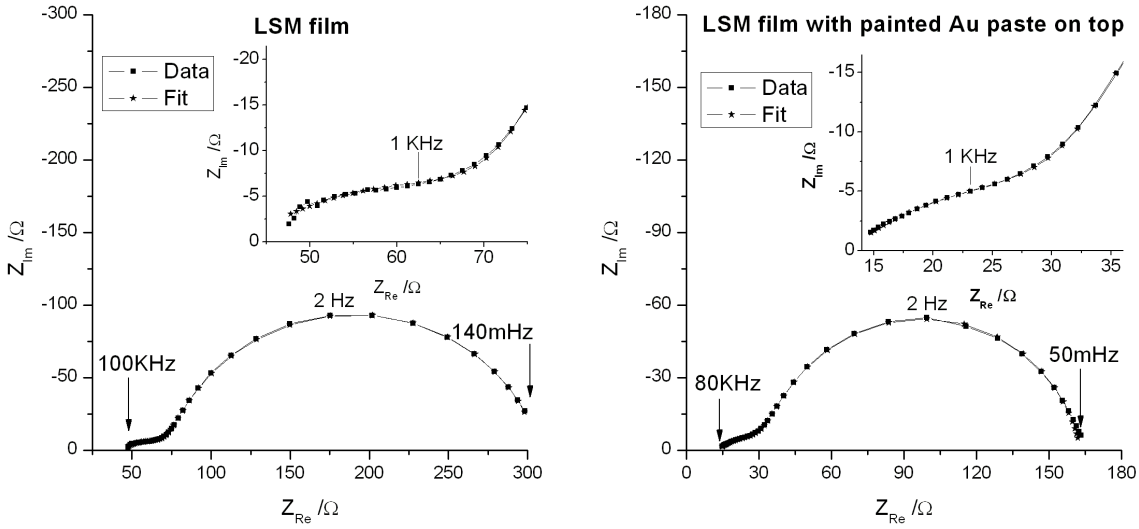


Figure 8.7: **Left:** The impedance spectrum of a LSM film at $1000^0C$ at OCV fitted with the equivalent circuit $R_1(R_2Q_2)(R_3Q_3)$. The fitted parameters are $R_1 = 42.30$, $R_2 = 36.49$, $Q_2 = 7.860 * 10^{-4}$, $\alpha_2 = 0.386$ $R_3 = 228.9$, $Q_3 = 6.016 * 10^{-4}$, $\alpha_2 = 0.863$. **Right:** The impedance spectrum of a LSM film with painted Au paste on top at $1000^0C$ at OCV fitted with the equivalent circuit $R_1(R_2Q_2)(R_3Q_3)$. The fitted parameters are $R_1 = 13.12$, $R_2 = 23.08$, $Q_2 = 1.054 * 10^{-3}$, $\alpha_2 = 0.467$ $R_3 = 127.1$, $Q_3 = 7.887 * 10^{-4}$, $\alpha_2 = 0.883$.

low frequency semicircles are observed. The responses can be well described with a serial connection of an electrolyte resistance $R_1$ and two times CPE's each in parallel with a resistor, $R_1(R_2Q_2)(R_3Q_3)$ in Boukamp notation. The high frequency semicircle is in many cases very difficult to resolve for LSM point electrodes, but is clearly resolved for the LSM films. By comparing the two impedance spectra, it is seen that painting Au paste on top of the film reduces both the resistance of the low and high frequency semicircle and thus the $freq. \rightarrow 0$ resistance. This clearly shows, as predicted, the presence of significant lateral resistance of the films. The electrolyte resistance of the films can be calculated using the Finite-Element-Method (FEM) software Comsol. The LSM film geometry was chosen, with a large electrolyte film compared to the 2mm in diameter electrode. The thickness of the electrolyte film was 1mm. The conductivity of YSZ at $1000^0C$ can be found in

the literature to be ranging from 100 to 200mS/cm [63, 64, 65, 66]. Setting the electrode to 1V, the ground to 0V, solving laplace's equation and doing a current boundary integration of the ground results in resistances between $7-15\Omega$. From this it can be concluded, that for the LSM film with Au paste on top, the lateral resistance is reduced to an extent so that the extrapolation $freq. \rightarrow \infty$ determined $R_1$ value corresponds to the situation where the potential throughout the electrode is constant. This is not the case for the LSM film without Au paste. In principle the double layer capacitance should yield the Newman situation, with the whole LSM/YSZ interface at constant potential, for the frequency $\rightarrow \infty$. Since the Newman situation is not reached in the impedance spectrum of the LSM film without Au paste on top, further impedance spectrum features might be present at even higher frequencies, which in practise are inaccessible. The high frequency semicircles are exceptionally suppressed. The cause to this remains unknown and only speculations can be made. A charge transfer resistance at the LSM/YSZ interface can in principle explain the existence of the high frequency semicircle, but so can the lateral ohmic resistance of the LSM film as shown in section 5.6 page 45.

### 8.2.4 Interfacial changes of polarized LSM films

Figure 8.8 page 125 shows images of the infacial changes of a LSM film, with painted Au paste on top, after experiment and removal of LSM by dissolution in aqua regia. The experiments were the exact same, with similar results, as those of the article presented in figure 3 page 114 and figure 4 page 115. From the images it is possible to observe areas with formation of $La_2Zr_2O_7$ and areas with formation of the "Hill and valley structure". The La, Zr, Y EDS mapping images of the figure show that the areas with "Hill and valley structure" do not contain lathanum and hence $La_2Zr_2O_7$. The images show that the formation of a "Hill and Valley structure" is not unique for anode Ni electrodes or cathode Au electrodes, but it also takes place at interfaces of real SOFC LSM cathodes and YSZ.

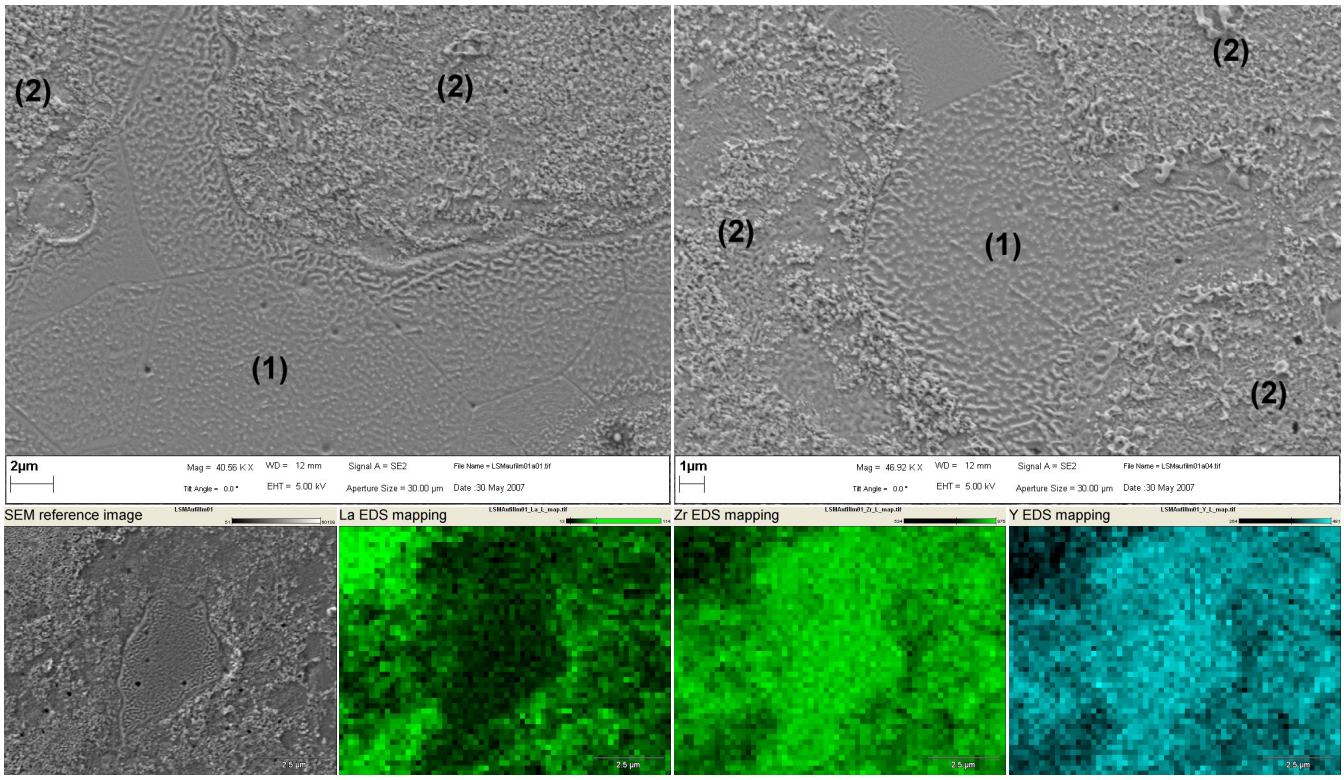


Figure 8.8: Images of cathodic polarized LSM film with painted Au paste on top. The images illustrate that two parallel processes are taking place: the formation of the (1) "Hill and valley structure" along with the formation of (2) the insulating $La_2Zr_2O_7$ phase. The lower row of the figure shows La, Zr and Y EDS mapping.

# Chapter 9

# Discussion and conclusion

## 9.1 Effects of potential distribution

The finite element calculations, presented in section 5.3 page 39, deal with the frequency dependent electrolyte resistance for pure electronically conducting point- and microelectrodes. The change in electrolyte resistance during impedance spectrum recording results in an error in the estimated reaction resistance $R_{reaction}$ determined as $R_{reaction} = Z(freq. \rightarrow 0) - Z(freq. \rightarrow \infty)$. The results show that the error for relevant point- and microelectrodes is of the same magnitude as the electrolyte resistance of the experiment. Depending on the catalytic properties, of the electrode the error in $R_{reaction}$ might be of significance, but for most point- and microelectrodes it is neglectable.

In section 5.4 page 41, it is shown that the two different potential distributions at high and low frequency interact with each other at the transition frequencies between the two potential distributions. The interaction resulted in a distortion of the impedance spectrum. The distortion was shown to be due to a continuous change in parameters, such as the electrolyte resistance and the capacitance, as function of frequency. It is difficult to assess whether these effects are significant in real measurement of point- and microelectrodes. The electronic conductivity of LSM is a factor 1000 lower than for Pt. This might cause a bending of the equipotential lines in LSM near the TPB, which can result in a distortion of LSM impedance spectra similar to the simulated spectrum in figure 5.5 page 41. A distortion can in many cases be observed for LSM as shown in figure 8.3 page 119, but it is very difficult to assess whether the distortion is due to interaction between different potential distributions or if it is due to an interfacial charge transfer resistance, as suggested in the literature.

The modelling of lateral ohmic resistance in films presented in section 5.6 page 45 provides two sources for current conduction. At high frequencies, it is the permittivity of the model electrode that conducts current, which results in a constant potential throughout the electrode. At low frequencies, it is the electrostatic conductivity of the model electrode that conducts current, and a potential gradient in the lateral direction of the film exist. The shift between the two different potential distributions of the two current sources results in an extensive interaction between the potential distributions at medium frequencies. At high frequencies, the removal of the lateral ohmic resistance can be observed. The modelling of the double layer capacity as a thin slice with isotropic permittivity is, however, questionable. The double layer capacity can in principle show lateral conduction to a certain degree. However, the extent to which this is possible is unclear. The response from lateral conduction of the double layer capacity might be at very high frequencies, which are not experimentally accessible. The existence of a high frequency very suppressed semicircle is clearly observed for LSM films with lateral resistance as shown in section 8.2.3 page 122. Whether this is due to the lateral ohmic resistance of the films or an interfacial charge transfer resistance as in the case of LSM point electrodes, is an open question.

## 9.2 Electrode material migration of noble metal SOFC model cathodes

The well known strong activating behavior of Pt upon medium to high cathodic polarizations was clearly identified in section 6 page 49 primarily to be caused by an extension of the electrode by Pt electrode material migration. The outgrowth of Pt, during cathodic polarization from the original electrode, was shown in some cases to happen in a dentritic manner. In such cases, characteristic saw-tooth like current fluctuations, were observed. The current fluctuations were identified with impedance spectroscopy to be synchronous with fluctuations in the electrolyte resistance and hence the electrode area. This lead to the conclusion that the current fluctuations were a consequence of cut off of dentritic shaped outgrown Pt by surface tension forces.
Section 7 page 76 showed that the electrode material migration is not unique for Pt. It is also observed for the noble metals Ag and Pd. However, Au do not show any electrode material migration. All the electrodes with elec-

trode material migration show inductive hysteresis in the cathodic region of linear potential sweeps and an activating current progression upon cathodic step polarization from OCV. Ag electrodes show activation on a comparable timescale as to Pt electrodes, but without any current fluctuations. Together with the post mortem analysis, it can be concluded that the dentritic outgrown Ag from the original electrode is not as easily cut off by surface tension forces as in the case of Pt. Pd, on the other hand, show a very fast activation on the timescale of seconds that show fast and very extensive current fluctuations. The Pd current fluctuations are different than the fluctuations for Pt electrodes in the sense that a continues decrease in current is observed followed by an abrupt increase. The exact opposite is observed for Pt electrodes. Post mortem analysis of Pd electrodes shows an overall dentritic outgrowth of Pd from the original Pd electrode. But the outgrown Pd consist of an ocean of small 10-100nm sized Pd particles which indicate that surface tension forces have an important role.

The transport of electrode material can generally happen by two transport mechanisms. It can either be a surface transport mechanism or it can be a gas phase transport mechanism where a volatile Pt, Ag or Pd specie is reduced at the cathodic polarized TPB. Calculated partial pressures of the relevant metal oxides are presented in figure 7.1 page 91. The partial pressures of Pt and Ag oxides are comparable, while the partial pressure of Pd and Au oxide is a factor 10000 lower. In an attempt to clarify whether it is possible to trap Pt from the gas phase at the TPB of a LSM film, the experiment on page 84 was constructed. In this experiment, a reservoir of Pt was deposited approximately $100\mu m$ from a cathodic polarized LSM TPB. The presence of Pt along the LSM TPB after the experiment was clearly identified by point EDS and EDS element mapping. In order to get a better feeling regarding the evaporation of noble metals, the temperature treatment experiments of migrated Pt, Ag and Pd presented on page 83 were performed. The experiments show that Pt and Ag evaporates on the same timescale as the cathodic polarized electrodes activate. Pd is also in this respect different than the Pt and Ag electrodes. The evaporation of Pd happens on a many orders of magnitude longer timescale ($> 10^5$) than the cathodic polarized Pd electrodes activate. The experiments mentioned above suggest that the migration of Pt and Ag is transported through the gas phase as metal oxides which are reduced at the cathodic polarized TPB. Pd migration is distinctively different than the migration Pt and Ag. The combination of a very low Pd evaporation and a fast Pd electrode activation means, that a gas phase transport mechanism of Pd can be ruled out. This leaves an unknown surface transport mechanism of Pd as the only explanation.

## 9.3 SOFC cathode reaction kinetics of Pt

The development of a hotstage setup made it possible to conduct measurements on an array of 300-400nm thick Pt microelectrodes with a varying size from $20\mu m$ to $250\mu m$ in diameter. The measurements were conducted before the Pt microelectrodes became leaky due to an inevitable breakup into smaller islands. As the electrode size decreased the presence of two semicircles became evident in the impedance spectra of the electrodes at OCV. This reveals the presence of two processes with different characteristic time constants. The determined reaction resistance $R_{reaction}$ was found to be inverse proportional to the electrode area for the largest microelectrodes, while $R_{reaction}$ was close to being inverse proportional to the perimeter for the smallest microelectrodes. This suggest, that bulk oxygen transport is able to take place for Pt. Similar behavior has been reported for Ag, which shows that Ag and Pt are more alike than previously assumed in the literature.

## 9.4 Non-stationary TPB effects of Au and LSM point-electrodes

In section 8 page 100, results were presented on heavily cathodic polarized Au point-electrodes, medium cathodic polarized LSM point-electrodes and LSM films.
The heavily polarized Au point-electrodes show activation which is revealed by post mortem analysis to be caused by morphological changes at and near the TPB. These morphological changes form a porous structure which extends the TPB length and hence results in an activation of the Au point-electrodes. It is further shown, that the YSZ surface at the Au/YSZ interface forms the well known "hill and valley structure" reported for the anode Ni model point-electrodes. The morphological changes are most pronounced along the current-carrying TPB, which indicates that current causes or accelerates the morphological changes.
Post mortem analysis of LSM point-electrodes and LSM film experiments show that two processes are taking place for LSM electrodes. In the case of Au point-electrodes, morphological changes are taking place at and near the LSM/YSZ interface. The formation of the "hill and valley structure" can be observed. This shows that it is not a unique occurring phenomena

for metal electrodes, but that it also applies to real SOFC cathode materials. But besides this, the formation of the insulating $La_2Zr_2O_7$ phase can also be observed. This is even the case though LSM with 5 percent excess manganese was used, which is believed to considerably reduce the formation of $La_2Zr_2O_7$. Both processes seem to follow the current-carrying perimeter of the electrodes. This indicate that the current has a roll in the observed changes. The morphological change causes an activation of the LSM electrodes, while the formation of $La_2Zr_2O_7$ causes a deactivation. The two processes have different dependencies with respect to the current density. This can be observed in linear potential sweeps as two hysteresis loops. One of the loops is inductive, while the other is capacitive.

# Appendix A

# Lateral resistance of films

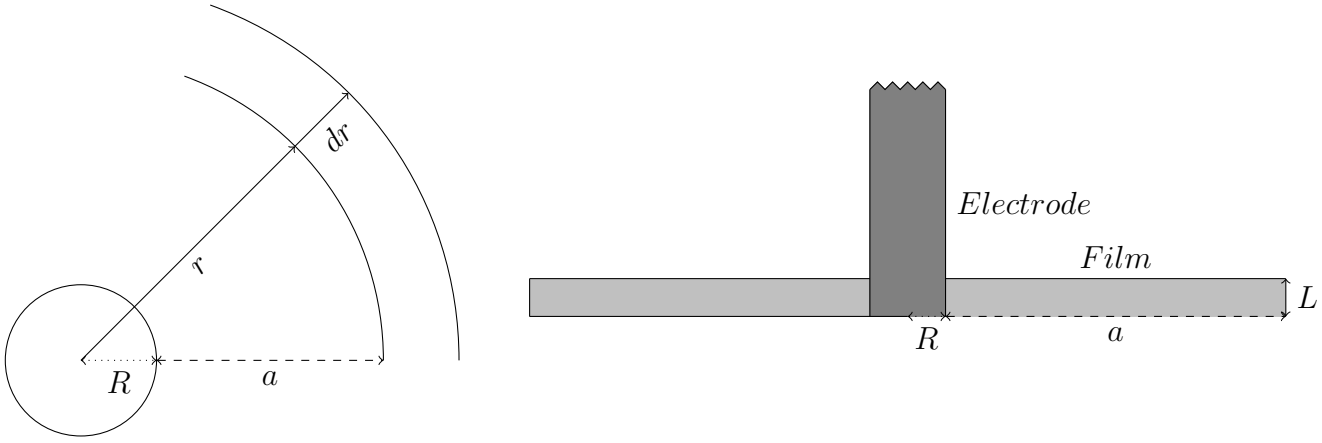


Figure A.1: Top view and cross section of the considered situation.

Top view and cross section of the situation, treated in the following, is sketched in figure A.1 page 131. The situation consist of a circular film with radius (R+a), thickness L, conductivity $\kappa$. The film is contacted with a infinitely good circular conductor with radius R at the center of the film. The lateral ohmic resistance of the film can be calculated in the following way:

Since cylinder geometry exists and conservation of charge must be obeyed we have the following relation for the current density i:

$$i(R)2\pi R = i(r)2\pi r \tag{A.1}$$

$\Downarrow$

$$i(r) = i(R)\frac{R}{r} \tag{A.2}$$

The relationship between the current density i and the driving force, which is gradient in potential, is:

$$i = -\kappa \nabla \varphi \tag{A.3}$$

$\Downarrow$

$$\frac{d\varphi}{dr} = -\frac{i(r)}{\kappa} = -i(R)\frac{R}{\kappa r} \tag{A.4}$$

$\Downarrow$

$$\varphi_{electrode} - \varphi_{R+a} = -\frac{i(R)R}{\kappa}\int_{R}^{R+a}\frac{1}{r}dr = \frac{i(R)R}{\kappa} ln(1+\frac{a}{R}) \tag{A.5}$$

The resistance can now be calculated as the potential drop divided by the total current I:

$$R_{film} = \frac{\Delta\varphi}{I} = \frac{\varphi_{electrode} - \varphi_{R+a}}{2\pi R i(R) L} = \frac{ln(1+\frac{a}{R})}{2\pi\kappa L} \tag{A.6}$$

# Appendix B

# Fitted hotstage data

The results of fitting the hotstage data with the two equivalent circuits $R_1(R_2Q_2)(R_3C_3)$ and $R_1(R_2Q_2(R_3C_3))$ are given on the following two pages in table B.1 and table B.2.

Table B.1: Fitted parameters with the equivalent circuit $R_1(R_2Q_2)(R_3C_3)$

| Diameter /$\mu m$ | $R_1$ /$\Omega$ | $R_2$ /$\Omega$ | $Q_2$ | $\alpha$ | $C_W$ | $R_2$ /$\Omega$ | $C_3$ /F |
|---|---|---|---|---|---|---|---|
| 20 | 1244 | 1.19E+06 | 4.49E-09 | 0.88 | 2.16E-09 | 3.49E+06 | 2.53E-08 |
| 20 | 1660 | 9.53E+05 | 4.93E-09 | 0.88 | 2.43E-09 | 9.75E+05 | 5.02E-08 |
| 20 | 986 | 1.28E+06 | 3.73E-09 | 0.88 | 1.76E-09 | 4.60E+06 | 2.13E-08 |
| Average | 1297 | 1.14E+06 | 4.39E-09 | 0.88 | 2.11E-09 | 3.02E+06 | 3.22E-08 |
| 30 | 1719 | 4.77E+05 | 7.80E-09 | 0.88 | 3.69E-09 | 1.89E+05 | 1.65E-07 |
| 30 | 1915 | 8.99E+05 | 6.46E-09 | 0.90 | 3.53E-09 | 1.62E+06 | 3.43E-08 |
| 30 | 1674 | 8.85E+05 | 6.85E-09 | 0.88 | 3.42E-09 | 1.13E+06 | 4.56E-08 |
| 30 | 1698 | 6.52E+05 | 6.43E-09 | 0.90 | 3.46E-09 | 4.34E+05 | 9.02E-08 |
| 30 | 1736 | 7.82E+05 | 6.10E-09 | 0.89 | 3.14E-09 | 7.89E+05 | 5.42E-08 |
| 30 | 1787 | 8.37E+05 | 6.27E-09 | 0.89 | 3.27E-09 | 9.05E+05 | 5.55E-08 |
| 30 | 1739 | 9.45E+05 | 6.57E-09 | 0.88 | 3.35E-09 | 1.31E+06 | 4.41E-08 |
| 30 | 1519 | 9.33E+05 | 6.37E-09 | 0.88 | 3.2E-09 | 1.40E+06 | 3.93E-08 |
| Average | 1723 | 8.01E+05 | 6.60E-09 | 0.89 | 3.40E-09 | 9.73E+05 | 6.61E-08 |
| 60 | 1400 | 4.80E+05 | 2.56E-08 | 0.84 | 1.12E-08 | 2.51E+05 | 1.48E-07 |
| 60 | 1647 | 4.98E+05 | 1.97E-08 | 0.88 | 1.07E-08 | 2.72E+05 | 1.47E-07 |
| 60 | 1261 | 5.24E+05 | 2.57E-08 | 0.85 | 1.22E-08 | 6.28E+05 | 7.72E-08 |
| 60 | 1576 | 5.47E+05 | 1.89E-08 | 0.89 | 1.08E-08 | 3.41E+05 | 1.22E-07 |
| 60 | 1578 | 5.76E+05 | 1.83E-08 | 0.89 | 1.07E-08 | 4.90E+05 | 8.88E-08 |
| Average | 1492 | 5.25E+05 | 2.16E-08 | 0.87 | 1.12E-08 | 3.97E+05 | 1.17E-07 |
| 100 | 1060 | 3.90E+05 | 1.33E-07 | 0.81 | 6.71E-08 | 4.99E+04 | 2.30E-07 |
| 100 | 1034 | 4.18E+05 | 9.62E-08 | 0.84 | 5.15E-08 | 8.54E+04 | 7.89E-08 |
| 100 | 498 | 2.90E+05 | 1.16E-07 | 0.79 | 4.65E-08 | 5.16E+02 | 2.57E-09 |
| 100 | 1106 | 4.42E+05 | 1.06E-07 | 0.83 | 5.73E-08 | 1.56E+04 | 5.17E-07 |
| Average | 925 | 3.85E+05 | 1.13E-07 | 0.82 | 5.60E-08 | 3.79E+04 | 2.07E-07 |
| 150 | 554 | 1.43E+05 | 3.10E-07 | 0.77 | 1.24E-07 | 2.17E+02 | 1.60E-08 |
| 150 | 836 | 2.04E+05 | 2.94E-07 | 0.81 | 1.54E-07 | 1.07E+04 | 6.40E-08 |
| Average | 695 | 1.73E+05 | 3.02E-07 | 0.79 | 1.40E-07 | 5.45E+03 | 4.00E-08 |
| 200 | 638 | 1.10E+05 | 4.83E-07 | 0.82 | 2.55E-07 | 3.98E+03 | 1.27E-07 |
| 200 | 620 | 1.06E+05 | 5.03E-07 | 0.81 | 2.54E-07 | 3.30E+03 | 1.37E-07 |
| Average | 629 | 1.08E+05 | 4.93E-07 | 0.82 | 2.54E-07 | 3.64E+03 | 1.32E-07 |
| 250 | 449 | 5.92E+04 | 1.08E-06 | 0.75 | 4.34E-07 | 8.14E+02 | 3.15E-07 |
| 250 | 460 | 5.70E+04 | 1.02E-06 | 0.76 | 4.24E-07 | 9.38E+02 | 2.76E-07 |
| Average | 455 | 5.81E+04 | 1.05E-06 | 0.76 | 4.29E-07 | 8.76E+02 | 2.95E-07 |

Table B.2: Fitted parameters with the equivalent circuit $R_1(R_2Q_2(R_3C_3))$

| Diameter /$\mu m$ | $R_1$ /$\Omega$ | $R_2$ /$\Omega$ | $Q_2$ | $\alpha$ | $C_W$ | $R_2$ /$\Omega$ | $C_3$ /F |
|---|---|---|---|---|---|---|---|
| 20 | 1061 | 4.72E+06 | 4.42E-09 | 0.87 | 2.50E-09 | 2.11E+06 | 1.09E-08 |
| 20 | 795 | 5.93E+06 | 3.68E-09 | 0.87 | 2.09E-09 | 2.11E+06 | 1.03E-08 |
| 20 | 1621 | 1.93E+06 | 4.79E-09 | 0.88 | 2.58E-09 | 2.35E+06 | 1.01E-08 |
| Average | 1159 | 4.19E+06 | 4.29E-09 | 0.88 | 2.42E-09 | 2.19E+06 | 1.04E-08 |
| 30 | 1703 | 6.67E+05 | 7.71E-09 | 0.88 | 3.79E-09 | 2.02E+06 | 1.06E-08 |
| 30 | 1862 | 2.53E+06 | 5.98E-09 | 0.90 | 3.67E-09 | 1.99E+06 | 1.01E-08 |
| 30 | 1617 | 2.03E+06 | 6.54E-09 | 0.88 | 3.62E-09 | 2.14E+06 | 1.04E-08 |
| 30 | 1670 | 1.09E+06 | 6.29E-09 | 0.90 | 3.56E-09 | 2.04E+06 | 1.13E-08 |
| 30 | 1683 | 1.58E+06 | 5.91E-09 | 0.89 | 3.29E-09 | 2.04E+06 | 1.03E-08 |
| 30 | 1730 | 1.75E+06 | 6.08E-09 | 0.89 | 3.44E-09 | 2.10E+06 | 1.14E-08 |
| 30 | 1654 | 2.26E+06 | 6.35E-09 | 0.88 | 3.57E-09 | 2.21E+06 | 1.08E-08 |
| 30 | 1451 | 2.34E+06 | 6.07E-09 | 0.88 | 3.41E-09 | 2.13E+06 | 1.03E-08 |
| Average | 1671 | 1.78E+06 | 6.37E-09 | 0.89 | 3.59E-09 | 2.08E+06 | 1.07E-08 |
| 60 | 1407 | 7.36E+05 | 2.37E-08 | 0.85 | 1.13E-08 | 2.27E+06 | 8.99E-09 |
| 60 | 1637 | 7.73E+05 | 1.84E-08 | 0.89 | 1.06E-08 | 2.25E+06 | 1.05E-08 |
| 60 | 1247 | 1.16E+06 | 2.21E-08 | 0.86 | 1.22E-08 | 1.79E+06 | 1.09E-08 |
| 60 | 1564 | 8.91E+05 | 1.74E-08 | 0.89 | 1.06E-08 | 2.38E+06 | 9.95E-09 |
| 60 | 1561 | 1.07E+06 | 1.64E-08 | 0.90 | 1.03E-08 | 2.23E+06 | 1.01E-08 |
| Average | 1483 | 9.27E+05 | 1.96E-08 | 0.88 | 1.11E-08 | 2.18E+06 | 1.01E-08 |
| 100 | 1058 | 4.99E+05 | 5.00E-08 | 0.88 | 3.05E-08 | 3.47E+06 | 8.46E-09 |
| 100 | 742 | 4.41E+05 | 1.00E-07 | 0.77 | 4.00E-08 | 3.77E+03 | 1.07E-08 |
| 100 | 990 | 2.88E+05 | 1.01E-07 | 0.80 | 4.25E-08 | 1.48E+06 | 4.49E-09 |
| 100 | 1110 | 4.56E+05 | 9.25E-08 | 0.84 | 5.12E-08 | 9.48E+06 | 2.66E-09 |
| Average | 975 | 4.21E+05 | 8.59E-08 | 0.83 | 4.25E-08 | 3.61E+06 | 6.58E-09 |
| 150 | 705 | 1.41E+05 | 2.52E-07 | 0.79 | 1.05E-07 | 2.65E+05 | 1.71E-08 |
| 150 | 662 | 2.13E+05 | 2.11E-07 | 0.77 | 8.53E-08 | 1.45E+05 | 4.22E-08 |
| Average | 684 | 1.77E+05 | 2.32E-07 | 0.78 | 9.53E-08 | 2.05E+05 | 2.97E-08 |
| 200 | 564 | 1.14E+05 | 3.79E-07 | 0.78 | 1.59E-07 | 6.83E+04 | 6.24E-08 |
| 200 | 546 | 1.09E+05 | 4.13E-07 | 0.77 | 1.67E-07 | 6.84E+04 | 5.49E-08 |
| Average | 555 | 1.12E+05 | 3.96E-07 | 0.78 | 1.63E-07 | 6.84E+04 | 5.86E-08 |
| 250 | 425 | 5.99E+04 | 9.85E-07 | 0.73 | 3.49E-07 | 7.42E+04 | 5.30E-08 |
| 250 | 435 | 5.78E+04 | 9.07E-07 | 0.74 | 3.28E-07 | 6.06E+04 | 6.19E-08 |
| Average | 430 | 5.89E+04 | 9.46E-07 | 0.74 | 3.39E-07 | 6.74E+04 | 5.74E-08 |

# Appendix C

# Calculated hotstage temperature

Heat transfer from the YSZ slice, with microelectrodes, exposed to the surroundings is mainly caused by radiation. The radiation from a blackbody as heat flux per unit surface area $q_{radiation}$ is described by Stefan-Boltzmann's law:

$$q_{radiation} = \varepsilon \sigma T^4 \tag{C.1}$$

The heat from the YSZ side with counter electrode and temperature $T_{counter}$ to the YSZ side exposed to the surroundings with temperature $T_{surf}$ is mainly transported by thermal conduction of the YSZ and obeys the following equation:

$$q_{conduction} = K\frac{(T_{counter} - T_{sur})}{\Delta x} \tag{C.2}$$

At thermal equilibrium the following relation must be obeyed:

$$q_{conduction} = q_{radiation}(T_{surf}) - q_{radiation}(T = 298K) \tag{C.3}$$

Setting $T_{counter} = 1173K$, $\Delta x = 1 * 10^{-3}m$ and using the typical YSZ property values stated below [62]:

| Symbol | Explanation | Value |
|---|---|---|
| $\varepsilon$ | Emittance of YSZ | 0.8 (typical value for ceramics) |
| $\sigma$ | Stefan-Boltzmann constant | $5.5704 \cdot 10^{-8}\ \frac{W}{m^2K^4}$ |
| K | Thermal conductivity of YSZ | $2\frac{W}{Km}$ |

yield a $T_{surf} = 1124K$ and hence the temperature difference across the YSZ slice $\Delta T = 49^0C$, when using maple to solve equation C.3 numerical.

# Bibliography

[1] S. B. Adler; Chem. Rev., 104 (2004), 4791-4843.

[2] N. L. Robertson, J. N. Michaels; J. Electrochem. Soc., 138 (1991), 1494.

[3] L. Bay, Ph.D. thesis, Technical University of Denmark, (1998).

[4] T. Kenjo, K. Tsukamoto; Solid Oxide Fuel Cells, Aachen Germany, (1997) 431-440.

[5] M. Kleitz, T. Kloidt, L. Dessemond; High-Temperature Electrochemical Behavior of Fast Ion and Mixed Conductors, Roskilde Denmark, 1993, p 89.

[6] T. Kawada, J. Suzuki, M. Sase, A. Kaimai, K. Yashiro, Y. Nigara, J. Mizusaki, K. Kawamura, H. Yugami; J. Electrochem. Soc., 149 (2002), E252.

[7] Solid State Electrochemistry, 26th Risø International Symposium on Materials Science 2005 p. 39.

[8] E. J. L. Schouler, M. Kleitz; J. Electrochem. Soc., 134 (1987), 1045.

[9] T. Jacobsen, B. Zachau-Christensen, L. Bay, M. Jorgensen; J. Electrochim. Acta, 46 (2001), 1019.

[10] Y. Jiang, S. Wang, Y. Zhang, J. Yan, W. Li; J. Electrochem. Soc., 145 (1998), 373.

[11] M. Odgaard, E. Skou; Ionics, 3 (1997), 75-81.

[12] S. McIntosh, S. B. Adler, R. A. Gorte; Electrochem. Solid State Lett., 7 (2004), A111.

[13] R. Lewis, R. Gomer; Surf. Sci., 12 (1968), 157.

[14] G. Kneringer, F. P. Netzer; Surf. Sci., 49 (1975), 125.

[15] S. G. Neophytides, D. Tsiplakides, C. G. Vauenas; J. Catalysis, 178 (1998), 414-428.

[16] A. C. Luntz, M.D. Williams, D. S. Bethune, J. Chem. Phys., 89 (1988), 4381-4395.

[17] J. L. Gland, B. A. Sexton, G. B. Fisher; Surf. Sci., 95 (1980), 587-602.

[18] C. T. Rettner, C. B. Mullins; J. Chem. Phys., 94 (1991), 1626-1635.

[19] C.Schwandt, W.Weppner, J. Electrochem. Soc., 144(11) (1997), 3728.

[20] J. Mizusaki, K. Amano, S. Yamauchi, K. Fueki; Solid State Ionics, 22 (1987), 313-322.

[21] B. L. Kuzin, M. A. Komarow, Solid State Ionics, 39 (1990), 163.

[22] N. L. Robertson, J. N. Michaels; J. Electrochem. Soc., 137(1) (1990), 129-135.

[23] M. J. Verkerk, A. J. Burggraaf; J. Electrochem. Soc., 130(1) (1983), 78-85.

[24] F. Berthier, J. P. Diard, B. Le Gorrec, C. Montella; Corrosion, 51(2) (1995), 105-115.

[25] A. Mitterdorfer, L. J. Gauckler; Solid State Ionics, 117 (1999), 187.

[26] A. Mitterdorfer, L. J. Gauckler; Solid State Ionics, 117 (1999), 203.

[27] A. Mitterdorfer, L. J. Gauckler; Solid State Ionics, 120 (1999), 211.

[28] E. Sibert, A. Hammouche, M. Kleitz; Electrochemica Acta, 40(11) (1995), 1753.

[29] A. Hammouche, E. Siebert, A. Hammou, M. Kleitz; J. Electrochem. Soc., 138(5) (1991), 1212.

[30] A. Mitterdorfer, L. J. Gauckler; Solid State Ionics, 111 (1998), 185.

[31] J. Mizusaki, T. Saito, H. Tagawa; J. Electrochem. Soc., 143 (1996), 3065.

[32] T. Ioroi, T. Hara, Y. Uchimoto, Z. Ogumi, Z. Takehara; J. Electrochem. Soc., 144 (1997), 1362.

[33] T. Ioroi, T. Hara, Y. Uchimoto, Z. Ogumi, Z. Takehara; J. Electrochem. Soc., 145 (1998), 1999.

[34] A. Endo, M. Ihara, H. Komiyama, K. Yamada; Solid State Ionics, 86-88 (1998), 1191.

[35] J. H. Kuo, H. U. Anderson, D. M. Sparlin; Solid State Chem., 83 (1989), 52.

[36] V. Brichzin, J. Fleig, H. U. Habermeier, G. Cristiani, J. Maier; Solid State Ionics, 152-153 (2002), 499-507.

[37] V. Brichzin, J. Fleig, H. U. Habermeier, J. Maier; Electrochemical and Solid-State Letters, 3(9) (2000), 403-406.

[38] H. Yokokawa, N. Sakai, T. Kawada, M. Dokiya; J. Electrochem. Soc., 138 (1991), 2719.

[39] H. Yokokawa, N. Sakai, T. Kawada, M. Dokiya; Solid State Ionics, 52 (1992), 43.

[40] T. Horita, K. Yamaji, N. Sakai, H. Yokokawa, T. Kawada, T. Kato; J. Electrochem. Soc., 145 (1998), 3196.

[41] T. Horita, K. Yamaji, N. Sakai, H. Yokokawa, T. Kawada, T. Kato; Solid State Ionics, 127 (1999), 55.

[42] J. Fleig, J. Power Sources, 102 (2002), 228.

[43] K. V. Jensen,S. Primdahl, I. Chorkendorff, M. Mogensen, Solid State Ionics, 144 (2001), 197-209.

[44] K. V. Jensen, R. Wallenberg, I. Chorkendorff, M. Mogensen, Solid State Ionics 160 (2003), 27.

[45] M. Mogensen, K. V. Jensen, M. J. Jørgensen, S. Primdahl, Solid State Ionics 150 (2002), 123.

[46] A. J. Nam, A. Teren, T. A. Lusby, A. J. Melmed; J. Vac. Sci. Technol., B 13(4) (1995), 1556-1559.

[47] J. Hoegh, K. V. Hansen, M. Mogensen, Proceedings of the Risoe International Symposium on Materials Science, 26th, Roskilde, Denmark, Sept. 4-8 (2005).

[48] L. Bay, T. Jacobsen, Solid State Ionics 93 (1997), 201.

[49] R. F. Harrington, Time-Harmonic Electromagnetic Fields, John Wiley and Sons, INC.

[50] J. Newman, J. Electrochem. soc., may (1966), 501-502.

[51] B. A. Boukamp, Solid State Ionics 20 (1986), 31.

[52] J. Fleig, J. Maier, Electrochimica Acta Vol. 41 (1996), 1003-1009.

[53] Rajesh Radhakrishnan, V. Anil Virkar, S. C. Singhai, Journal of the Electrochemical Society 152(5) (2005), A927.

[54] K. V. Jensen,S. Primdahl, I. Chorkendorff, M. Mogensen, Solid State Ionics, 144 (2001), 197-209.

[55] K. V. Jensen, R. Wallenberg, I. Chorkendorff, M. Mogensen, Solid State Ionics 160 (2003), 27.

[56] M. Mogensen, K. V. Jensen, M. J. Jørgensen, S. Primdahl, Solid State Ionics 150 (2002), 123.

[57] E. Ahlgren, F. W. Poulsen, Solid State Ionics 70/71 (1994), 528-532.

[58] B. K. Lee, Y. H. Yu, B. S. So, S. M. Kim, J. Kim, H. W. Lee, J. H. Lee, J. H. Hwang, J. Electroceram. 17 (2006), 735-739.

[59] L. Bay, T. Jacobsen, Solid State Ionics 93 (1997), 201-206.

[60] R. Radhakrishnan, A. Virkar, S. C. Singhal, J. Electrochem. Soc. 152(5) (2005), A927-A936.

[61] R. Jiménez, T. Kloidt, M. Kleitz, J. Electrochem. Soc. 144(2) (1997), 582.

[62] Facts & Figures, an International Energy Agency SOFC Task Report, Berne, April 1992.

[63] I.R. Gibson, G.P. Dransfield, J.T.S. Irvine, J. European Ceremic Soc. 18 (1998), 661-667.

[64] S.P.S. Badwal, Solid State Ionics 53 (1992), 23-32.

[65] C.C. Appel, N. Bonanos, A. Horsewell, S. Linderoth, J. Mat. Sci. 36 (2000), 4493-4501.

[66] S. Linderoth, N. Bonanos, K. V. Jensen, J.B. Bilde-Sørensen, J. American Ceramic Soc. 84 (2001), 2652-2656.

[67] M. Odgaard, E. Skou, Solid State Ionics 86-88 (1996), 1217.

[68] T. Ioroi, T. Hara, Y. Uchimoto, Z. Ogumi, Z. Takehara, J. Electrochem. Soc. 144(4) (1997), 1362.

[69] T. Jacobsen, B. Zachau-Christiansen, L. Bay, S. Skaarup, Proceedings of the 17th Risø International Symposium on Materials Science: High Temperature Electrochemistry: Ceramics and Metals p. 29 (1996).